

# **GZK Neutrino Search with the IceCube Neutrino Observatory using New Cosmic Ray Background Rejection Methods**

THÈSE N° 5813 (2013)

PRÉSENTÉE LE 28 JUIN 2013  
À LA FACULTÉ DES SCIENCES DE BASE  
LABORATOIRE DE PHYSIQUE DES HAUTES ÉNERGIES 1  
PROGRAMME DOCTORAL EN PHYSIQUE

ÉCOLE POLYTECHNIQUE FÉDÉRALE DE LAUSANNE

POUR L'OBTENTION DU GRADE DE DOCTEUR ÈS SCIENCES

PAR

**Shirit COHEN**

acceptée sur proposition du jury:

Prof. O. Schneider, président du jury  
Prof. M. Ribordy, directeur de thèse  
Dr P. North, rapporteur  
Prof. E. Resconi, rapporteur  
Prof. D. Ryckbosch, rapporteur



ÉCOLE POLYTECHNIQUE  
FÉDÉRALE DE LAUSANNE

Suisse  
2013



# Acknowledgements

It has been a great privilege and pleasure to take part in the IceCube collaboration research work during these past years. The effort to solve challenging physics questions within an international working group together with collaboration meetings and work stay abroad had been the most rewarding during this thesis work.

I thank my advisor Mathieu Ribordy for giving me the opportunity to join IceCube, for his strong physics understanding and sharp ideas during the research work, and for his support in finalising the analysis. The work would not have been possible without the day-to-day guidance of Levent Demiroers, and almost as important, his good company in the office. I am also grateful to Ronald Bruijn for his help and patience in the past year and friendly discussions aside from work. Arriving at the finishing line of this doctoral studies within our tiny IceCube group in EPFL is an achievement you have all helped to realise and I am grateful for it.

This research work was developed within the EHE/Diffuse working group in IceCube with its collaborators in the US, Europe and Japan — and accordingly complicated phone meetings schedule. I wish to thank my colleagues for good discussions on the physics topics and help swimming in the IceCube software, particularly Aya Ishihara, Keiichi Mase, Henrike Wissing and Spencer Klein.

The IceCube group was a part of the High Energy Laboratory at EPFL and I thank our LHCb colleagues for the good working atmosphere and a positive environment to master my French. It has been a pleasant experience tutoring physics classes for Olivier Schneider and I thank him for his advice and encouragement. Together with my friend Kim (always a keen supporter) we enjoyed a remarkably warm welcome by our Swiss fellow students Mathias, Geraldine, Marco and Cedric, and we all livened up the social life on the 6th floor... I also thank Neus and Yasmine for coffee breaks and sympathy.

I am deeply thankful to my mother Shulamit for her endless support and belief in me. The hard work and commitment to the family by both my mother and my late father, Amnon, have been truly inspirational. I am grateful to my brothers and their families for their encouragement and many joyful moments shared together. I strongly appreciate the support of the Liebig family. Finally, I thank my two men, Wolfgang and Carmi, for living through this adventure with me, the difficult moments and the rewarding ones.

*Lausanne, June 2013*

S. C.



# Abstract

Ultra high energy neutrinos are important astrophysical messengers that carry information on processes taking place in extreme astrophysical environments. The detection of neutrinos originating from the Greisen-Zatsepin-Kuzmin (GZK) process would confirm the proton dominance in the composition of the Ultra High Energy Cosmic Rays (UHECRs) as well as help to identify the unknown sources of the charged particles.

Data taken between April 2008 and May 2009 by the IceCube neutrino observatory in its 40 strings configuration were used for an all-flavour GZK neutrino event search. The main challenge for this search was the separation of the faint GZK neutrino signal (order of 1 event per year) from the several orders of magnitude higher atmospheric muon background. Special focus was given to identifying the topological differences between signal and background events and, based on them, the development of new background rejection techniques.

High energy events have been pre-selected by requiring a minimum amount of detected light and number of active photomultipliers in an event. Photon hits in IceCube's surface array photomultipliers were used to identify and reject atmospheric muon background events. Photon hit pattern differences (in time and space) in the in-ice detector between background and signal events were used to construct new cut parameters for background rejection.

UHE neutrino events were selected by a final analysis cut determined by optimising the Model Discovery Potential parameter (MDP) based on the neutrino flux from a reference GZK model. The predicted rates for the analysis live time of 315.34 days were 0.32 signal neutrino events and a total background rate of 0.015. The achieved least detectable signal by the analysis is 5.3 events which gives  $MDP=16.4$ . This means a normalisation factor of 16.4 higher on the reference GZK neutrino flux would be necessary in order to be able to claim a  $5\sigma$  discovery.

The full data sample was processed after the analysis methodology had been frozen and approved by the IceCube collaboration. No data events survived the analysis' final cuts. A 90% confidence level upper limit was calculated based on the null observation giving  $E^2\phi \leq 4.75 \times 10^{-8} \text{ GeV cm}^{-2} \text{ s}^{-1} \text{ sr}^{-1}$  in the energy range  $[10^{5.5}, 10^9] \text{ GeV}$ , a result slightly below the Waxman-Bahcall limit.

**Keywords:** GZK neutrinos, IceCube, South Pole, UHECRs



# Résumé

Les neutrinos de ultra-haute énergie sont des messagers astrophysiques importants qui recèlent de l'information sur les processus qui se déroulent dans des environnements astrophysiques extrêmes. La détection de neutrinos produits par le processus de Greisen-Zatsepin-Kuzmin (GZK) confirmerait la prédominance des protons dans la composition des rayons cosmiques de ultra-haute énergie (UHECR) et permettrait l'identification de ces sources inconnues des particules chargées.

Les données prises entre avril 2008 et mai 2009 par l'observatoire de neutrinos IceCube dans sa configuration à 40 chapelets ont été utilisées pour une recherche de tels événements. Le principal défi pour cette recherche est la séparation du faible signal GZK (de l'ordre de un événement par an) du bruit de fond de muons atmosphériques, plus élevé par plusieurs ordres de grandeur.

Une attention particulière a été accordée à l'identification des différences topologiques entre le signal et le bruit de fond des événements, résultant dans le développement de nouvelles techniques de rejet des muons atmosphériques.

Les événements de haute énergie ont été pré-sélectionnés en exigeant que les événements aient un minimum de lumière détectée et de photomultiplicateurs actifs. Le comptage de photons par les photomultiplicateurs du détecteur de surface de l'observatoire a été utilisé pour identifier et rejeter les événements de muons atmosphériques. Les différences entre le signal et le bruit de fond des distributions temporelles et spatiales des photons enregistrés par les chapelets enfouis sous la glace sont utilisées pour construire de nouveaux paramètres afin de mieux rejeter de bruit de fond.

Les événements de signal UHECR ont été sélectionnés à l'aide de coupures optimisées pour une découverte potentielle sur la base d'un modèle de référence de flux de neutrinos GZK. Les taux de comptage prévus par l'analyse pour une durée effective de prise de données de 315.34 jours sont 0.32 événements de signal et 0.015 événements de bruit de fond total. Il en résulte que le signal le "moins détectable" est 5.3 événements (i.e. un facteur  $MDP=16.4$ ). Cela signifie que le flux de référence devrait être 16.4 fois supérieur pour mener à une découverte avec un taux de confiance à  $5\sigma$ .

L'ensemble complet des données a été traité après que la méthodologie d'analyse ait été gelée puis approuvée par la collaboration IceCube. Aucun événement n'a survécu aux coupures finales de l'analyse. La limite supérieure, pour un taux de confiance à 90% et calculée sur

## Abstract

---

la base de cette observation nulle, est  $E^2\phi \leq 4.75 \times 10^{-8} \text{ GeV cm}^{-2} \text{ s}^{-1} \text{ sr}^{-1}$  dans la gamme d'énergie  $[10^{5.5}, 10^9] \text{ GeV}$ , un résultat légèrement inférieur à la limite Waxman-Bahcall.

**Keywords :** GZK neutrinos, IceCube, le pôle Sud, UHECRs

# Contents

<b>Acknowledgements</b>	<b>iii</b>
<b>Abstract (English/Français)</b>	<b>v</b>
<b>List of figures</b>	<b>xi</b>
<b>List of tables</b>	<b>xiv</b>
<b>1 Introduction</b>	<b>1</b>
<b>2 Theory</b>	<b>5</b>
2.1 Cosmic Rays . . . . .	5
2.1.1 Acceleration mechanism . . . . .	8
2.1.2 Cosmic ray sources . . . . .	9
2.2 Astrophysical neutrinos . . . . .	9
2.2.1 Astrophysical neutrino production models . . . . .	10
2.2.2 Theoretical bounds on a diffuse neutrino flux . . . . .	11
2.2.3 Active Galactic Nuclei as neutrino sources . . . . .	12
2.2.4 Gamma Ray Bursts as neutrino sources . . . . .	13
2.2.5 Cosmogenic neutrinos . . . . .	14
2.3 Atmospheric muons and neutrinos . . . . .	17
2.3.1 Atmospheric air showers . . . . .	18
2.3.2 Conventional atmospheric neutrinos . . . . .	18
2.3.3 Prompt neutrino component . . . . .	20
2.4 Neutrino interactions . . . . .	21
2.4.1 Electromagnetic cascades . . . . .	23
2.4.2 Hadronic cascades . . . . .	24
<b>3 The IceCube neutrino observatory</b>	<b>25</b>
3.1 Neutrino detection principle . . . . .	25
3.1.1 Lepton energy loss . . . . .	25
3.1.2 Cherenkov radiation . . . . .	27
3.2 Observatory overview . . . . .	28
3.3 The digital optical module . . . . .	30
3.3.1 The photomultiplier tube . . . . .	31

## Contents

---

3.3.2	PMT signal processing . . . . .	33
3.4	The data acquisition system . . . . .	35
3.5	Event topologies in IceCube . . . . .	35
3.6	South Pole ice properties . . . . .	36
3.6.1	The ice model . . . . .	37
<b>4</b>	<b>Simulation and reconstruction in IceCube</b>	<b>41</b>
4.1	Event simulation . . . . .	41
4.1.1	Atmospheric muon event generation . . . . .	42
4.1.2	Neutrino event generation . . . . .	42
4.1.3	Propagation . . . . .	43
4.1.4	Detector simulation . . . . .	44
4.1.5	Simulated data samples . . . . .	44
4.2	Event reconstruction . . . . .	44
4.2.1	Waveform processing . . . . .	45
4.2.2	Likelihood description . . . . .	45
4.2.3	Track first guess . . . . .	48
4.2.4	Muon track reconstruction algorithms . . . . .	49
<b>5</b>	<b>GZK neutrino search data analysis</b>	<b>51</b>
5.1	Analysis overview . . . . .	51
5.1.1	The searched signal . . . . .	51
5.1.2	Background events . . . . .	52
5.1.3	Analysis structure . . . . .	53
5.1.4	Data sample and simulated events . . . . .	54
5.2	Analysis level 0 (EHE Filter) . . . . .	56
5.3	Analysis level 1 . . . . .	56
<b>6</b>	<b>Atmospheric muon bundles rejection methods</b>	<b>61</b>
6.1	Atmospheric shower veto using IceTop . . . . .	61
6.1.1	Data and simulated events . . . . .	63
6.1.2	Veto efficiency dependencies . . . . .	63
6.1.3	Data and MC simulation results . . . . .	67
6.2	Early photon hit times . . . . .	71
6.2.1	Early $t_{\text{res}}$ hit density PDFs . . . . .	71
6.2.2	Construction of early $t_{\text{res}}$ likelihood parameter . . . . .	74
6.2.3	Early photon hits $\Delta \ln(L_{\text{tres}})$ parameter distributions . . . . .	74
6.3	Perpendicular light distribution . . . . .	76
6.3.1	Perpendicular light density parametrisation . . . . .	76
6.3.2	Construction of $\mu$ -function likelihood parameter . . . . .	77
6.4	Combined $\Delta \ln(L)$ parameter separation power results. . . . .	78

<b>7 Analysis final event selection</b>	<b>81</b>
7.1 Analysis level 2 . . . . .	81
7.2 Analysis level 3 cut optimisation . . . . .	82
7.2.1 Model Discovery Potential parameter . . . . .	83
7.2.2 Cut optimisation technique . . . . .	84
7.3 Final event selection . . . . .	87
7.3.1 Neutrino effective area . . . . .	89
7.4 Systematic uncertainties . . . . .	92
<b>8 Results &amp; discussion</b>	<b>95</b>
8.1 Discussion . . . . .	98
<b>A Appendix A</b>	<b>99</b>
<b>B List of abbreviations</b>	<b>107</b>
<b>Bibliography</b>	<b>109</b>
<b>Curriculum Vitae</b>	<b>117</b>



# List of Figures

1.1	The role of neutrinos as astrophysical messengers . . . . .	2
1.2	Supernova 1987A neutrinos detected by KamiokaNDE II . . . . .	3
2.1	Cosmic Rays energy flux . . . . .	6
2.2	UHECR energy flux as measured by Auger and HiRes . . . . .	7
2.3	UHECR measured $\langle X_{\max} \rangle$ and $\text{RMS}(X_{\max})$ distributions by the Auger experiment . . . . .	8
2.4	UHE protons attenuation length . . . . .	15
2.5	Number of produced GZK neutrinos during proton propagation . . . . .	16
2.6	UHE neutrino flux predictions from different GZK theoretical models . . . . .	18
2.7	Extensive air shower scheme . . . . .	19
2.8	Atmospheric conventional and prompt $\nu_{\mu} + \bar{\nu}_{\mu}$ fluxes . . . . .	21
2.9	Feynman diagrams for neutrino deep inelastic CC and NC interactions . . . . .	22
2.10	Neutrino interaction cross sections . . . . .	23
3.1	Muon energy loss processes in ice . . . . .	26
3.2	Geometry of Cherenkov light emission . . . . .	28
3.3	Scheme of the IceCube neutrino observatory . . . . .	30
3.4	IceCube 40-strings detector geometry . . . . .	31
3.5	Scheme of IceCube's digital optical module . . . . .	32
3.6	PMT ATWD waveform examples . . . . .	33
3.7	Event topologies in IceCube . . . . .	36
3.8	Absorption and effective scattering coefficients in the South Pole ice . . . . .	40
4.1	CORSIKA simulation event rate . . . . .	43
4.2	Cherenkov light front . . . . .	46
4.3	Residual time distribution and Pandel characterisation . . . . .	48
5.1	Theoretic GZK neutrino flux models . . . . .	52
5.2	GZK neutrino fluxes at the IC40 detector . . . . .	53
5.3	Analysis level 0 NPE distribution . . . . .	58
5.4	Analysis level 0 NCh distribution . . . . .	59
5.5	Analysis level 1 $\cos(\theta)$ vs. $\log(\text{NPE})$ distribution . . . . .	60
6.1	Definition of the IceTop and in-ice detectors impact parameters . . . . .	64

## List of Figures

---

6.2	The IceTop veto efficiency for p and Fe CRs . . . . .	65
6.3	IceTop veto efficiency vs. MC true energy dependency . . . . .	65
6.4	IceTop veto efficiency dependency (MC) on true detector containment values . . . . .	66
6.5	IceTop veto efficiency dependency (MC) on reconstructed detector containment values . . . . .	67
6.6	IceTop veto efficiency characterisation (MC) . . . . .	68
6.7	The IceTop veto efficiency in the data burn sample . . . . .	70
6.8	Negative $t_{\text{res}}$ hit density w.r.t. the MPE fitted track . . . . .	71
6.9	Negative $t_{\text{res}}$ 2D PDF distributions . . . . .	73
6.10	$\Delta \ln(L_{\text{tres}})$ parameter distribution at analysis level 1 . . . . .	75
6.11	$\Delta \ln(L_{\text{tres}})$ parameter distributions for different $\log(\text{NPE})$ ranges . . . . .	75
6.12	$\mu$ -function fit to light density distribution around a single muon track . . . . .	77
6.13	$\mu$ -function fit parameters $\log(a)$ vs $\omega$ 2D distributions . . . . .	78
6.14	Perpendicular light $\Delta \ln(L_{\text{perp}})$ distribution at analysis level 1 . . . . .	79
6.15	Combined $\Delta \ln(L_{\text{com}})$ parameter distributions . . . . .	80
7.1	Analysis level 2 $\cos(\theta)$ vs. $\log(\text{NPE})$ distribution . . . . .	82
7.2	Analysis level 2 distributions of parameters used for final cut selection . . . . .	85
7.3	Event rate distributions of $\Delta \ln(L_{\text{com}})$ vs $\log(\text{NPE})$ for zenith bin 10 . . . . .	86
7.4	Complement cumulative distributions of $\Delta \ln(L_{\text{com}})$ vs $\log(\text{NPE})$ for zenith bin 10 . . . . .	87
7.5	MDP parameter 2D map for zenith bin 10 . . . . .	88
7.6	Neutrino effective area for different analysis levels . . . . .	90
7.7	Neutrino effective area for different neutrino flavours . . . . .	91
8.1	Neutrino flux upper limit obtained by this analysis . . . . .	97
A.1	GZK neutrino signal distribution of $\Delta \ln(L_{\text{com}})$ vs $\log(\text{NPE})$ . . . . .	100
A.2	Corsika atmospheric muon background events distribution of $\Delta \ln(L_{\text{com}})$ vs $\log(\text{NPE})$ . . . . .	101
A.3	Atmospheric neutrino background distribution of $\Delta \ln(L_{\text{com}})$ vs $\log(\text{NPE})$ . . . . .	102
A.4	GZK neutrino signal complement cumulative distributions of $\Delta \ln(L_{\text{com}})$ vs $\log(\text{NPE})$ . . . . .	103
A.5	Corsika atmospheric muon background complement cumulative distributions of $\Delta \ln(L_{\text{com}})$ vs $\log(\text{NPE})$ . . . . .	104
A.6	Atmospheric neutrino background complement cumulative distributions of $\Delta \ln(L_{\text{com}})$ vs $\log(\text{NPE})$ . . . . .	105
A.7	MDP parameter value distributions w.r.t $\Delta \ln(L_{\text{com}})$ and $\log(\text{NPE})$ . . . . .	106

# List of Tables

5.1	IC40 Monte-Carlo simulation files used in this analysis . . . . .	55
5.2	IC40 IceTop and in-ice detector coincident MC simulation files used for IceTop veto studies . . . . .	55
5.3	Analysis level 0 passing event rates . . . . .	57
5.4	Analysis level 0 theoretic GZK models event rates . . . . .	57
5.5	Analysis level 1 passing event rates . . . . .	59
7.1	Analysis level 2 passing event rates . . . . .	82
7.2	Analysis level 3 passing event rates summary . . . . .	89
7.3	Analysis final cut selection (level 3) and event passing rates per zenith bin. . . .	90
A.1	$\cos(\theta)$ bins used at Analysis level 3 . . . . .	99



# 1 Introduction

Man's curiosity about the nature of the universe has always existed. Ancient cultures all around the world were methodically observing the night sky in plain eye, listing celestial objects and their trajectories and trying to explain their findings. The Chinese astronomers of the 2nd century reported the appearance of a bright star in the night sky in 185CE. The object that sparkled like a star was visible for eight months before fading away. Nowadays this is considered as the first supernova event observation recorded by humankind.

In contrast to old age astronomy that used only visible light, modern day astrophysics observes astronomical objects using several astrophysical messengers: lower energy photons such as radio or micro waves, higher energy photons such as X-rays and gamma rays, charged particles (cosmic rays) and most recently neutrinos.

A large amount of information is contained in photon emission coming from an astronomical source. Studying the energy range, luminosity and spectrum shape gives information about processes taking place at the source vicinity, its chemical composition and physical properties. Photons are emitted in abundance, are stable, point back to their source and are relatively easy to detect. However, photons are attenuated by interstellar gas and dust clouds, and interactions with the cosmic background radiation. Particularly for high energy sources further information is needed in addition to the detection of gamma-ray flux in order to distinguish between different acceleration models.

Studying the composition and characteristics of the cosmic ray flux gives information on a more global scale: acceleration power and processes taking place in our galaxy or beyond it. This is because emitted charged particles are deflected by galactic magnetic fields and therefore do not point back to their source when detected.

Neutrinos are uncharged particles that interact solely via the weak force with a very small interaction cross section. They are produced in nuclear reactions and high energy collisions, are not deflected or attenuated and therefore point back to their origin. High energy neutrinos produced in an energetic, optically thick environment escape the region instantly while gamma-rays produced in the same region are delayed due to multiple collisions. High energy neutrinos therefore establish the link between gamma-rays and high energy cosmic rays. The

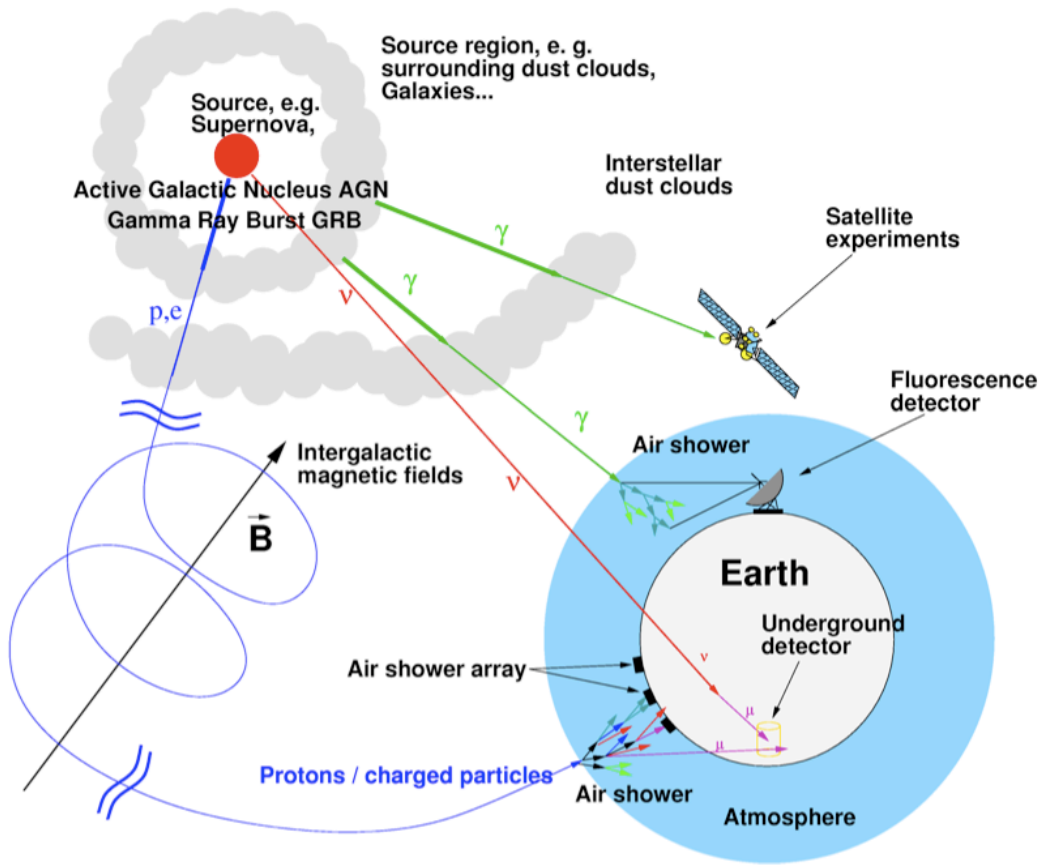


Figure 1.1: The role of neutrinos as messengers in high energy astrophysics. Energetic astrophysical environments may be the sources for emission of high energy cosmic ray particles, gamma rays and high energy neutrinos. The charged cosmic rays (p,e) are deflected by intergalactic magnetic fields and lose their directional information by the time they are detected. Gamma rays ( $\gamma$ ) are attenuated by interstellar dust clouds and interactions with the cosmic background radiation. The uncharged neutrinos ( $\nu$ ) traverse the cosmos freely and point back to their source when they are detected on earth.

relation between the different messenger particles from extraterrestrial sources and how they are detected is illustrated in Figure 1.1. Detection of all three astrophysical messengers is needed in order to determine the nature of processes taking place at the radiation sources.

The first achievements of neutrino astronomy were the measurement of the neutrino flux from the sun and providing evidence of neutrino oscillations, a finding which also indicates a non-zero neutrino mass. Another major discovery was the detection of neutrinos from the supernova event SN1987a taking place at the Large Magellanic Cloud, the only confirmed neutrino source to date apart from the sun. Neutrinos from SN1987a were recorded by three different neutrino detectors on earth, KamiokaNDE II in Japan [1] (see Figure 1.2), IMB in the US and BNO in Russia, three hours prior to the optical signal.

Recently built neutrino detectors and projects planned for the future are focusing on detection

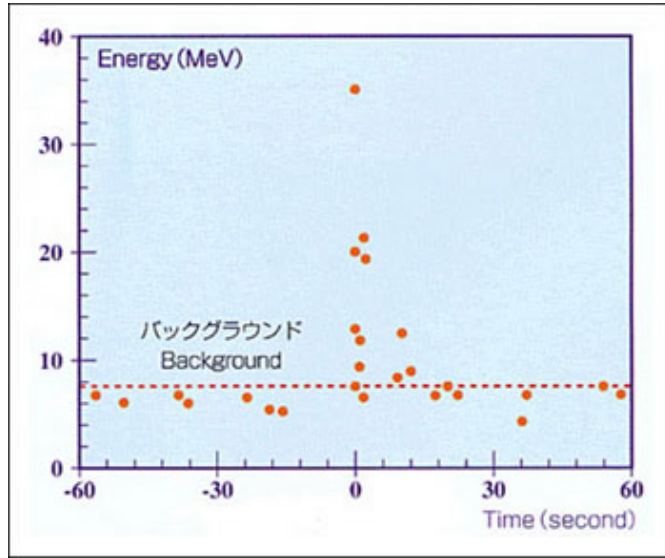


Figure 1.2: Neutrino events from supernova 1987A detected by the KamiokaNDE II detector in Japan. 11 events were counted within 12s.

of high energy neutrinos ( $> \text{GeV}$ ) as these are predicted to emanate from different cosmological sources. The construction of the IceCube neutrino observatory at the South Pole was completed in December 2010, reaching an instrumented volume of 1 cubic kilometre. IceCube is the largest neutrino detector to date and is able to measure neutrinos of energies  $> 10^9 \text{ GeV}$ .

This thesis work describes a search for a cosmogenic neutrino flux at extreme high energies as well as the development of signal-from-background separation techniques for these type of events using the half completed IceCube detector operational in 2008-2009. Detection of cosmogenic neutrinos is needed for determining the sources of the highest energy cosmic rays and their location as well as the cosmic ray spectrum at the source.



## 2 Theory

### 2.1 Cosmic Rays

First discovered in 1912 by Victor Hess, the nature of Cosmic Rays has been studied by multiple experiments since then.

Cosmic Rays (CR) are relativistic charged particles traveling through the universe. The composition of the CR flux is predominantly protons (79%), with Helium nuclei, heavier elements nuclei, and electrons constitute the other 21% [2]. Primary CRs are star nucleosynthesis products which are accelerated at astrophysical sources. These interact with interstellar gas producing secondaries such as antiprotons and positrons.

The measured energy flux of CR extends over 12 orders of magnitude, from  $10^9$  eV to  $10^{21}$  eV. Particles with energies lower than  $10^9$  eV are decelerated by the solar wind. The CR energy flux is described by an inverse power law with the differential flux given by  $dN/dE \propto E^{-\gamma}$  with few slope changes over the vast energy range. The most energetic particles observed ever in nature are CRs with energies of  $\sim 10^{20}$  eV. These Ultra High Energy CR (UHECR) are detected indirectly by large surface arrays for CR atmospheric shower detection and optical telescopes for the produced fluorescence and Cherenkov light. AGASA [3], HiRes [4] and the Pierre Auger Observatory [5] use these techniques for UHECRs detection. Direct detection of the CR flux at energies  $< 100$  TeV where the flux is relatively high is possible with small detectors carried by satellites or balloons to the top of the atmosphere (such as AMS [6], ATIC [7]). The flux in the middle range between 100 TeV and 1 EeV is detected indirectly by smaller air shower detector arrays such as KASCADE [8] and Tibet [9].

Figure 2.1 shows the CR flux for energies above  $10^{13}$  eV. The differential flux follows a power law with index  $\gamma = 2.7$  up to  $\sim 10^{15}$  eV, where a steepening of the spectrum occurs (a feature known as *the knee*) to an index  $\gamma = 3.2$ . At around  $10^{18} - 10^{19}$  eV the slope becomes softer again with  $\gamma \sim 2.8$  (*the ankle*), and finally the flux drops dramatically at about  $3 - 5 \times 10^{19}$  eV (see Figure 2.2). Particles with energies above the ankle are referred to as Ultra High Energy Cosmic Rays (UHECRs).

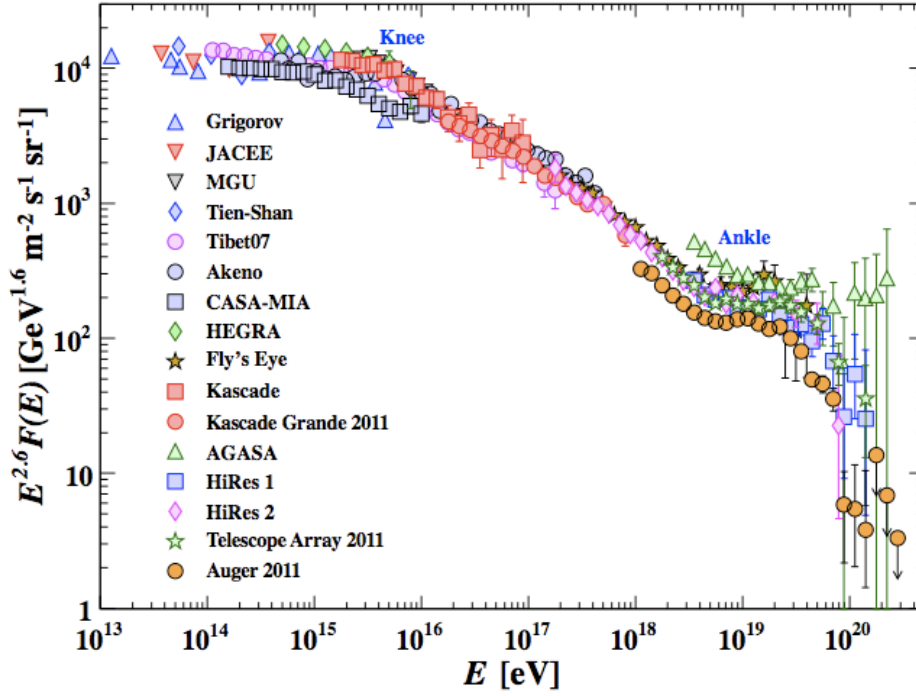


Figure 2.1: The cosmic rays energy flux as measured by different experiments. Taken from [10]

It is believed that the part of the flux up to *the knee* is of galactic origin. Beyond *the knee*, the flux transitions from a steep galactic component to a flat flux of extragalactic origin [11] and the CR mass composition changes. The Standard Model for Galactic Cosmic Rays (SMGCR) [12] predicts that Super Nova Remnants (SNRs) constitute the galactic CR sources via SNR shock acceleration. Within this model, the proton component of the galactic CR reaches its maximum energy at about  $4 \times 10^{15}$  eV and thus gives the most probable explanation for the existence of the knee. Assuming rigidity-dependent injection then the maximum energy of the galactic iron flux is expected to be 26 times higher at  $\sim 10^{17}$  eV [11].

Several theoretical models exist that describe the transition between galactic and extragalactic fluxes, its energy range and the changes in its mass composition. Three models are commonly used, the "ankle", the "dip", and the "mix composition" model. All three predict a heavy galactic component and a lighter extragalactic one but differ in other aspects. The ankle model predicts the transition to occur at *the ankle* which requires an additional high energy galactic flux component that exists beyond the  $10^{17}$  eV limit from the SMGCR. This energetic flux is expected to be heavy (iron). Several objects are suggested as possible sources, for instance SN explosions interacting with stellar wind or hypernovae. In the dip model, the transition from the galactic iron flux to the extragalactic proton flux takes place at a lower energy of  $4 - 7 \times 10^{17}$  eV and gives rise to the so-called *2nd knee*. Consequently, the dip in the total flux before *the ankle* is explained by UHE protons that loose energy due to pair-production

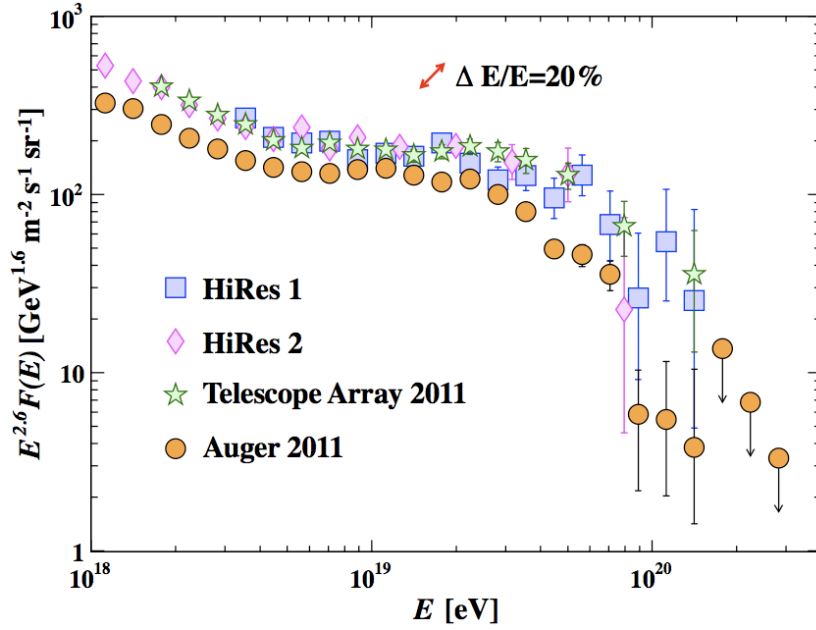


Figure 2.2: UHECR energy flux measurements from Auger, HiRes and Telescope Array. Taken from [10]

( $p\gamma \rightarrow p + e^+ + e^-$ ) from scattering on Cosmic Microwave Background (CMB) photons [11]. The mix composition model predicts a transition just before *the ankle* from galactic iron to an extragalactic mixed composition, a mix which is often dominated by protons.

Finally, assuming that the highest energy CRs are of extragalactic origin and of light nuclei composition, the flux's rapid steepening around  $3 - 5 \times 10^{19}$  eV may be explained by the predicted Greisen-Zatsepin-Kuzmin (GZK) effect [13]: pion production by scattering of the UHECR's on the CMB photons. In the scenario that the UHECRs composition is mixed or heavy, the propagating nuclei may interact with infra-red CMB photons and suffer energy losses by photo-disintegration and pair production [14]. The steepening of flux due to these losses occurs at lower energy than the flux steepening predicted by the GZK effect, and its shape differs. The  $e^+e^-$  pair production dip is present only if protons constitute at least 85% of the mixed. The higher the proton content in the composition mix, the more pronounced are the dip and *ankle* features [14]. High quality measurements of the UHECR flux features (dip and steepening) can be used then as an indirect measurement of its composition.

Several collaborations measured the composition of UHECRs in the energy range  $10^{18} - 10^{19.5}$  eV but so far results are inconclusive. Composition dependency is observed in distributions of  $\langle X_{\max} \rangle$  and  $\text{RMS}(X_{\max})$ , the shower-to-shower fluctuations of the depth of maximum. Results from HiRes [4] indicate a close to constant, light composition consisting of protons and possibly light nuclei. The Auger collaboration results [15] indicate a change of the composition from light to heavier elements above  $10^{19}$  eV (see Figure 2.3). It appears that the HiRes observations do not match the prediction of the ankle model for mass composition,

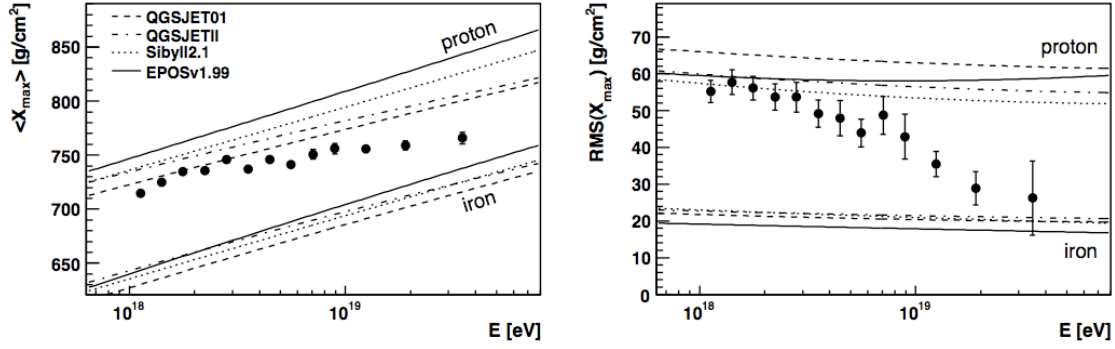


Figure 2.3: UHECR  $\langle X_{\max} \rangle$  (left) and  $\text{RMS}(X_{\max})$  (right) shower events measurements from the Auger experiment, taken from [16]. Data indicates light composition (probably dominated by protons) changing to a heavier mixture above  $10^{19}$  eV.

where the flux up to *the ankle* consists of galactic iron. These results are inconclusive and further work on this topic is needed to solve the composition question. The UHECR composition is crucial for predictions of a cosmogenic neutrino flux which is discussed in section 2.2.5.

### 2.1.1 Acceleration mechanism

The CR energy flux follows a power-law shape over many orders of magnitude, indicating that CRs do not result from thermal processes but from an acceleration mechanism where sources dissipate high energies to the acceleration process.

A likely candidate for this mechanism is Fermi's 1st order acceleration: charged particles are confined to a shock (discontinuity) region by magnetic inhomogeneities. When a particle bounces across the shock front back and forth it gains momentum proportional to the shock's  $\beta = v_s/C$  value, or otherwise energy  $\Delta E \propto E$ . The particle can undergo multiple reflections which increase its energy before it finally escapes the region. For a population of particles going through this process, the resulting spectrum is a power law given by  $dN/dE \propto E^{-\gamma}$ . For strong (supersonic) shocks the spectral index  $\gamma$  equals 2, for less energetic shocks the slope is steeper [17]. The measured CR energy flux has a steeper spectral index than the  $\gamma = 2$  injection spectrum due to energy losses during CR propagation.

Generally a particle continues to gain energy as long as it is confined to the shock region by the magnetic field, meaning the particle's gyroradius is smaller than the size of the acceleration region. The maximum attainable energy for a particle of charge  $Ze$  was calculated by Hillas [18] as

$$E_{\max} = \frac{\beta Z}{2} B_{\mu G} L_{\text{pc}} \quad (2.1)$$

where  $E_{\max}$  [10<sup>15</sup> eV],  $B$  [ $\mu$ G] is the magnetic field and  $L$  [pc] is the size of acceleration region.

### 2.1.2 Cosmic ray sources

For the CR spectrum below the knee, shock waves produced in supernova remnants (SNR) within our galaxy are suggested as the CR acceleration source. Various models estimate protons to be accelerated up to  $10^{15}$  eV within expanding SNRs. Observations of gamma ray emission of about  $10^{14}$  eV from SNRs point to electronic acceleration to slightly higher energies: Brehmsstrahlung and synchrotron radiation photons are subjected to inverse Compton scattering by the accelerated electrons resulting in a double hump flux shape. In addition, an energy balance calculation shows that the total energy deposited by the SNR population into CRs can account for the bulk of the measured galactic CR energy flux [19]. This calculation takes into account the SN event frequency, luminosity per SN event, and requires an assumption on the efficiency of SN energy transfer into CR kinetic energy. Other source candidates for galactic CRs are pulsar wind nebulae and binary systems which exhibit gamma ray emission.

With increasing energy of the CR spectrum and the transition from galactic to extragalactic origin, larger acceleration sites and stronger magnetic fields are needed at the sources in order to reach the obtained energies.

The energy density contained in the extra-galactic component of the CR flux is  $\rho_{\text{UHECR}} \approx 3 \times 10^{-19} \text{ erg/cm}^3$ . Assuming a cosmologically distributed population of sources accelerating CRs over a Hubble time of  $t_H \approx 10^{10} \text{ yr}$ , the required total power needed to reach the observed  $\rho_{\text{UHECR}}$  is

$$L_{\text{UHECR}} \approx 10^{45} \text{ erg Mpc}^{-3} \text{ yr}^{-1}. \quad (2.2)$$

Natural extragalactic source candidates are Active Galactic Nuclei (AGNs) and Gamma Ray Bursts (GRBs), objects that appear to be energetic enough to allow particle acceleration to energies around the ankle. With electromagnetic output of  $2 \times 10^{44} \text{ erg/s}$  from a typical AGN and  $2 \times 10^{52} \text{ erg}$  per GRB event these objects have the required power to produce the UHECRs flux, under the transparent source hypothesis - similar energy injected into CRs, gamma rays and neutrino emission. Relevant models for Ultra High Energy Cosmic Rays (UHECRs) production and the associated neutrino flux are given in sections 2.2.3 and 2.2.4 .

## 2.2 Astrophysical neutrinos

Accelerated cosmic rays escape their source and propagate through the surrounding radiation fields and gas clouds. Even if charged protons are trapped in sources due to magnetic fields, then the neutral neutrons created in  $py$  interactions may escape (transparent source) and later decay to protons, thus recovering the accelerated flux shape. Charged and neutral pions are created in the photo-nuclear and nuclear-nuclear interactions. Charged pion decay produces a neutrino flux while neutral pion decay results in gamma ray emission. A similar amount of energy is then found in the emitted photons, charged CRs and neutrino flux. The astrophysical neutrino flux is therefore dependent on CR interactions with its surroundings

and the detection of a neutrino flux from an astrophysical source is then a clear sign of hadronic acceleration taking place.

### 2.2.1 Astrophysical neutrino production models

The main pion production channels for photo-nuclear and nuclear-nuclear interactions are

$$\begin{aligned} p\gamma &\rightarrow p + \pi^0 \\ p\gamma &\rightarrow n + \pi^+ \end{aligned} \tag{2.3}$$

$$\begin{aligned} pp &\rightarrow p + p + \pi^0 \\ pp &\rightarrow p + n + \pi^+ \end{aligned} \tag{2.4}$$

The  $p\gamma$  interactions go through direct production as well as a large contribution with the  $\Delta^+$  intermediate state around its mass of  $m_\Delta = 1.2\text{GeV}$ . Protons are recuperated via neutron decay and neutron-photon interactions

$$n\gamma \rightarrow p + \pi^- \tag{2.5}$$

Neutrinos are then produced in charged pion decay via

$$\begin{aligned} \pi^+ &\rightarrow \nu_\mu + \mu^+ \\ \mu^+ &\rightarrow e^+ + \nu_e + \bar{\nu}_\mu \end{aligned} \tag{2.6}$$

$$\begin{aligned} \pi^- &\rightarrow \bar{\nu}_\mu + \mu^- \\ \mu^- &\rightarrow e^- + \bar{\nu}_e + \nu_\mu \end{aligned} \tag{2.7}$$

while neutral pion decay results in gamma ray emission

$$\pi^0 \rightarrow \gamma + \gamma \tag{2.8}$$

The resulting gamma ray and neutrino energy fluxes follow the initial CR flux, so a power law spectra is expected. In the  $p\gamma$  case the average energy transfer from the proton to the pion is  $0.2E_p$  [20]. Charged pion is produced in 1/3 of the cases and neutral pion otherwise, 2/3 probability. The pion passes in average  $0.25E_\pi$  to a daughter neutrino or  $0.5E_\pi$  to a produced

gamma ray. 4-momentum conservation and the kinematics of the decay are used to calculate the energy distributions of the daughter particles [21]. The fractions of initial proton energy transferred to a single neutrino or photon are  $\approx 1/20E_p$  and  $\approx 1/10E_p$  respectively. Eventually a similar amount of energy is deposited in gamma rays as in all-flavour produced neutrinos. A similar result is obtained for pp collisions [22].

Observations of solar as well as man-made neutrinos in the past 20 years give evidence for neutrino flavour oscillations [10]. Neutrinos have a mass, the mass and flavour eigenstates do not coincide resulting in neutrino flavour oscillations. Mass and eigenstates are related via a unitary matrix similarly as in the quarks sector, the Maki-Nakagawa-Sakata matrix [23] (MNS matrix). Detection of a high energy neutrino flux originating from an astrophysical distance means detection after very large number of oscillation cycles. The extension of the source itself (assuming a source is defined and the distance to it is known) means that not a fixed but a range of propagation distances has to be considered for detected neutrinos originating from it. More importantly, the neutrino energy measurement by itself has a substantial error. From these reasons a measured oscillation probability is in fact the averaged one over many oscillation cycles, and is dependent only on the neutrino mass matrix elements, which have been experimentally measured.

The neutrino flavour ratio at production from charged pion decay in pp or p $\gamma$  interactions is

$$\nu_e : \nu_\mu : \nu_\tau = 1 : 2 : 0. \quad (2.9)$$

Calculation of the flavour ratio over cosmological distance (assuming a measurement of the average oscillation probability) involves the MNS matrix elements. Our current knowledge of the matrix elements from neutrino oscillations measurements of solar, atmospheric and man-made neutrinos gives a very small  $\theta_{13}$  mixing angle (which means  $|U_{e3}|^2 \ll 1$ ) and measured  $\sin^2(2\theta_{\text{atom}})$  close to 1 (which gives  $|U_{\mu 3}| \simeq |U_{\tau 3}|$  when recognising the atmospheric oscillations angle with  $\theta_{23}$ ). Using this information, the flavour ratio after oscillations over a cosmological distances is then expected to be [24]

$$\nu_e : \nu_\mu : \nu_\tau = 1 : 1 : 1 \quad (2.10)$$

### 2.2.2 Theoretical bounds on a diffuse neutrino flux

The particle physics interactions leading to neutrino productions are well understood. However, the processes taking place in astrophysical sources, resulting in acceleration of CR to ultra high energies are not resolved. Different theoretical models exist describing the evolution of sources such as AGNs and GRBs and predicting a neutrino flux. In general, the predicted

neutrino flux is normalised with respect to observations of gamma ray or CR fluxes. With a similar argument, using the measured high energy cosmic ray flux and assuming that all high energy neutrino flux originates from CRs interactions one can obtain a model-independent upper bound for the sum of all extragalactic neutrino flux.

Waxman and Bahcall (WB) derived an upper bound on the diffuse extragalactic neutrino flux assuming optically thin sources and using UHECR normalisation [25]. They assume acceleration of protons taking place in cosmologically distributed sources. The protons interact with photons, producing pions, neutrons and protons. Charged pion decays produce neutrinos and neutron decays produce protons again. Assuming a proton injection spectrum of  $\Phi \propto E^{-2}$ , taking into account proton energy loss during propagation and the measured CR energy spectrum above  $10^{19}$  eV, the generation rate of CRs was calculated to be

$$E_{\text{CR}}^2 \frac{dN_{\text{CR}}}{dE_{\text{CR}}} \approx 10^{44} \text{ erg Mpc}^{-3} \text{ yr}^{-1}. \quad (2.11)$$

The produced protons interact with photons producing charged and neutral pions. As demonstrated before, charged and neutral pions are generated roughly with the same probability, and a single neutrino emitted from charged pion decay has an average energy  $E_\nu \approx 0.05 E_p$ . Noting that the two muon neutrinos produced per charged pion decay take about half of its energy and taking into account neutrino generation over Hubble time  $t_H \approx 10^{10}$  yr, the current  $\nu_\mu + \bar{\nu}_\mu$  energy density is given by

$$E_\nu^2 \frac{dN_\nu}{dE_\nu} \approx 0.25 \times t_H E_{\text{CR}}^2 \frac{dN_{\text{CR}}}{dE_{\text{CR}}} \quad (2.12)$$

An upper bound on the muon neutrino flux is then calculated as

$$E_\nu^2 \Phi_{\text{max}} = \frac{c}{4\pi} E_\nu^2 \frac{dN_\nu}{dE_\nu} \approx 1.5 \times 10^{-8} \text{ GeV cm}^{-2} \text{ s}^{-1} \text{ sr}^{-1} \quad (2.13)$$

A correction factor is then calculated to account for the CR source evolution with redshift, CR energy loss due to redshift and pair production, and neutrino energy loss due to redshift. This results in a factor 3 increase to the muon neutrino flux. Finally, accounting for neutrino flavour oscillations, the upper bound on muon neutrino flux at earth becomes

$E_\nu^2 \Phi_{\text{WB}} = 2.25 \times 10^{-8} \text{ GeV cm}^{-2} \text{ s}^{-1} \text{ sr}^{-1}$  [20] [25]. It is noted that the WB bound is valid also if there are strong magnetic fields confining protons to the source region [26]. In that case neutrons produced in  $p\gamma$  interactions escape the source area and later decay producing CR protons.

### 2.2.3 Active Galactic Nuclei as neutrino sources

AGNs are the brightest sources in the universe that emit continuous electromagnetic (EM) radiation. The generating process of an AGN is believed to be the accretion of matter by a supermassive black hole at the centre of the galaxy and the release of gravitational energy.

AGNs emit EM radiation over a wide wavelength range from radio to gamma rays, with variability observed in all wavelengths and with various time scales. AGNs are typically divided to radio-quiet and radio-loud galaxies and to further subcategories. One group of radio-loud (luminosity from jets and lobes is dominant) AGNs is blazars, objects that show rapid variability and the jets are assumed to be pointing close to the direction of the observer. Detected EM emission can be highly polarised and a characteristic double hump spectrum is observed.

Many models exist to explain blazar activity. These can be divided into two groups: leptonic and hadronic. Any model has to reproduce the observed gamma ray signal and double hump structure in the EM spectrum in order to be relevant.

The leptonic models assume that protons are not accelerated to energies high enough to have efficient  $p\gamma$  interactions. Assuming X-ray photons of 1keV and the centre of mass energy needed for  $p\gamma$  pion production then the threshold proton energy for pion production is around  $10^{15}$ eV. Instead, AGN radiation originates in relativistic electrons. The double hump structure in this case is due to photons originating in the jet (synchrotron) or externally (accretion disk) being boosted to higher energies in inverse Compton collisions with the electrons that are accelerated in the jet.

Due to the absence of high energy protons above the  $p\gamma$  or  $pp$  pion production threshold, leptonic models do not predict a UHE neutrino flux. Hadronic models assume that a significant fraction of the jet kinetic energy is used for proton acceleration to relativistic energies. The distinction is made between  $pp$  and  $p\gamma$  as dominating interactions.

One example for a  $p\gamma$  interactions hadronic model is the Synchrotron Proton Blazar (SPB) model by Muecke et al [27]. In this model protons are co-accelerated with electrons in the jet region but the energy density of the protons is much higher. Charged UHECR protons are produced close to the source via the decay of escaping neutrons. The associated neutrino flux is proportional to the measured extra galactic UHECR flux. The lower frequency hump of the EM spectrum (X-ray) originates in the electron's synchrotron radiation. The higher frequency hump (TeV) originates mostly from synchrotron radiation of relativistic protons and with contributions from neutral pion decay and induced cascades, and muon synchrotron emission. Large magnetic field are required in the SPB model to allow the proton synchrotron emission to reproduce the high frequency hump. A diffuse neutrino flux at earth from BL Lac blazars population was calculated using the model. The flux peaks around  $10^8$ GeV at about an order of magnitude lower than the WB bound.

### 2.2.4 Gamma Ray Bursts as neutrino sources

GRBs are the most luminous, high energy explosions in the universe. GRBs appear isotropically all over the sky in distant galaxies in regions with active star formation. Their time duration spans from ms to several minutes. The initial gamma ray signal is often followed by emission in longer wavelengths when the GRB ejecta interacts with interstellar gas (the afterglow). Short

duration bursts are believed to result from massive stellar core collapse into a neutron star or a black hole, while long duration bursts are associated with merging binary systems.

The general model for the massive core collapse case assumes relativistic jets emerging from the stellar envelope following the collapse. The observed gamma rays are produced by synchrotron emission and inverse Compton scattering on accelerated electrons by shocks in the jet flow [28]. Protons are similarly accelerated and a neutrino flux accompanying the GRB burst is produced via  $p\gamma$  interactions.

Razaque, Meszaros and Waxman use the general GRB model to calculate expected neutrino fluxes associated with the different stages of the GRB event: a precursor signal taking place 10-100s before the bright burst and prompt flux coinciding with the burst. [28]. While the jets are still inside the star, shock accelerated protons may interact with X-ray photons to produce pions, resulting in a  $\sim$ TeV neutrino precursor signal. The prompt neutrino flux mentioned above is of energies  $\gtrsim 100$  TeV. The model is similarly used to determine neutrino fluxes from core collapses in which the jets do not fully emerge from the stellar envelope and the events are not categorised as GRBs. The escaping neutrino flux is then the sole signal from such core collapse events.

### 2.2.5 Cosmogenic neutrinos

During propagation in the cosmos UHE protons with energies above  $\approx 10^{20}$  eV may interact with low energy photons of the Cosmic Microwave Background (CMB) or Cosmic Infrared Background (CIB) radiation via  $p\gamma \rightarrow \pi^+ n$  or  $\pi^0 p$ . The charged and neutral pion decays produce UHE neutrinos and photons. These interactions degrade the proton energy and therefore a decrease in the UHECR flux at energies above the threshold is expected, the so-called GZK cutoff [13]. The predicted UHE neutrino flux is referred to as GZK or cosmogenic neutrinos.

The CMB spectrum is approximately a 2.72K temperature black body radiation spectrum with average photon energy of  $\langle \epsilon \rangle = 6.4 \cdot 10^{-4}$  eV. The injected UHECR proton spectrum is usually assumed to be a power-law with a cut-off energy,  $dN/dE \propto E^{-\alpha} \times \exp(-E/E_c)$ , with typical values  $\alpha = 2$  and  $E_c = E^{21.5}$  eV. The centre of mass of the  $p\gamma$  collision has to satisfy  $s \gtrsim (m_p + m_\pi)^2$  to allow pion production. For a head-on collision the proton's threshold energy is then  $\approx 10^{20}$  eV.

A rough estimate of the interaction path length  $\lambda_{\text{GZK}}$  can be calculated by assuming the interaction cross section and photon density are constants [22]. The respective values are  $\sigma_{p\gamma} = 0.25$  mb and  $n_\gamma = 411 \text{ cm}^{-3}$  and the interaction path length is then

$$\lambda_{\text{GZK}} = (n_\gamma \sigma_{p\gamma})^{-1} \approx 3 \text{ Mpc}. \quad (2.14)$$

A more precise calculation for the proton threshold energy for the interaction takes into ac-

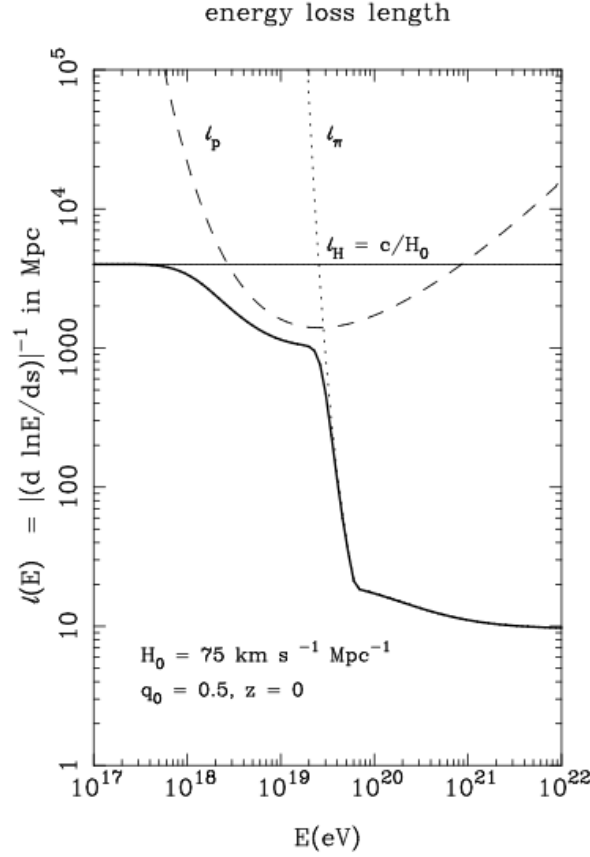


Figure 2.4: UHE protons attenuation length as a function of energy. Solid line refer to proton attenuation length due to pion production ( $l_\pi$ , which dominates) as well as pair production ( $l_p$ ) and expansion losses. Plot taken from [29].

count the shape of the CMB spectrum  $f(\epsilon_\gamma)$  and the detailed  $p\gamma$  cross section  $\sigma_{p\gamma}(E_p, \epsilon_\gamma, \cos(\theta))$  where  $\theta$  is the angle between the proton and photon in the lab frame and which includes direct, resonance and multi-pion contributions. The effective energy threshold is then decreased to  $E_p \approx 10^{19.6} \text{ eV}$ . The interaction length is then calculated by

$$\lambda_{\text{int}}^{-1}(E_p) = \frac{1}{2} \int d\cos(\theta) \int_0^\infty d\epsilon_\gamma \sigma_{p\gamma}(E_p, \epsilon_\gamma, \cos(\theta)) f(\epsilon_\gamma). \quad (2.15)$$

The attenuation length can be approximately calculated by multiplying the integrand by an inelasticity factor,  $K_p(E_p, \epsilon_\gamma, \cos(\theta)) \equiv 1 - E'_p/E_p$ . The inelasticity is about  $m_\pi/m_p \approx 1/7$  at the interaction energy threshold, increasing with higher energies and asymptotically reaching  $1/2$ . Figure 2.4 shows the attenuation length dependency on the proton energy (solid line). The attenuation length above  $10^{19} \text{ eV}$  decreases dramatically with the increasing inelasticity factor and cross section. The slope changes at about  $10^{20} \text{ eV}$  and the attenuation length shows a slower decrease up to about  $10^{20.5} \text{ eV}$  (increasing inelasticity and decreasing cross section) which afterwards remains fairly constant.

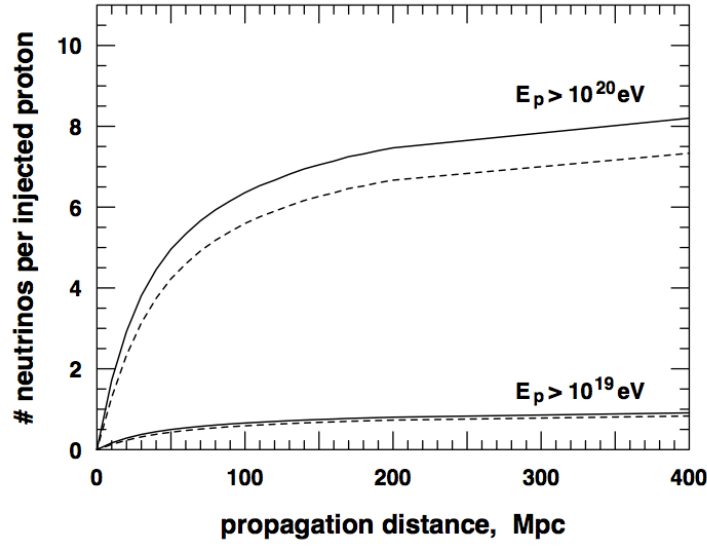


Figure 2.5: Total number of produced GZK neutrinos per proton as a function of its propagation distance. Lower curves for protons of energy above  $10^{19}$  eV and upper curves for protons of energies above  $10^{20}$  eV. Solid lines signify created  $\nu_\mu, \bar{\nu}_\mu$ , dashed lines created  $\nu_e, \bar{\nu}_e$ . Proton injection power-law flux of  $E^{-2}$  with a cut-off energy of  $10^{21.5}$  eV is used for this calculation. Plot taken from [30].

Protons with  $10^{21}$  eV injection energy will on average interact more than twice in the first 10 Mpc of propagation and would lose about half of their initial energy. UHECRs above the GZK interaction energy threshold lose energy over a distance of  $\sim 20$  Mpc, so only UHECRs originating from sources at distance  $\sim 50$  Mpc or less can be detected on Earth [31]. The relatively short interaction path length means that UHECRs interact within a short distance from their source (in comparison to the distance from the source to Earth that can be few orders of magnitude larger), and so cosmological neutrinos point back to the direction of the UHECRs sources. Figure 2.5 shows the total number of created neutrinos as a function of the proton propagating distance, demonstrating that the detected neutrino spectrum from UHECR proton sources at 200 Mpc distance will be fully evolved. It is also demonstrated that it is the more energetic protons that are important for neutrino production hence the significance of the injection cut-off energy. Given this relation, the detection of GZK neutrinos will help to determine the location and nature of the most powerful CR accelerators in the universe.

Calculation of the expected cosmogenic neutrino flux is dependent on the characteristics of the injection proton spectrum (power law spectral index and high energy cutoff value), the distribution of UHE proton sources and cosmological evolution. The resulting  $\nu_\mu - \bar{\nu}_\mu$  spectra has a single peak between  $10^{18}$  eV and  $10^{19}$  eV. The cosmogenic  $\nu_e - \bar{\nu}_e$  exhibits a two peak structure, a higher energy one of mostly  $\nu_e$  from charged pion decay (similarly as the  $\nu_\mu$  peak) and a lower energy one between  $10^{16}$  eV and  $10^{17}$  eV of  $\bar{\nu}_e$  from neutron decay. Neutrons of energy lower than  $10^{20}$  eV are more likely to decay than to interact.

The GZK neutrino by Engel, Seckel and Stanev (ESS) published in 2001 is usually considered as a baseline model [30]. ESS used the measured cosmic ray flux on earth at  $10^{19}$  eV for the normalisation of their injection flux. An update of this model by Seckel and Stanev was presented in 2008 (SS08) [32], taking into account HiRes and Auger UHECR spectrum measurements and new normalisation of CR injection spectrum with accounting for CR propagation and cosmological evolution. Mixed composition as well as an all-proton hypothesis models are reported.

The flux models presented by Ahlers et al. in 2010 [33] use diffuse gamma-ray flux measurements by the Fermi large area telescope to constrain the cosmogenic neutrino production rate. It is assumed that the diffuse gamma-ray flux originates from electrons, positrons and gamma-rays that are co-produced with cosmogenic protons. Subsequent interactions with the CMB and intergalactic magnetic fields create cascaded, thus randomising the direction of the resulting gamma-rays and decreasing their energy. The implication of the cross-over energy between galactic and extra galactic CR contribution is also assessed (the  $E_{\min}$  model parameter). The neutrino flux is required to be smaller when the gamma-ray bound is applied and relatively low cross-over energy has a decreasing effect on the flux.

In case of an injection spectrum of UHECRs with a heavy composition, the nuclei go through photodisintegration processes when interacting with CMB and CIB photons. A nuclei would undergo many reactions during propagation, cascading in atomic number and charge and generating UHE protons, neutrons and alpha particles. In consequence, the cosmogenic neutrino flux expectation is lower in the heavy composition case than in the proton UHECR scenario. The neutrino flux spectrum from UHE iron nuclei was calculated by Ave et al. [34]. The iron-induced neutrino spectrum reproduces the double peak structure existing in the UHE proton case, with a third peak around  $10^{14}$  eV of  $\nu_e$  originating from neutron decays of neutrons emitted by the disintegrating nuclei.

Figure 2.6 shows a comparison of GZK neutrino flux predictions from the models described above. Flux models contain curves for produced  $\nu_\mu$  and  $\bar{\nu}_e$  (such as for the ESS01 and SS08 models) or a single curve for the total neutrino flux prediction (as in the Ahlers models). In any case neutrino flavour oscillations over a cosmological distance need to be considered when interpreting the flux models to event rates on earth (see section 2.2.1).

## 2.3 Atmospheric muons and neutrinos

Muons and neutrinos are produced by CR interactions with the atmosphere and constitute the main background for an UHE neutrino search. The main effort of any neutrino search is effectively rejecting the atmospheric muon flux that is higher by a factor of  $10^6$ . Atmospheric neutrinos, however, compose an irreducible background.

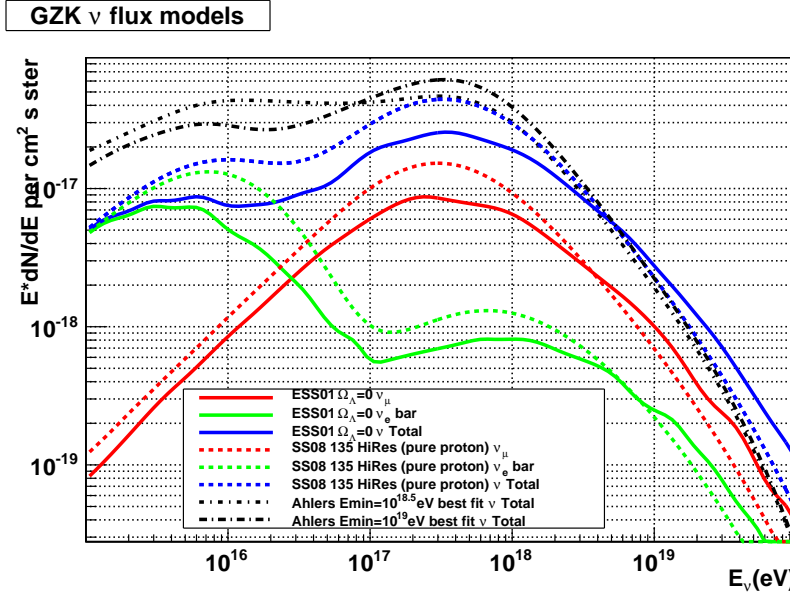


Figure 2.6: UHE neutrino flux predictions from different GZK theoretical models.

### 2.3.1 Atmospheric air showers

An atmospheric air shower is initiated by a single charged CR particle interacting with nuclei in the earth's atmosphere. The initial reaction produces secondary particles that interact as well, creating a cascade of particles through production and decay channels. Muons and neutrinos are produced in decays of charged mesons (pions, kaons, and at very large energies charmed mesons), electrons positrons and photons originate from cascades initiated by decay of neutral and charged mesons. UHECR induce extensive air showers in which the secondary particles are of very large energy and reach the earth's surface where the spread of the shower can be of a  $>10$  km scale. However, muons and neutrinos are the most abundant particles reaching the earth's surface and the only ones that survive at large depths. The shower has a hadronic component (see hadronic showers section 2.4.2) and an electromagnetic one (see electromagnetic showers section 2.4.1). The hadronic core at the centre of the shower can include a large number of muons that typically retain the direction of the initial CR, typically called a *muon bundle*. Induced electromagnetic cascades tend to spread out of the shower core. A schematic view of air shower development is shown in Figure 2.7. Some of the produced muons may decay before reaching the surface, producing muon and electron neutrinos. This contribution is substantial only up to muon energies of few GeV so not important for this work.

### 2.3.2 Conventional atmospheric neutrinos

The atmospheric neutrino spectrum can be divided into two contributions, neutrinos originating from pion and kaon decays referred to as the conventional component, and neutrinos from

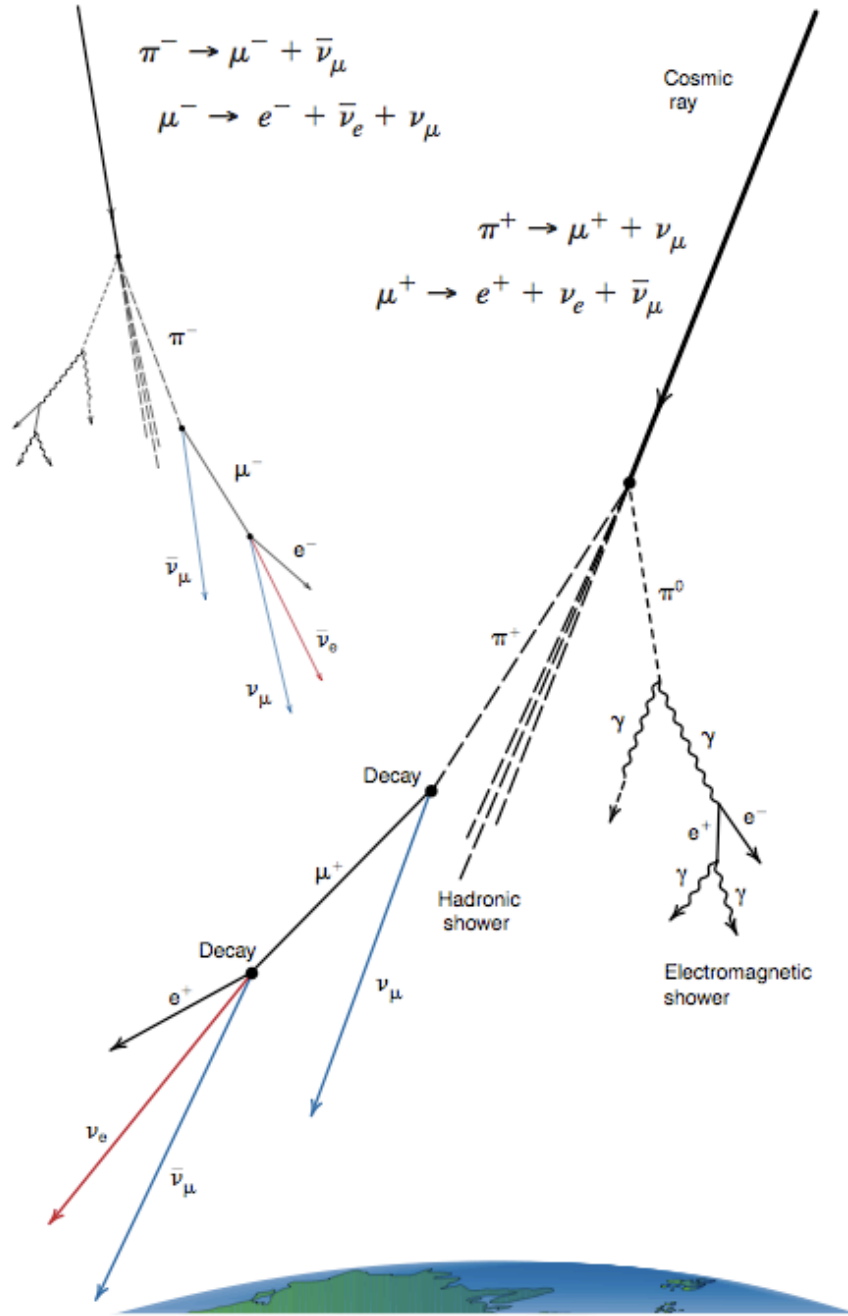


Figure 2.7: Extensive air shower scheme taken from [35].

charmed meson decays referred to as the prompt (charm) component. The steeply falling conventional component dominates up to about 0.1-1PeV where the hard flatter prompt component emerges [36].

Neutrinos from pion decay dominate up to the TeV range where contributions from kaons are important. The conventional flux is then dominated by  $\nu_\mu$  and a neutrino-antineutrino

asymmetry is present due to the strong majority of positively charged CRs. With increasing energy the interaction probability for pions and kaons also increases. For particles traversing a given medium the energy for which the decay length and interaction length are equal is called the critical energy,  $E_{\text{crit}}$  (we note that  $E_{\text{crit}}$  have several different definitions, other definitions are more useful for muons and electrons [10]). The interaction length is dependent on the medium density and the particle's cross section (which is dependent on its energy) while the decay length is dependent solely on the particle's energy. For mesons traversing the atmosphere an isothermal atmospheric density distribution is often assumed for  $E_{\text{crit}}$  calculations [37]. Typical values of  $E_{\text{crit},\pi} = 115\text{GeV}$  for pions and  $E_{\text{crit},K} = 850\text{GeV}$  for kaons are obtained. Above these energies the particles are more likely to interact with the air nuclei than to decay. This creates an energy dependent reduction in muon and neutrino production resulting in an increase of 1 in their power law spectral index compared to the generating CR flux,  $\gamma = 2.7 \rightarrow \alpha = 3.7$  for energies above  $\sim 1\text{TeV}$  [10]. This effect is zenith angle dependent and is less strong for near horizontal events due to their large path length in the low density upper atmosphere. So while the flux of the CR primaries is isotropic, the conventional neutrino atmospheric flux exhibits a complicated zenith dependency due to the interplay between meson decay and interaction in the atmosphere. The conventional atmospheric neutrino flux model used in this work was developed by Honda et al. [38].

### 2.3.3 Prompt neutrino component

In the case that the CR generating an air shower is of very high energy, charmed mesons and baryons can be generated in the shower ( $D_0, D^\pm, D_s, \Lambda_c^+$ ). The life time of these particles is very short and their critical energy is very high at  $E_{\text{crit}} > 10^7\text{GeV}$ , so that they rapidly decay, generating isotropic muon and neutrino prompt fluxes that have a harder spectrum than the conventional one. Neutrinos and muons are produced in semi-leptonic decay modes, such as

$$\begin{aligned} D_0 &\rightarrow K^- + l^+ + \nu_l \\ D^+ &\rightarrow \bar{K}^0 + l^+ + \nu_l \\ \Lambda_c^+ &\rightarrow \Lambda_0 + l^+ + \nu_l \end{aligned} \tag{2.16}$$

The decay branching fractions for electron and muon flavours are equal giving the same prompt flux for  $\nu_e$  and  $\nu_\mu$  while the  $\nu_\tau$  flux is more than an order of magnitude lower. The transition between  $\nu_\mu$  conventional to higher contribution of prompt flux is at about  $300\text{TeV}$ , while the transition in the  $\nu_e$  flux is at much lower energy at about  $10\text{TeV}$  due to the lower  $\nu_e$  conventional flux. A comparison of conventional and prompt  $\nu_\mu + \bar{\nu}_\mu$  flux models for vertical and horizontal zenith angles is presented in Figure 2.8. The atmospheric neutrino prompt flux component model used in this thesis work was derived by Enberg et al [36].

We note that neutrino oscillations for a baseline in the order of the diameter of the earth ( $\sim 12,000\text{ km}$ ) are negligible for energies much greater than  $50\text{GeV}$ . This is clear from the

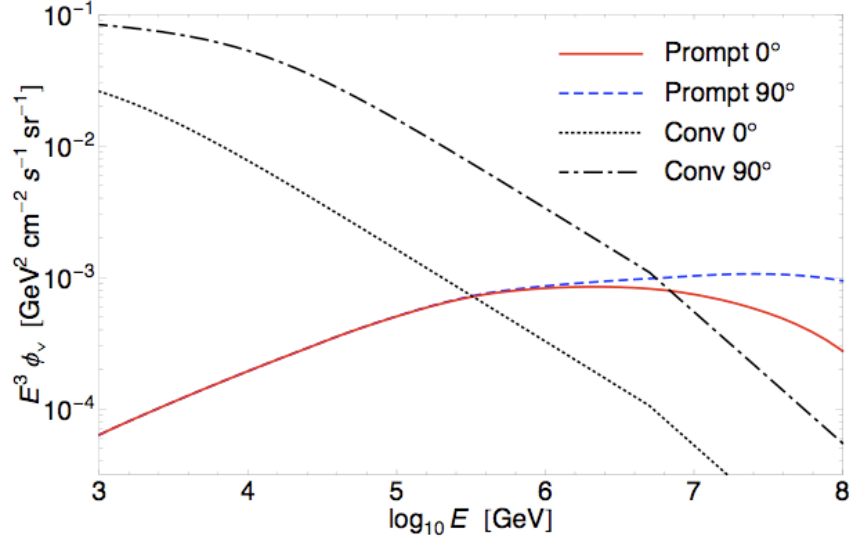


Figure 2.8: A comparison of atmospheric conventional and prompt  $\nu_\mu + \bar{\nu}_\mu$  fluxes. The conventional contribution is modelled by Honda et al. [38] while the prompt contribution is calculated by Enberg et al. [36]. Plot taken from [36].

oscillation frequency calculated approximately by

$$\frac{\Delta m_{ij}^2 L}{4E} \approx 1.27 \Delta m_{ij}^2 (\text{eV}^2) \frac{L(\text{km})}{E(\text{GeV})} \quad (2.17)$$

where the squared mass difference between flavours is  $\approx 10^{-3} \text{eV}^2$ .

## 2.4 Neutrino interactions

Neutrinos interact solely via the weak force. For astrophysical high energy neutrinos, interactions are Deep Inelastic Scattering (DIS) processes. Neutrino-nucleon interactions can be of Charged-Current (CC) type, with the exchange of  $W^\pm$  boson or of Neutral-Current (NC) type with the exchange of a neutral  $Z^0$  boson.

$$\nu_l(\bar{\nu}_l) + N \rightarrow l^- (l^+) + X \quad (\text{CC}) \quad (2.18)$$

$$\nu_l(\bar{\nu}_l) + N \rightarrow \nu_l(\bar{\nu}_l) + X \quad (\text{NC}) \quad (2.19)$$

$l$  stands for a lepton and the subscript stands for the corresponding lepton flavours,  $N$  is a nucleon and  $X$  a hadronic interaction product. For example, a muon neutrino interacting through CC with one of the ice's nuclei will result in a muon. In detail, the  $W$  or  $Z$  couples with one of the quarks in a proton or neutron that forms the atomic nuclei. The CC changes the type of quark. High enough energy may be transferred to the scattered quark, dissociating it

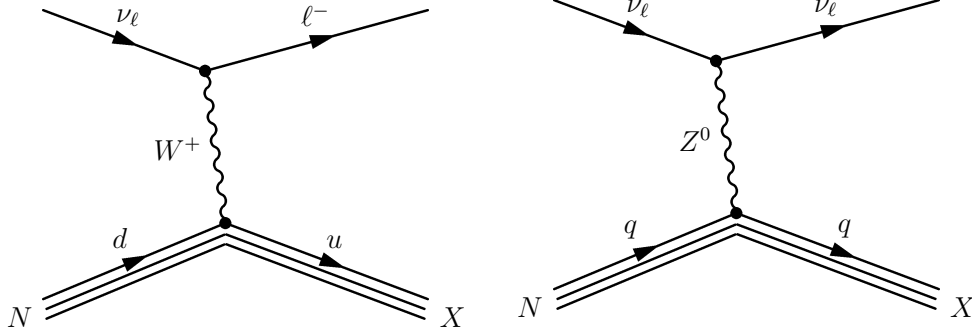


Figure 2.9: Feynman diagrams for neutrino deep inelastic charged current (left) and neutral current (right) interactions.

from the nuclei and creating an hadronic shower. The Feynman diagrams describing these two processes are given in Figure 2.9.

There is one neutrino-electron process that is relevant for astrophysical neutrino energies. Energetic enough electron anti-neutrinos can interact with electrons at rest to produce a real W boson via the so-called Glashow resonance [39] :

$$\bar{\nu}_e + e^- \rightarrow W^- \quad (2.20)$$

with a cross section of about  $5 \times 10^{-31} \text{cm}^2$ , about two orders or magnitude higher than the CC cross section. The invariant mass of the collision has to allow the creation of the W boson with its rest mass of  $M_W = 80 \text{GeV}$ , requiring a  $\bar{\nu}_e$  incoming energy of

$$E_\nu = \frac{M_W^2}{2m_e} \approx 6.3 \times 10^6 \text{GeV}. \quad (2.21)$$

The W boson decays into hadrons or leptons. The Glashow resonance should be easily apparent above the standard cross section in IceCube's data. It is suggested that the Glashow resonance may help to distinguish between pp and pγ type sources of extra-galactic diffuse neutrino flux because a smaller flux of  $\bar{\nu}_e$  exists in the case of pγ processes [40].

The neutrino-nucleon interaction cross sections for CC and NC as a function of  $E_\nu$  are presented in Figure 2.10. The cross sections increase with energy. The neutrino cross section is slightly higher than that of the anti-neutrino [41] for the following reason: the total angular momentum from the spins of an antineutrino and a quark is +1 while for neutrino and a quark it is 0. As the total angular momentum for the antineutrino case is non zero, high scattering angles are suppressed. The corresponding contributions from the scattering on antiquarks are small. This is because most of the nucleon momentum is carried by the valence quarks and only a small fraction by antiquarks from the sea quarks. CC interactions are more likely than NC ones as the W boson coupling to fermions is higher than the Z boson one [10].

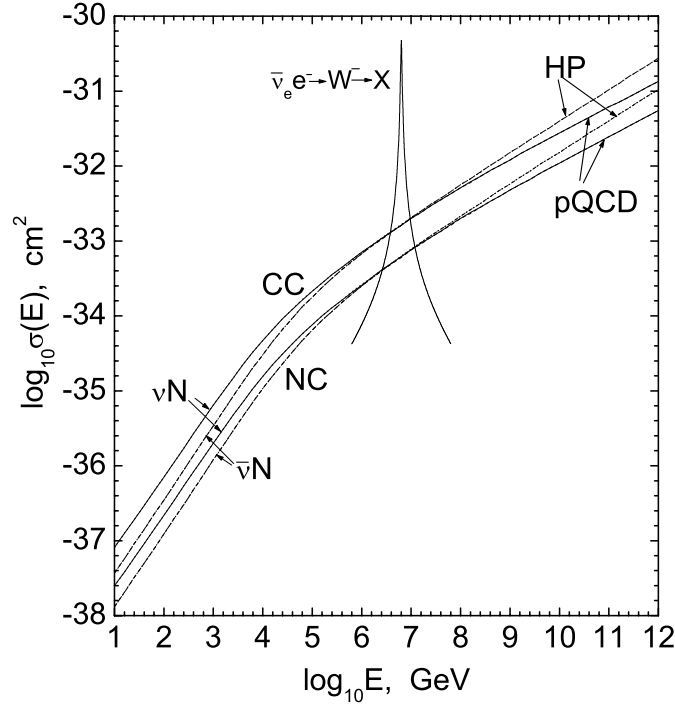


Figure 2.10: Neutrino and anti neutrino cross sections of CC and NC interactions. The Glashow resonance is depicted separately. The HP [42] and pQCD [43] models use different extrapolation techniques for the unknown PDFs shapes. Plot taken from [44].

Calculations of neutrino-nucleon DIS cross sections are dependent on Parton Distribution Functions (PDFs) of the nucleon. Typically DIS involves very large values of  $Q^2$ , the 4-momentum transfer squared, and very small values of Bjorken  $x$ , the fraction of the momentum of the interacting nucleon taken by the scattered quark. The highest values of  $Q^2$  and lowest values of  $x$  were measured at the HERA particle accelerator. The HERA data were used by the CTEQ collaboration for neutrino-nucleon cross section calculations [43]. These results are represented in Figure 2.10. The cross section's uncertainty increases with energies  $> 10^8 \text{ GeV}$  as the relevant PDFs shape is unknown and calculation becomes very model dependent. The two models presented in Figure 2.10 differ by a factor 2 at  $E_\nu = 10^{12} \text{ GeV}$ . New cross sections based on Zeus PDF fits were calculated by Cooper-Sarkar and Sarkar [45] and are used for MC neutrino simulations for this analysis work. The new results show a less steep rise of the cross sections at the highest energies compared to the previous calculations shown in Figure 2.10.

### 2.4.1 Electromagnetic cascades

Electromagnetic (EM) cascade is a process involving electrons, positrons and photons. An initiating particle loses energy by creating secondary particles via bremsstrahlung or pair

production process. Many more particles are produced in subsequent steps of the same mechanism until the created photons are not energetic enough to allow pair production.

As mentioned earlier, a neutrino-induced electron initiates an EM cascade shortly after its production. Electromagnetic cascades can also be initiated by the energetic photons and electrons emitted in stochastic muon or tau energy losses: bremsstrahlung,  $e^+e^-$  production and photo-nuclear interactions. Charged particles in the EM cascade emit Cherenkov light that can be detected. Studies showed that the total Cherenkov light output in the EM cascade is approximately proportional to the total track length for all charged particles in the cascade [46]. The total track length itself is proportional to the cascade's initiating particle's energy  $E_0$ .

An effective total track length was defined and parametrized as [46]:

$$L_{eff} = 0.894 \times E_0(\text{GeV}) \times 4.889[\text{m}] \quad (2.22)$$

### 2.4.2 Hadronic cascades

Neutrino-nucleon CC and NC interactions will result in hadronic cascade: the produced hadrons in their turn interact with other nuclei producing more hadrons and subsequently a cascade. Hadronic cascades can be initiated at a later stage as well - from stochastic energy losses of muon or tau leptons (photo-nuclear) or from hadronic decay of the tau. In atmospheric showers an initially developed hadronic cascade ultimately creates an EM cascade where most of the energy is dissipated.

Hadronic cascade development fluctuates much more than that of EM cascade as it can vary a lot with the type of particles produced. In general it produces less Cherenkov light than an EM cascade. The effective track length for an hadronic cascade was parametrized as [46]:

$$L_{eff} = 0.86 \times E_0(\text{GeV}) \times 4.076[m] \quad (2.23)$$

## 3 The IceCube neutrino observatory

Neutrinos are charge-less, interact only through the weak force and have very small cross section which makes them difficult to detect. Neutrino detectors therefore have a very large detector volume in order to achieve a satisfying event rate. Neutrino telescopes typically use a large body of water or clear ice in which they collect Cherenkov light emitted by secondary charged particles resulting from neutrino-nucleon interaction in the medium. The IceCube neutrino observatory uses this detection technique. IceCube utilises the South Pole transparent ice as neutrino target and detection medium and is made up to trigger for neutrino energies above 10-100 GeV.

### 3.1 Neutrino detection principle

Neutrino detection involves the detection of secondary charged leptons or neutrino-induced cascades. These are recorded primarily by the emitted Cherenkov light (see section 3.1.2) as well as light produced in stochastic lepton energy losses. Other detection methods are possible for neutrinos of energies higher than about 100PeV. The Askaryan effect [47] predicts two types of signal (in addition to optical Cherenkov emission) from neutrino-induced particle cascades: radio-frequencies electromagnetic emission and acoustic wave signal. Radio emission is the detection technique used by RICE [48] and ANITA [49], both taking place at the South Pole, but no neutrino events have been identified so far. The acoustic signal techniques has been studied in water by SAUND [50] and ANTARES [51], and in ice by IceCube [52] including development work for high sensitivity acoustic sensors [53].

#### 3.1.1 Lepton energy loss

Muon propagating through a medium loses energy via several types of processes. The energy deposited in Cherenkov radiation is relatively very small. Energy loss due to ionisation is homogeneous along the muon track (continuous) and the amount of deposited energy is almost constant per unit length. Other stochastic radiative processes include bremsstrahlung,

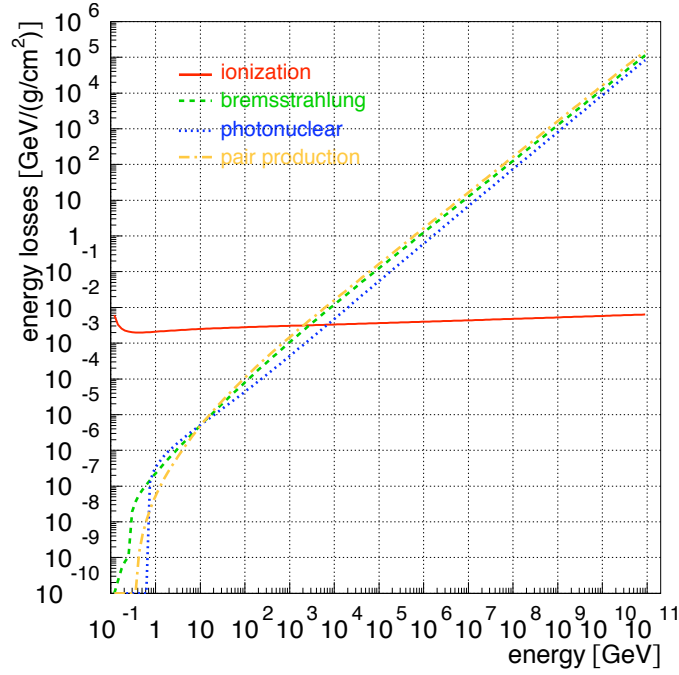


Figure 3.1: Muon energy loss processes in ice vs. muon energy: ionisation (solid), bremsstrahlung (dashed), pair production (dashed-dotted) and photo-nuclear (dotted). Plot taken from [54].

pair production and photo-nuclear interactions. Figure 3.1 shows the muon energy losses by these different processes and their energy dependence. For muons propagating through ice stochastic losses become dominant at energies higher than about  $10^4$  GeV.

The mean energy loss per unit length for energetic charged heavy particles propagating through a medium is described by the Bethe formula. The average rate of energy loss for the high energy muons of  $E > 10^4$  GeV relevant for this analysis work can be parametrized as [10]:

$$-\frac{dE}{dx} = a(E) + b(E)E \quad (3.1)$$

where  $a(E)$  describes ionisation losses and  $b(E)$  describes the sum of stochastic losses.  $a$  and  $b$  are slowly-varying functions (seen in Figure 3.1) and can be assumed to be constant such that

$$-\frac{dE}{dx} \approx a + bE. \quad (3.2)$$

Stochastic losses are dominant at high energies so a constant  $a$  is a good enough approximation. Typical  $a$  and  $b$  values for energetic muons propagating in the South Pole ice were obtained by fitting MC simulated energy loss curves in the range 20 GeV to  $10^{11}$  GeV [54],

giving

$$a = 0.259 \text{ [GeV/mwe]} \quad (3.3)$$

$$b = 3.63 \times 10^{-4} \text{ [1/mwe]} \quad (3.4)$$

where mwe stands for meter water equivalent. Integrating the approximated energy loss (3.2) gives the mean muon range for a muon with initial energy  $E_0$ :

$$x_0 \approx \frac{1}{b} \ln \left( 1 + \frac{E_0}{E_{\text{crit}}} \right) \quad (3.5)$$

where  $E_{\text{crit}} = a(E_{\text{crit}})/b(E_{\text{crit}})$  is the critical energy for which radiative and ionisation losses are equal. For ice this is in the order of  $E_{\text{crit}} \approx 750 \text{ GeV}$  to  $1 \text{ TeV}$ . The mean muon range for a TeV muon is therefore around 2.4km and for a PeV muon the range is above 20km. This means that neutrino-induced muons produced well outside of the instrumented volume of the IceCube detector can reach it and be detected. Detection is done by Cherenkov light and, specifically for high energies as shown above, light emitted in stochastic energy loss processes (bremsstrahlung and Cherenkov light from secondary charged particles).

The dominating energy loss process for electrons is bremsstrahlung. An electron will travel only a short distance in ice before creating an electromagnetic cascade, in comparison to the large muon range of a muon with a similar energy.

Tau leptons are induced by tau neutrinos appearing in UHE astrophysical neutrino oscillations presented in section 2.2.1 or produced as a part of the prompt component of extensive air showers in  $D_s^+ \rightarrow \tau^+ \nu_\tau$  decays presented in section 2.3.3. The tau lepton's lifetime is  $2.9 \times 10^{-13} \text{ s}$ . This gives an approximate tau decay length of  $l_\tau = \gamma c t_\tau \sim 50(E_\tau/\text{PeV}) \text{ m}$ , which is larger than 1km for  $E_\tau \sim 20 \text{ PeV}$  [55]. The tau lepton decays leptonically with 35% branching fraction ( $\tau^- \rightarrow \mu^- + \bar{\nu}_\mu + \nu_\tau$ , and almost as frequently  $\tau^- \rightarrow e^- + \bar{\nu}_e + \nu_\tau$ ), and hadronically with 65% branching fraction ( $\tau^- \rightarrow \text{hadrons} + \nu_\tau$ ) [56]. Tau energy losses processes are dominated by photo-nuclear interactions and pair production [57].

#### 3.1.2 Cherenkov radiation

The principal neutrino detection in IceCube is by Cherenkov light detection. It is emitted by charged leptons produced at neutrino-nucleon CC interactions (section 2.4). The neutrino-nucleon vertex point is seen as the starting point of the lepton track or cascade, if it is in close proximity to the instrumented volume. Cherenkov radiation from an induced lepton is used to track the lepton passage through the ice. Secondary charged particles created in stochastic energy loss processes (important for high energy muons, see section 3.1.1) also in turn produce Cherenkov light which can be detected and used for an event's energy estimation.

A relativistic charged particle traveling through a dielectric medium with a speed greater

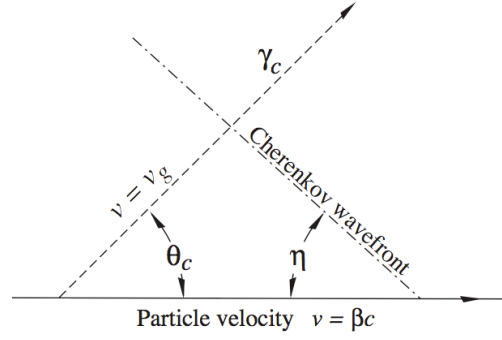


Figure 3.2: Geometry of Cherenkov radiation emission from a charged particle in a dispersive medium [10].  $\eta$  is the opening half-angle of the emission light cone,  $\eta + \theta_c \neq 90^\circ$ .

than the phase speed of light in that medium emits photons. This is the so-called Cherenkov radiation. The charged particle polarises the medium and photons are emitted when the medium's molecules depolarises. A coherent shock front of light is formed, cone shaped, with a characteristic angle  $\theta_c$  depending on the medium's refractive index  $n$ :

$$\cos(\theta_c) = 1/n\beta \quad (3.6)$$

where  $\beta = v/c$  is the ratio between the speed of the particle and the speed of light in vacuum. The refractive index of ice is  $n \approx 1.33$  and the corresponding Cherenkov angle is  $\theta_c \approx 41^\circ$  assuming a relativistic particle ( $\beta \approx 1$ ). A schematic view of the Cherenkov radiation geometry is given in Figure 3.2.

The number of emitted photon per unit track length and wavelength  $\lambda$  is given by the Frank-Tamm calculations:

$$\frac{d^2N}{dx d\lambda} = \frac{2\pi\alpha}{\lambda^2} \left( 1 - \frac{1}{\beta^2 n^2(\lambda)} \right) \quad (3.7)$$

where  $\alpha$  is the fine structure constant. Cherenkov radiation is stronger at short wavelengths due to the  $1/\lambda^2$  dependency. In IceCube the detected wavelengths cutoff is at around 350nm due to the glass housing of the photomultipliers.

### 3.2 Observatory overview

As neutrinos traverse the South Pole ice they may interact with nucleons in the ice, producing secondary charged particles which emit Cherenkov radiation. Capturing this Cherenkov light allows for indirect neutrino detection and track reconstruction. This is the principal of work of the IceCube neutrino observatory at the South Pole.

IceCube consists of an array of strings of Digital Optical Modules (DOMs) embedded in the antarctic ice (in-ice detector) as well as a surface array of DOMs placed in ice-filled tanks

(IceTop). With the detector's construction completion in December 2010, IceCube reached an instrumented volume of 1 cubic kilometer, currently the largest neutrino observatory in the world. The large detector volume is necessary due to the low neutrino interaction cross section and the low predicted astrophysical neutrino flux.

The proof-of-principle for neutrino detection at the South Pole ice was done by the AMANDA detector [58], IceCube's predecessor. AMANDA comprised of 19 strings holding a total of 677 optical modules installed in the ice at depths between 1500m and 2000m. The detector's optical modules spacing and total instrumented size made it suitable for detection of lower energy neutrinos compared to IceCube. AMANDA was collecting data for 13 year before it was decommissioned in 2009.

The completed detector includes 86 strings with each string holding 60 DOMs, giving a total of 5160 DOMs placed in depths of 1450m to 2450m below the surface. Of these, 80 of the strings are placed at 125m distance of each other and neighbouring DOMs on a string are placed with 17m vertical distance. The remaining 6 strings form DeepCore: an inner ring at the centre of IceCube with strings placed more densely with their DOMs placed with smaller spacing at the lower part of the detector where the antarctic ice is the clearest. The surface array IceTop consists of 81 stations placed on top of IceCube strings. Each station includes two ice tanks with each tank housing two DOMs.

A scheme of the IceCube detector is shown in Figure 3.3. The geometry of the IceCube 40-strings detector on the surface is shown in Figure 3.4.

IceCube's main physics goal is the search for high energy neutrino sources, but its physics program is diverse. Other goals are determining the sources of ultra high energy cosmic rays, giving evidence of the energy-release processes that occur at GRBs and AGNs, providing information about dark matter particles existence and constraining neutrino oscillation parameters. IceTop main physics goal is the study of CR energy flux and mass composition at the region of the knee.

The initial detector design was optimised for an energy range of 100GeV to 100PeV [59] though the detector has the capability to detect neutrino energies as high as 100EeV. High quantum efficiency DeepCore strings were added in order to increase the detector's sensitivity to neutrinos of low energies, from  $\sim 10$ GeV [60]. Detection of supernovae neutrinos of few tens of MeV energies is possible by looking at overall detector noise rate [61] or by studying detector hits which are correlated in space and time [62] [63].

In this work data that was taken between April 2008 and May 2009 by the incomplete detector is used. During that time IceCube had 40 operational strings and 40 IceTop stations (IC40). This detector configuration covered half of the complete IceCube hexagon shape giving approximately a rectangular shape with a short and long axes.

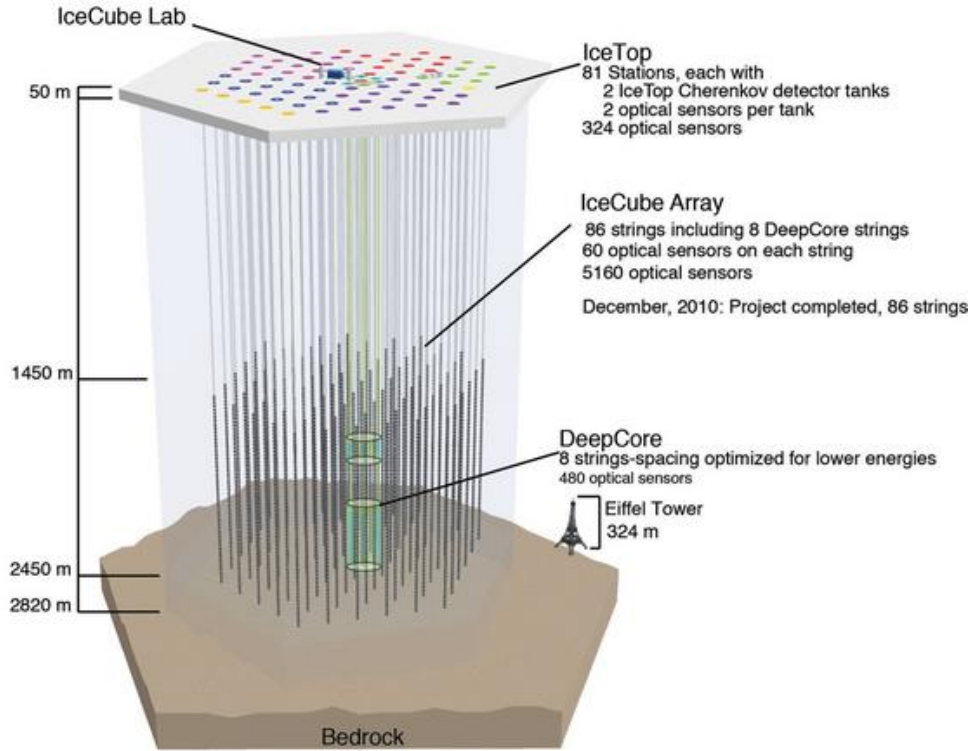


Figure 3.3: The IceCube neutrino observatory. Image credit: Jamie Yang.

### 3.3 The digital optical module

The principal element of the IceCube detector for Cherenkov light detection and data acquisition is the Digital Optical Module (DOM). Its design had to consider the difficult conditions at which the detector is working: negative temperatures down to  $-40^{\circ}\text{C}$ , high pressure up to 400atm during freezing, and the need for highly reliable detector with a life time of at least  $\sim 15$  years as the modules are inaccessible once deployed. The light detector has to function on low power, detect wide dynamic range of number of photon hits and have fast response time with nanoseconds time resolution.

The DOM is an integrated package of a 25cm diameter photomultiplier tube (PMT), high voltage power supply unit, LED flasher calibration board and embedded digital data acquisition system encased inside a thick glass pressure housing [64]. The PMT is held in place and optically coupled to the glass sphere by an optical gel. It is shielded from the earth's magnetic field by a mu-metal cage. The DOM components are used for operating the PMT, amplifying and digitising the PMTs analog pulses, signal filtering and detector calibration. A schematic view of the DOM is given in Fig 3.5

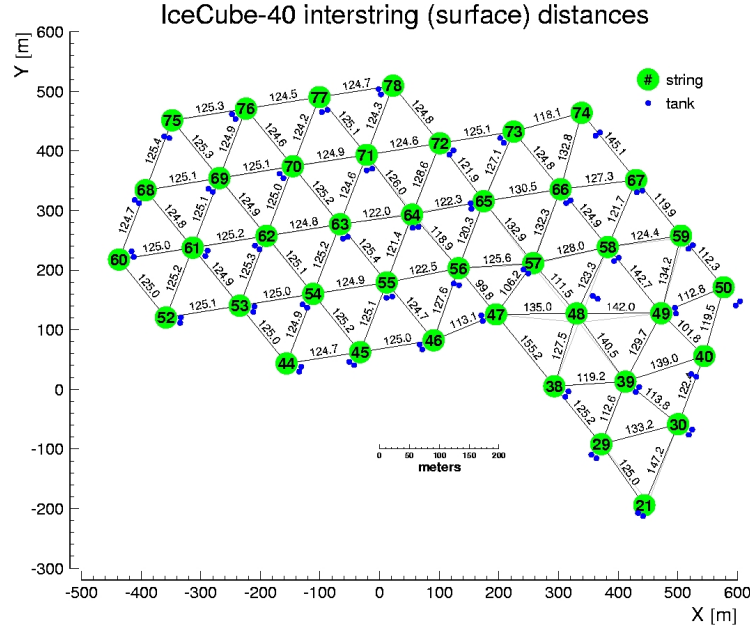


Figure 3.4: The surface geometry of the IceCube 40-strings detector. Image credit: Kurt Woschnagg.

### 3.3.1 The photomultiplier tube

IceCube chose Hamamatsu R7081-02 for the PMT due to its low dark noise rate, high gain and good time and charge resolution for single photons [65]. It is sensitive to light in the wavelength range 300 – 650nm with a peak quantum efficiency of 25% at 390nm, though the glass and optical gel set a short wavelength cutoff at about 350nm. It operates on 1500V which results in nominal gain of  $10^7$  that gives Single Photo Electron (SPE) pulses of 8mV, well observed above electronic noise level (0.1mV).

The PMTs were manufactured with custom low radioactivity glass which resulted in low dark noise rate of 300Hz in the antarctic ice temperatures. A high energy neutrino event can create an optical signal of  $3\mu\text{s}$  but most of the information is contained within its first 300ns. Due to this short time window and low dark rate, only 1% of the induced muons will have a single dark noise photon hit in the 100 DOMs closest to the track. This would have very low impact on track reconstruction.

The PMTs charge resolution from SPE hits was measured as approximately 30%. Including effects from the DOM digitisation and readout electronics the time resolution was measured as 2.7ns with large DOM-to-DOM variations. Simulations show that photon scattering in the ice creates long delays in photon arrival time with 40% of photons delayed by at least 5ns for 10m traveling distance [66]. This photon delay then constitute a much larger effect than the 2.7ns PMT time resolution. On the other hand, PMTs close to an ultra high energy tracks will detect the first arriving photon with a negligible delay, in which case the PMT time resolution

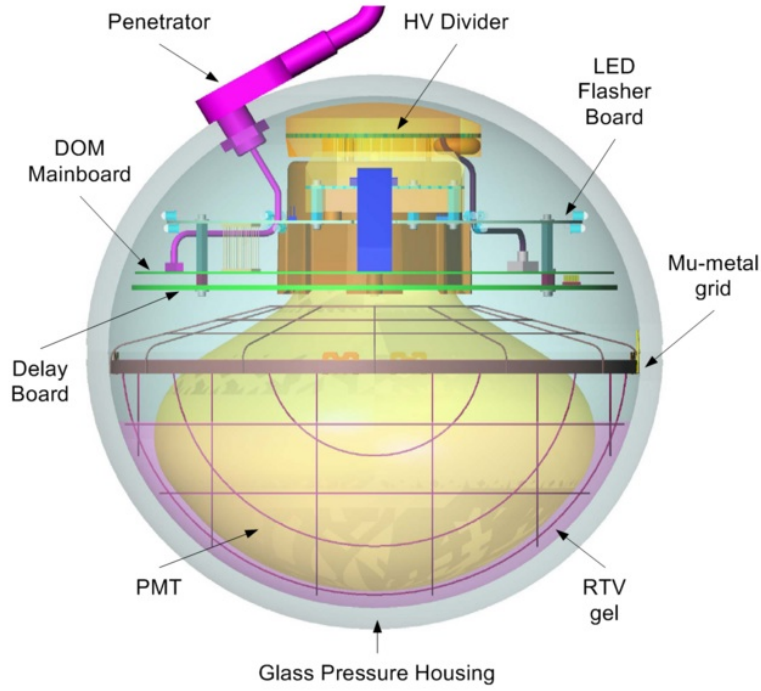


Figure 3.5: Scheme of the IceCube Digital Optical Module unit. Image credit: R. Pearson

becomes important. In practice many reconstruction methods in IceCube use the PMT signal rise time which is produced by the first arriving photons, so based on short delayed photons. As these first photons travel different distances some time delays are expected (see section 4.2.2) depending on the South Pole's ice quality (see section 3.6).

The PMT response is proportional to the number of detected photons up to the nonlinear saturation regime beyond which the PMT response curve flattens. The saturation behaviour is dependent on the PMT work gain and is almost independent of incoming pulse time length. With the  $10^7$  work gain the response is linear up to 50mA current (31 photoelectrons per ns) and saturates at 150mA. MC Simulation studies show that saturated PMTs starts to appear for 600 TeV shower energies and that for a  $\sim 10$  PeV showers most of the PMTs closest to the event are badly saturated. PMT saturation affects the estimation of total charge collected in a PMT waveform but it does not affect event track reconstructions which are based on MPT signal rise time. In IC40 data taking run and this analysis work saturated PMTs are used and treated similarly to unsaturated ones. More work is needed in order to understand better and develop methods to correct for saturated PMTs and obtain an improved charge estimation.

The LED flashers are used for determining the energy scale for event energy reconstruction as well as detector-wide geometry and time calibration and measurement of the properties of the South Pole ice.

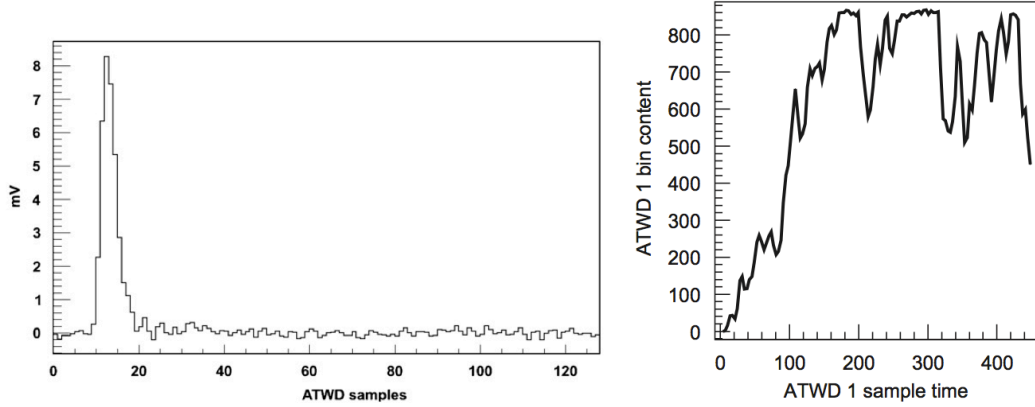


Figure 3.6: PMT ATWD waveform examples. Left: typical single SPE waveform shape. Right: ATWD channel 1 (highest amplification) waveform from light emitted from DOM flasher board which contains some saturated bins ( $x$  axis in [ns]). In this case the ATWD channels 2 is not saturated and voltage values can be read from it (for channel 1 saturated bins). Plots are taken from [67].

### 3.3.2 PMT signal processing

The PMT signal is digitised by two digitising systems on the DOM main board (MB), time stamps are set on the waveforms and they are sent to the surface.

A trigger is issued if the PMT signal exceeds a discriminator threshold which is set to 0.25 SPE in the IC40 data run. Timing on the MB is controlled by a 20MHz quartz oscillator which is doubled to 40MHz [59]. The local time is regularly calibrated with an all-detector time at the surface. The trigger is given a time stamp from the local clock.

The PMT signal is delayed by 75ns by passing on a 11.2m long strip-line on a dedicated delay board [59]. This is done before the signal is reaching the digitisers in order for the rising part of the waveform to be fully recorded. The fast digitiser is implemented in an Analog Transient Waveform Digitiser (ATWD) chip. It has 128 samples and can run between 200 and 700 Mega-Samples Per Second (MSPS). In IC40 The sampling frequency was 300 MSPS which gives 3.3ns bin width and 442ns total time length for the ATWD waveform. The ATWD has four channels, three of which are used for waveform recording while the remaining one is used for calibration and monitoring. The three relevant channels amplify the PMT signal by 16X, 2X, and 0.25X, giving a dynamic range to match the PMT output. In order to minimise dead time, two ATWD chips are installed on the MB and work in ping-pong fashion. Examples of ATWD waveforms are shown in Figure 3.6. A typical single SPE waveform shape is given in the left plot. The right plot contains an ATWD channel 1 (highest amplification) waveform from light emitted from DOM flasher board which contains some saturated bins.

The second method is a fast Analog to Digital Converter (fADC). The fADC collects 256 samples in sampling frequency of 40MSPS which gives a waveform of 25ns bin width and  $6.4\mu\text{s}$  total

time length. The fADC waveform is long enough to fully detect an optical signal arriving to a DOM from the highest energy events. The fADC works with a low dynamic range such that a SPE charge is easily observed (typically 13-count value above the baseline [67]) but the fADC waveform can be saturated at high charge deposits while the ATWD lowest amplified waveform is not.

The PMTs waveforms may include after pulses, a common artefact for such detectors. Accelerated electrons travel between dynodes and ionise residual gases inside the PMT. The produced ions are accelerated towards the photocathode and release photoelectrons when reaching it. The ejected photoelectrons are amplified by the dynode stages, resulting in an after pulse signal which is typically recorded from 300ns to 11 $\mu$ s after the initial pulse. Different after pulse time peaks are associated with different gas ions of different mass and corresponding flight time. After pulses are significant at high energy events as the accumulated charge in them grows linearly with the initial pulse charge (with typically after pulse total charge is 6% of the initial generated one). For such high energy events where the initial pulse waveform is saturated, it was suggested that the after pulses may be used for initial pulse charge estimation. This approach however was not yet developed at the time of this analysis work.

A significant amount of the after pulses time range is within the time length of the fADC waveform (6.4 $\mu$ s) while the ATWD one includes only the very beginning of the after pulses. As the ATWD waveform 442ns time length includes 75ns recorded before the DOM trigger and the initial pulse peak, the after pulses has a minimal affect on the ATWD pulses. However, the IC40 online data processing scripts contained a software bug concerning the fADC pulse processing. Due to that the fADC pulses were discarded and all reconstruction methods and waveform charge estimation were done using ATWD pulses only. For this reason the PMT after pulses is not a concern for this analysis. Future high energy IC analysis may use the after pulses for better estimating the charge in initial saturated pulses by using the fADC waveforms smartly.

In order to reduce noise hits in the data and to avoid detector dead time while processing noise hits, a Local Coincidence (LC) condition is put in place. Each DOM is connected to its two nearest neighbouring DOMs with a copper wire twisted-pair. When a trigger occurs the DOM sends a LC signal to its neighbours. The LC condition is met if in a specific time window, typically smaller than 1 $\mu$ s, at least one of the neighbouring DOMs triggers and sends a response LC signal. The LC signal rate is typically ~10Hz so most of DOM triggers due to dark noise are eliminated. IceCube used a Hard LC (HLC) data collection mode during the IC40 run in which waveforms are digitised and kept only from DOMs that fulfilled the LC condition. In HLC information from isolated triggered DOMs are discarded. In later runs, starting from IC59, a Soft LC mode was implemented. In SLC limited information from isolated triggered DOMs is kept in the form of coarse charge stamp from the fADC's highest samples. However a large fraction of these isolated triggers are caused by noise hits and needs to be identified and discarded on later stages of event processing.

### 3.4 The data acquisition system

The DOMs are connected to the surface with a twisted-pair copper wire which is used for communication, delivering power to the DOMs, time calibration and data transmission. The string's cable connects to a surface junction box (together with cables from two IceTop tanks), which is connected to the counting house at the IceCube Laboratory (ICL).

After the signal digitisation is done at the DOM, the DOM launch information is sent to the ICL. It contains a time stamp from the local DOM clock and ATWD and fADC waveforms (HLC case). At the ICL the DOM launch time stamp is converted to an ICL clock time and all DOM launches from a single string are time-ordered.

Due to storage issues and in order to concentrate on interesting, reconstructible events, a Simple Majority Trigger (SMT) is applied. In IC40, events with 8 or more DOM launches (SMT8) within a time window of  $5\mu\text{s}$  are passed on for further filtering. Otherwise the data are discarded. The kept events are passed on to the Processing and Filtering system (PnF). This is a set of fast reconstructions and filters designed by the different IceCube working groups searching for different signal types. The events that pass at least one of the online filters are kept. Events are transmitted to the north daily via satellite.

### 3.5 Event topologies in IceCube

Events in IceCube are typically categorised as track-like events and cascade-like events. In a track-like event the DOM hits show up as following a track in the ice in their location and time distributions. In the cascade-like event the light emission and detection is roughly spherical and is more localised compared to a track event that can pass along the entire detector. In some cases an event may present a track and cascades DOM hit samples in the detector which is referred to as a composite event. A scheme of the light emission for the muon and track event topologies is given in Figure 3.7.

Neutrino-nucleon interactions in the ice produce hadronic showers. In the Neutral Current (NC) interaction case the produced event will have a cascade-like DOM hit signature located around the interaction vertex. In the Charged Current (CC) case the event topology is dependent on the type of the outgoing lepton which is determined from the incoming neutrino flavour. A  $\nu_\mu$ -induced muon travels through the detector producing a track-like signature. The muon may be produced outside of the detector (through-going track) or inside it (starting track) where an accompanying cascade may be observed at the vertex point making it a composite event. Electrons produced in  $\nu_e$  CC interactions immediately interact in the ice producing electromagnetic cascade giving a clear cascade-like event signature. Events involving  $\nu_\tau$ -induced  $\tau$  leptons generally have a composite event DOM hit signature. A track-like DOM hit pattern is found around the traversing  $\tau$  and cascade-like light emission is found around  $\tau$  production and decay vertices. A decaying  $\tau$  may also produce a charged muon, producing again track-like DOM hits. The length of the  $\tau$  track and the chance to have both

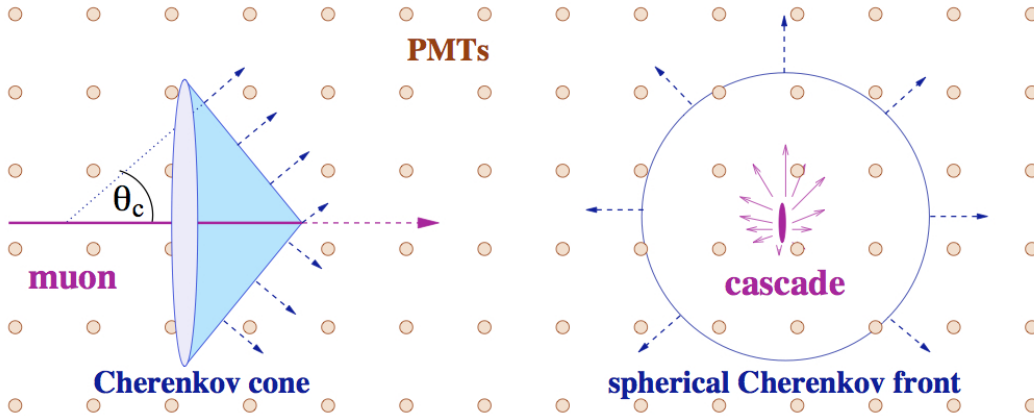


Figure 3.7: Track (left) and cascade (right) event topologies in the IceCube detector, taken from [83].

$\tau$  production and decay occurring inside the detector or not are dependent on the  $\tau$  energy. Events may look like a single cascade at low energy (production and decay vertices inseparable), two separated cascades with a faint track in between in middle energies ("double-bang" events), or "lollipop" if only one of the cascades is contained in the detector) and a simple track event for high energy, long track length  $\tau$  traversing the detector (produced and decays outside of it).

Determination of the event parameters for track-like events is a simpler task than for cascade-like events, with cascades light detection pattern being more sensitive to ice properties. Also, low quality track events may resemble (be confused with) cascade events but this is much less likely the other way around.

### 3.6 South Pole ice properties

Unless otherwise mentioned, the information in this section is summarised from [68], where the optical properties of the South Pole ice are thoroughly discussed.

The requirement from a neutrino Cherenkov detector detection medium is a transparent material with low photon scattering and absorption. The surrounding must also be dark in order to reduce noise and a large volume is desired due to the low neutrino cross section and low flux predictions for high energy neutrinos. The ice sheet at the south pole meets all these requirements, being that the glacial ice is the most transparent solid known for wavelengths between 200nm and 400nm. IceCube's PMT are most sensitive to wavelength's around 390nm, utilising well the transparent ice.

The 2820m thick glacial ice sheet at the south pole was created over a period of 165,000 years [69]. The South Pole ice is not fully homogeneous and clear but its quality is dominated

by dust impurities which variate with depth and, to a lesser extent, horizontally. The dust concentrations are correlated with climatological changes, reflecting the different atmospheric conditions and volcanic eruptions during the ice creation. The temperature of the ice varies between -55C at the surface and previously estimated -9C at bedrock [68], however newer measurements indicate that the bedrock ice temperature is closer to the pressure-induced melting point of -2C. The IceCube detector is installed in depths between 1450m and 2450m. Four distinct dust peaks are found in this region, the largest of them at around 2050m depth.

The optical properties of a medium are described by its amount of scattering and absorption of photons. These are usually quantified by the scattering length  $\lambda_s$  and absorption length  $\lambda_a$ . The first is defined as the average distance a photon will travel in the medium before being scattered and the second is defined as the distance for which the photon's survival probability drops to  $1/e$ . In the glacial ice at the IceCube depths scattering and absorption are predominantly due to the insoluble dust particles. Mie scattering model is used to calculate the light scattering off dust spheres with radius typically larger than the light's wavelength. In a single scattering we refer to the average cosine of the scattering angle  $\theta$  as the anisotropy,  $\langle \cos(\theta) \rangle$ . Mie scattering calculations for IceCube showed that scattering is strongly peaked in the forward direction with  $\langle \cos(\theta) \rangle = 0.94$  and has a weak dependency on light wavelength. It is then useful to describe the South Pole ice in terms of effective scattering length  $\lambda_e$ , which is the average distance at which a photon direction is randomised. Assuming large number of scattering processes  $\lambda_e$  is defined by

$$\lambda_e = \frac{\lambda_s}{1 - \langle \cos(\theta) \rangle}. \quad (3.8)$$

This highly anisotropic scattering case results in  $\lambda_e \gg \lambda_s$ .

Other than dust, another source for scattering in the ice are trapped air bubbles. Early measurements at shallow depths between 800m and 1000m showed large concentration of air bubbles which resulted in very short scattering length [70]. However, as pressure increases with depth, air bubbles compress and go through phase transition to air-hydrates solid state [71]. The refractive index of the air-hydrates is very similar to the one of ice so photons pass through it almost without any scattering. Additional measurements confirmed that at depths greater than ~1500m all bubbles have transformed into the solid phase. We can conclude that for the IceCube detector air bubbles do not contribute to photon scattering.

#### 3.6.1 The ice model

A six parameters "ice model" was constructed to parameterise the effective scattering length and the absorption lengths using Mie scattering assumption. The relevant parameters are the

effective scattering coefficient and absorption coefficient defined by:

$$b_e = \frac{1}{\lambda_e} \quad (3.9)$$

$$a = \frac{1}{\lambda_a}. \quad (3.10)$$

The model fits  $b_e$  and  $a$  at a wavelength of 400nm which is at the peak sensitivity of the IceCube detector, taking into account Cherenkov light wavelength spectrum, the DOM's glass housing transmissivity and the PMT's quantum efficiency:

$$b_e(\lambda) = b_e(400) \left( \frac{\lambda}{400} \right)^{-\alpha} \quad (3.11)$$

$$a(\lambda) = C_{\text{dust}} \lambda^{-\kappa} + A e^{-B/\lambda} (1 + 0.01 \Delta T)$$

$$C_{\text{dust}} = b_e(400) D + E \quad (3.12)$$

The model depends on 6 parameters as well as on the ice's temperature:  $\alpha, \kappa, A, B, D, E$  and  $\Delta T$ . Wavelengths are given in nanometers and temperature in K.

*Scattering*: scattering off dust is power-law dependent on the wavelength with  $\alpha$  close to 1 which exact value depends on dust composition.

*Absorption*: two terms contribute to the absorption coefficient's dependency on  $\lambda$ . The first term describes the absorption due to insoluble dust particles in the ice.  $C_{\text{dust}}$  is proportional to the dust concentration which is depth dependent. It is the dominating term for wavelengths in the region ~200nm to ~500nm. The second term describes absorption by the ice itself. It is an exponential increase in the infrared regime and this term dominates at wavelengths longer than ~500nm. The exponential is corrected with a 1%/K temperature dependence that was observed [72].  $\Delta T$  is calculated relatively to the temperature at 1730m depth. The Urbach tail component (ice absorptivity in wavelengths slightly longer than those corresponding to the ice's band-gap energy) is disregarded here as it is negligible for wavelengths longer than 300nm.

Light from pulsed and steady light sources was recorded by the AMANDA light sensors and used to extract scattering and absorption parameters, resulting in the Millennium ice model. For the installation of IceCube at larger depth, measurements of dust concentrations for depths below 2100m from the antarctic ice core from Vostok and Dome Fuji were incorporated. In addition, systematic studies of the ice model showed a systematic smearing of the dust layers structure. An improved data analysis technique was performed on the AMANDA data making sure the dust layers and clean layers are separated more accurately, resulting in a modified ice model called AHA. However, data collected with the IceCube detector suggests that the deepest ice below the largest dust peak is cleaner than what is modelled in AHA. The AHA ice model was used as the standard for the work detailed in this thesis.

Testing and improving the ice model is an ongoing effort in IceCube. With the recent completion of the detector a new model was developed called Spice-Mie [73]. Data taken using light emission from the DOM's LED flashers, covering the full detector's depth range, were used to fit effective optical ice parameters which include detector efficiencies. Figure 3.8 show the fitted absorption and effective scattering coefficients as a function of depth for the AHA and Spice-Mie models.

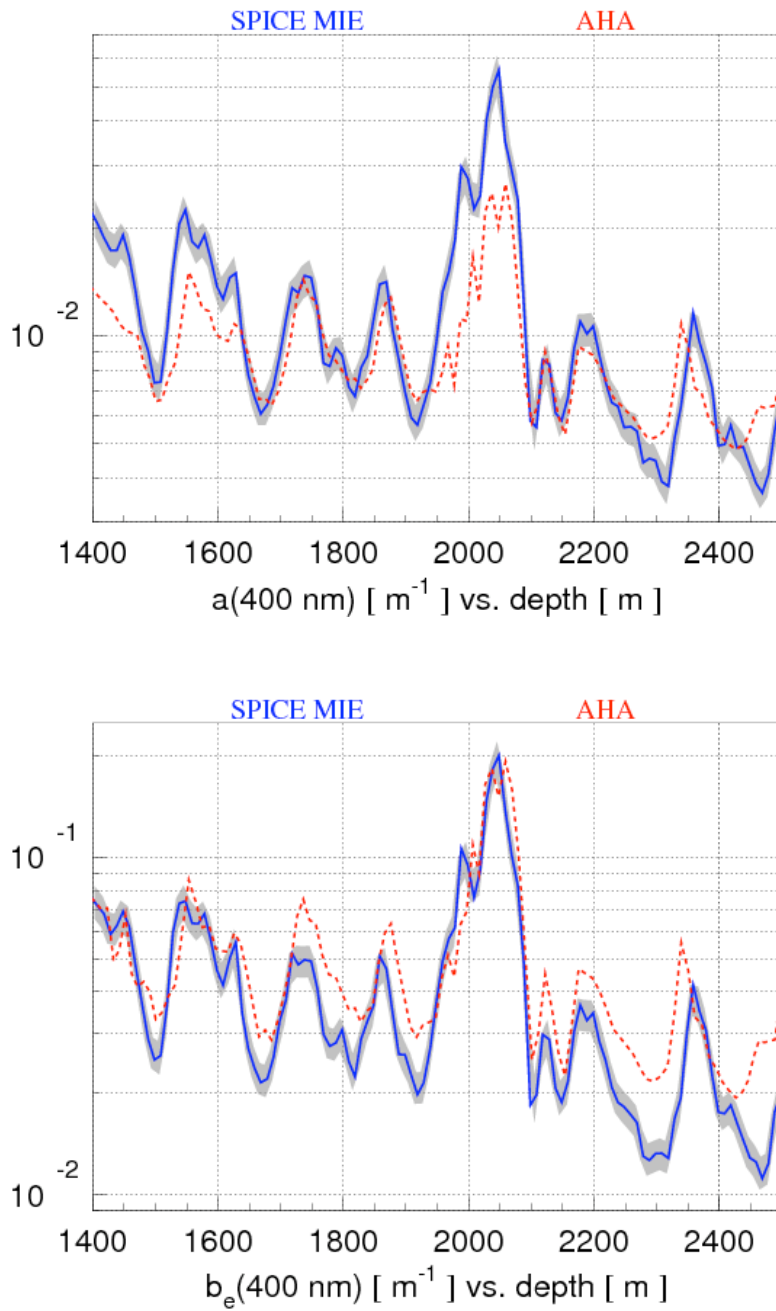


Figure 3.8: Absorption and effective scattering coefficients for 400nm wavelength at IceCube's depth range, as modelled by the AHA and Spice-Mie ice models. Plot adapted from [73].

## 4 Simulation and reconstruction in IceCube

A Monte Carlo (MC) simulation technique is used for generating simulated event samples of expected background and signal types of events. A good description of background event fluxes and understanding of the detector's characteristics and response are needed in order to construct a reliable background rejection method. Simulated atmospheric muon events, which constitute the majority of the background for this analysis, are compared with IceCube data to check the quality of the MC simulation and detector description.

### 4.1 Event simulation

Event simulation in IceCube takes place within a dedicated software framework called IceSim. The simulation chain includes the following elements:

- *Event generation* - Primary particles are created according to chosen flux models. Generated particles are assigned with a particle type, energy, direction of movement and a distance from the IceCube detector.
- *Propagation* - The primary particles are propagated through matter (atmosphere, earth rock and the antarctic ice) taking into account continuous and stochastic energy loss mechanisms and production of secondary particles, which are also propagated. Cherenkov photons emitted by primary and secondary particles are propagated through the antarctic ice.
- *Detector simulation* - The IceCube detector response is simulated including PE hit pattern, PMT response, DOM electronics simulation and the detector's trigger.

Two types of events are generated: atmospheric muons from extensive air showers initiated by UHECR interactions in the atmosphere, and single neutrino events.

### 4.1.1 Atmospheric muon event generation

The CORSIKA event generator (COsmic Ray Simulations for KAscade) [74] is used for extensive air shower simulation. Atomic nuclei from hydrogen (single proton) to iron are simulated and considered as the CR primaries initiating the showers. The primaries are propagated in the atmosphere until they interact with air nuclei or decay, and atmospheric muons and neutrinos are created. The high energy hadronic interactions are described by SIBYLL [75].

The default model for describing the primary CR spectrum in IceCube simulations is the poly-gonato model developed by Hoerandel [76]. The model assumes contributions of nuclei primaries from proton to uranium. In this case the knee in the CR spectrum is due to a rigidity dependent cutoff of the single type nuclei spectra (see section 2.1). The model describes only the galactic origin CR spectrum and so does not reproduce the observed spectrum at the highest energies which is believed to be of extragalactic origin CRs. To account for this shortcoming and to achieve a simulated event distribution closer to the observed one, the extragalactic UHECRs flux is approximated by extending the galactic iron component with a  $E^{-3}$  power law flux (the observed UHECRs flux slope is  $E^{-2.8}$ ). A smaller issue is that primary nuclei only up to iron are simulated by CORSIKA due to technical reasons. Double coincident and triple coincident atmospheric shower events are simulated as well.

The CORSIKA event simulation is done either according to the observed energy spectrum, a power law with index  $\gamma \geq 2.7$ , or with a bias towards production of high energy events by decreasing the power law index by one, giving a flatter flux. Simulated events are then weighted to obtain the observed CR energy spectrum. Efficient simulation of high energy events is important for this analysis work as large statistics of the highest energy muon background events are needed in order to allow the development of reliable background rejection techniques.

A second model of the primary CR spectrum that is used in this work is the 2-component model which assumes CR mass composition of proton and iron mix and was fitted to the KASCADE array measurements [77]. CORSIKA simulation sets of single proton CR showers and single iron CR showers were generated following a  $E^{-2}$  power law spectrum. The sets are then used together and events are weighted according to the 2-component model. These 2-component model simulation sets were shown to describe the experimental data better and have larger statistics than the poly-gonato model MC at the highest energy range as well as at the lowest energies considered in this analysis (see Figure 4.1). The 2-component model is therefore used as the benchmark MC simulation of single CR shower background events.

### 4.1.2 Neutrino event generation

Neutrino generation in IceCube is done with the neutrino generator software package (NuGen) which is based on the ANIS event generator [44]. NuGen makes use of recent calculations of the high energy neutrino cross section based on Zeus PDFs fits [78]. Neutrinos are generated at a random position on the earth's surface and propagated through the earth's rock. Energy loss

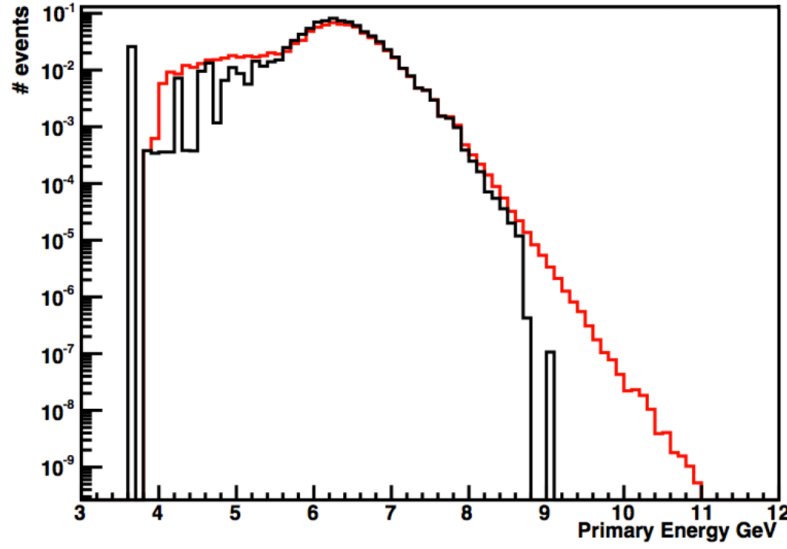


Figure 4.1: CORSIKA poly-gonato (black) and 2-component (red) simulated event rates vs primary energy.

by neutral current interactions and absorption due to charged current interactions are taken into account. The Preliminary Earth Model (PREM) is used to model the earth's structure [79].

Neutrinos that reach the vicinity of the IceCube detector are forced to interact with the antarctic ice producing secondary particles, which in turn emit photons that trigger the detector. Each event is then assigned with a weight representing the probability for that interaction to occur. Neutrino generation for this analysis is done following a  $E^{-1}$  power law which is efficient for HE events. The generated events are then weighted in order to describe the energy spectrum of atmospheric and cosmologic neutrino fluxes. In this work the baseline atmospheric neutrino flux models considered are Honda [38] for the conventional component and Engberg [36] for the prompt one.

#### 4.1.3 Propagation

The Muon Monte Carlo (MMC) software package propagates atmospheric muons and neutrino-induced leptons through the antarctic ice. MMC takes into account continuous and stochastic energy loss processes and deals with propagation of secondary leptons when created. The propagation of Cherenkov photons during simulation is very computationally demanding and consequently a different method is used. The Photonics software package [80] is used for photon propagation in MC simulations based on the ice model coefficient values. In Photonics, photons from a light source are propagated and photon density and time distributions around the IceCube detector volume are calculated. Light density and time distributions for different

light source locations are saved in look-up tables. During event simulation the Photonics tables are read to determine light distributions in the detector volume.

### 4.1.4 Detector simulation

The detector simulation starts with simulating the PMT response to the photon density at the DOM location as calculated by Photonics. This simulation stage is called *hit construction* where the number of photons propagating from the ice through the DOM sphere and onto the PMT are determined. The released photo-electrons and PMT output pulse are simulated in the following step, the *PMT simulation*. The *DOM simulation* includes the DOM electronic response, treatment of the PMT output and its digitisation to ATWD and fADC waveforms. The last step is the *trigger simulation* where the IceCube trigger conditions are applied in order to construct IceCube events. Events which do not pass the trigger conditions are rejected.

### 4.1.5 Simulated data samples

If simulation is done according to true flux parameters then the live time of a simulation event sample is the total number of simulated events over the true event rate. Most of the simulated events used in this analysis, however, were simulated in a biased way in order to favour the simulation of HE events. In the case of biased simulation an effective live time for each energy decade (or smaller intervals) in the event sample can be calculated in a similar fashion to the non-biased event simulation. It is important to have enough simulated events in the interesting energy region in order to reduce the statistical uncertainty of the signal selection methods and expected passing rates. The live time of the experimental data used in this analysis for signal search is 315.34 days. The live time of the signal and background MC simulated samples is in the order of hundreds of years for the highest energies and about a year live time at  $\approx 3 \times 10^6 \text{ GeV}$ .

## 4.2 Event reconstruction

Event reconstruction in IceCube aims to estimate the physical quantities of the recorded event: type of the detected particle or particles, their direction, location and energy. Events observed by the detector can be generally separated to track-like events and cascade-like events depending on the distribution of photon hits in the detector. Different reconstruction algorithms are used depending on the event type hypothesis. In this analysis only track reconstruction methods are used. Atmospheric muons (and muon bundles) are then rejected based on reconstructed variables.

### 4.2.1 Waveform processing

The event reconstruction methods use information extracted from the waveform digitisers in the form of *pulses*. Specifically in IC40 and in this analysis only the output of the ATWD digitiser was used for pulse extraction and event reconstruction.

A recorded event has a set of digitised waveforms for each DOM that has recorded a signal in the event. Each DOM has three ATWD digitised waveforms are obtained by using a different gain on the recorded PMT signal. The software module *DOMcalibrator* is applied on the digitised waveforms in order to calibrate them taking into account the work gain specific for each DOM [81]. *DOMcalibrator* performs a baseline subtraction, corrects for waveform tail droop, determines waveform start time and digitiser clock speed, and combines the three ATWD channels into a single waveform. The calibrated waveform is then passed to the *FeatureExtractor* module for pulse extraction [82]. A pulse is a waveform feature defined by a pulse starting time (leading edge), a pulse width and amplitude, and pulse extraction assumes a typical shape of a single photoelectron pulse. For the IceCube 40 strings data, the *FeatureExtractor* was used in a configuration which extracts a single pulse per waveform. The pulse starting time is given by estimating the leading edge time (or, arrival of first photon) of the first found peak above threshold. The pulse amplitude is given by the charge sum of all waveform bins above threshold and is measured in terms of photoelectrons (PEs), an average charge that a single photon-induced pulse would contain. As a specific pulse shape is assumed and its normalisation is set by the data whereas the attributed pulse width has no real significance.

### 4.2.2 Likelihood description

Event reconstruction can be described by the need to estimate a set of unknown parameters  $\vec{a}$  by using a collection of measured values  $\vec{x}$ . This is achieved by maximising the likelihood function  $L(\vec{x}|\vec{a})$  (or, in practice minimising  $-\ln L$ ) which for independent components  $x_i$  of  $\vec{x}$  can be written as

$$L(\vec{x}|\vec{a}) = \prod_i p(x_i|\vec{a}). \quad (4.1)$$

Here  $p(x_i|\vec{a})$  is the Probability Density Function (PDF) of measuring an  $x_i$  value given determined values for the set of parameters  $\vec{a}$ . In the IceCube case, regarding an infinitely long muon track along which photons are emitted with the typical Cherenkov angle, the set of parameters to determine includes a track vertex location and time, the track direction and energy at time  $t_0$ :

$$\vec{a} = (\vec{r}_0, t_0, \hat{p}, E_0). \quad (4.2)$$

A scheme of the Cherenkov light front and the different variables is presented in Figure 4.2. As the vertex location can be chosen arbitrarily along the track, the geometrical coordinates

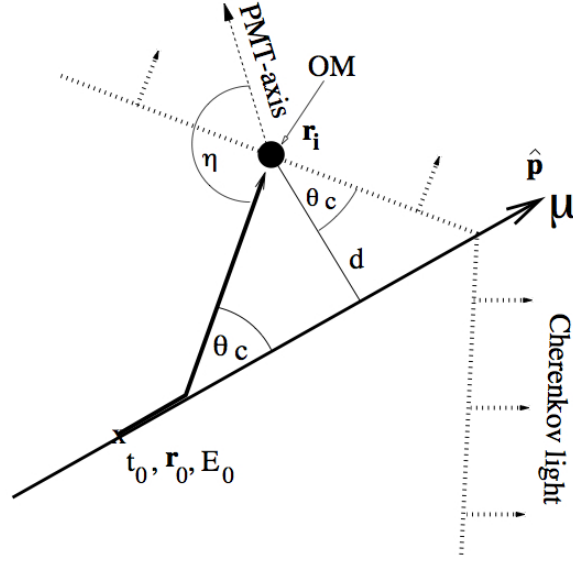


Figure 4.2: Definition of variables of the Cherenkov light front, used in track reconstruction, taken from [83].

contain five degrees of freedom. The energy at the vertex position constitutes the sixth degree of freedom. The geometry and energy of the track can be fitted simultaneously or separately, the latter is most often the case in IceCube. The set of measured values  $\vec{x}$  used for the likelihood minimisation is the set of feature-extracted pulses, each with pulse location, time and amplitude.

In IceCube, the PDF used for parameter estimation needs to describe the probability to measure a certain distribution of photons given a set of values for  $\vec{a}$ . The photon hit distribution on a given DOM is binned in time with  $K$  bins with the number of expected photons for each bin as  $\mu_i$ . The probability of measuring  $n_i$  photons with expectation value  $\mu_i$  is given by Poisson statistics. For a single DOM it is

$$L(\vec{x}|\vec{a}) = \prod_{i=1}^K \frac{e^{-\mu_i}}{n_i!} \mu_i^{n_i}. \quad (4.3)$$

The event's  $\ln(L)$  term is given by summing over  $\ln(L)$  contributions from all active DOMs in the event. The  $-\ln(L)$  term is then minimised with respect to the unknown track parameters. The photon expectation values  $\mu_i$  are determined by a parametrisation of probability of light distribution after propagation through the ice, which is based on previous measurements and presented in the next section.

### Time likelihood

As demonstrated in Figure 4.2 the geometrical photon arrival time at  $i$ th DOM is given by

$$t_{\text{geo},i} = t_0 + \frac{\hat{p} \cdot (\vec{r}_i - \vec{r}_0) + d_i \cdot \tan(\theta_c)}{c_{\text{ice}}} \quad (4.4)$$

The time residual is defined as the difference between the detected photon arrival time and the expected geometrical arrival time from a direct photon (no scattering in the ice) as

$$t_{\text{res},i} \equiv t_{\text{hit},i} - t_{\text{geo},i} \quad (4.5)$$

In an ideal case the distribution  $p(t_{\text{res}}|\vec{a})$  would be a delta function. In reality several effects distort the distribution making it wider and with a typical tail of high positive  $t_{\text{res}}$  values: the limited time resolution of the detector broadens the  $p(t_{\text{res}}|\vec{a})$  distribution, the PMT dark noise adds a flat component to it, photons from radiative energy losses along the muon track (a fluctuating component) create a long tail of high  $t_{\text{res}}$  hits and photon scattering in the ice as well shifts the distribution to higher  $t_{\text{res}}$  values. The first two effects also result in negative  $t_{\text{res}}$  values. Photon scattering in the ice is strongly dependent on the ice purity and the distance  $d$  between the track and the DOM. Scattering is the largest effect on the  $t_{\text{res}}$  distribution compared to the others mentioned above.

A commonly used analytical parametrisation for  $p(t_{\text{res}}|\vec{a})$  in IceCube is the so-called Pandel parametrisation [83]. It is a Gamma distribution based on measurements of laser light propagation taken in the BAIKAL experiment [84] using an isotropic, monochromatic and point-like light source. The Pandel parametrisation for light distribution can be written as

$$p(\xi, \rho, t_{\text{res}}) = \frac{1}{\Gamma(\xi)} \rho^\xi t_{\text{res}}^{\xi-1} e^{-\rho t_{\text{res}}} \quad (4.6)$$

$$\xi \equiv d/\lambda, \quad \rho \equiv 1/\tau + c_{\text{ice}}/\lambda_a. \quad (4.7)$$

The absorption length is given by  $\lambda_a$  while  $\tau$  and  $\lambda$  are functions of  $d$  and the DOM-track geometry, free parameters that are determined empirically [85]. The Pandel function is normalised and can be integrated analytically.

The Pandel parametrisation assumes bulk ice, meaning constant ice properties (scattering and absorption coefficients) all through the medium. The South Pole ice is however layered, with its characteristics changing significantly between different ice depths, as shown by the ice model in section 3.6.1. This is a disadvantage concerning the accuracy of modelling the photon arrival time distribution in IceCube for event reconstruction purposes. In order to incorporate the ice layer structure in the event reconstruction the Photonics (section 4.1.3) photon propagation tables are used. The Photorec software uses the Photonics tables (that are calculated according to the full ice model) to construct normalised numerical PDFs of Cherenkov photon arrival time.

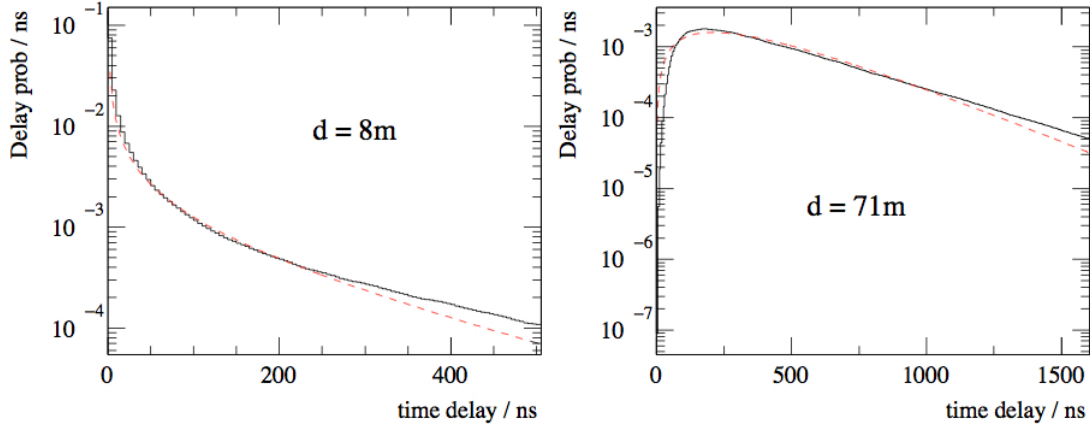


Figure 4.3: Residual time distribution from MC simulation (black) and in comparison the Pandel characterisation (dashed red) at short (left) and long (right) distance from a muon track [83].

#### 4.2.3 Track first guess

The track reconstruction methods based on the full likelihood description require a starting point (a track seed) to start the minimisation process. The track seed is obtained by fast analytic algorithms that do not require a starting point. The linefit algorithm is the first guess method used in this analysis. Linefit assumes a simple geometry which gives an analytical solution and is therefore very fast to obtain. The linefit track result is used by online filters at the South Pole as well as to seed higher level reconstruction algorithms such as SPE and MPE (section 4.2.4).

The linefit algorithm [83] does not use the true geometry of photons emitted in a Cherenkov cone around an advancing particle and neglects photon delay due to scattering in the ice. Instead, Linefit assumes an effective velocity  $\vec{v}$  with which the photons travel in a one-dimensional path through the detector and which is a free parameter of the fit. A DOM photon hit at time  $t_i$  and location  $\vec{r}_i$  is then described by

$$\vec{r}_i = \vec{r}_0 + \vec{v} \cdot t_i \quad (4.8)$$

where  $\vec{r}_0$  signifies the vertex point. A  $\chi^2$  term is then defined and minimised to obtain the solution  $(\vec{v}, \vec{r}_0)$ :

$$\chi^2 = \sum_{i=1}^{N_{\text{pulses}}} (\vec{r}_i - \vec{r}_0 - \vec{v} \cdot t_i)^2 \quad (4.9)$$

The summation is done over the pulses in the event, where  $t_i$  is the pulse's leading edge time and  $\vec{r}_i$  is the DOM position. Derivation of the  $\chi^2$  with respect to the free parameters gives an

analytic solution:

$$\vec{r}_0 = \langle \vec{r}_i \rangle - \vec{v} \langle t_i \rangle \quad (4.10)$$

$$\vec{v} = \frac{\langle \vec{r}_i \cdot t_i \rangle - \langle \vec{r}_i \rangle \langle t_i \rangle}{\langle t_i^2 \rangle - \langle t_i \rangle^2} \quad (4.11)$$

where  $\langle x_i \rangle$  is the average of parameter  $x$  over all pulses. The fitted velocities typically are close to the speed of light for track-like events with a long track and relatively homogenous light emission, and are smaller for cascade-like events.

#### 4.2.4 Muon track reconstruction algorithms

The Single Photo-Electron (SPE) PDF  $p_1$  describes the arrival time of single photons on a specific DOM location [83]. The PDF is obtained from simulation of photon propagation through the ice. For the SPE reconstruction method only the information from the first photon is used and the reconstruction result is robust (in practice the first rise time found in the PMT waveform is used). The exact measurement of photon arrival times other than the first one is limited due to electrical and optical signal response time. The constructed SPE likelihood function that is optimised is

$$\ln(L_{\text{time}}) = \sum_{i=1}^{N_{\text{DOM}}} \ln(p_1(t_{\text{res},i}|\vec{a})) \quad (4.12)$$

The result of the linefit first guess algorithm is used as a seed for the SPE track reconstruction. The result of the SPE is used for running a 32 iteration SPE fit (SPE32).

The first photon arriving at a DOM is usually less scattered than the average single photo-electron. The SPE PDF is modified to account for that. The arrival time distribution for the first of  $N$  photons is calculated by [83]:

$$p_N^1(t_{\text{res}}) = N \cdot p_1(t_{\text{res}}) \cdot \left( \int_{t_{\text{res}}}^{\infty} p_1(t) dt \right)^{(N-1)} = N \cdot p_1(t_{\text{res}}) \cdot (1 - P_1(t_{\text{res}}))^{(N-1)} \quad (4.13)$$

$P_1$  is the integrated distribution of the SPE PDF. The resulting  $p_N^1(t_{\text{res}})$  is called the Multi Photo-Electron (MPE) PDF. Similarly to (4.12), a MPE likelihood parameter is defined and its optimisation is referred to as the MPE reconstruction.  $N$ , the number of photons arriving at the DOM is estimated from the waveform and again the first identified rise time of the waveform is used for the first photon arrival time. The SPE32 reconstruction result is used as a seed for the MPE fit. The MPE reconstruction result improves with the energy of the muon event, the number of DOMs in the event and the event NPE (recorded Number of Photo-Electrons). For very energetic events with high NPE value the first arriving photons are very much direct photons (no scattering) and so they carry the information on the track

location. The MPE reconstruction has on average a smaller error on the fitted track parameters than the SPE reconstruction result. It is also more prone to converge in a local minimum rather in the global one (compared with the SPE fit), which gives rise to a small fraction of events with a mis-reconstructed track geometry.

## 5 GZK neutrino search data analysis

This chapter begins with an overview of the GZK neutrino search with data collected by the IceCube neutrino observatory. Information is given on the searched signal, the type of background events, the used MC simulation and the IceCube data on which the search is performed. The analysis starting filter level & first cuts are described next, with analysis higher level observables introduced in the next chapter.

It is important to note that the analysis was developed by using MC simulated signal and background events and a data burn sample (see section 5.1.4). The analysis technique and all selected cuts were determined based on these samples to avoid any bias. The analysis method has been frozen and approved by the IceCube collaboration prior to looking at the full data sets and obtaining final results.

### 5.1 Analysis overview

#### 5.1.1 The searched signal

This analysis is optimised to search for ultra high energy neutrinos, such as neutrinos predicted by the GZK effect (section 2.2.5) at  $10^8 - 10^9$  GeV energies using the IceCube 40-strings detector (IC40) data run. The predicted GZK neutrino event rates from the different theoretical models are in the order of 1 for the IC40 data run live time. A comparison of several theoretical models considered in this analysis is presented in Figure 5.1. The three neutrino flavours are included in the search, although the developed methods for background rejection (sections 6.2 and 6.3) are based on  $\nu_\mu$  signal events alone.

One of the GZK neutrino models is used as the default model in this analysis, so that the cut optimisation depends on it. This default model is the Seckel-Stanev 2008 pure proton, HiRes-measured energy normalisation model [32], referred to as *SS08 135h*. This model contains a  $10^8 - 10^9$  GeV energy neutrino peak from proton interactions produced with flavour ratio (1 : 2 : 0) and a lower energy  $\bar{\nu}_e$  peak from neutron decays (1 : 0 : 0). Taking into account

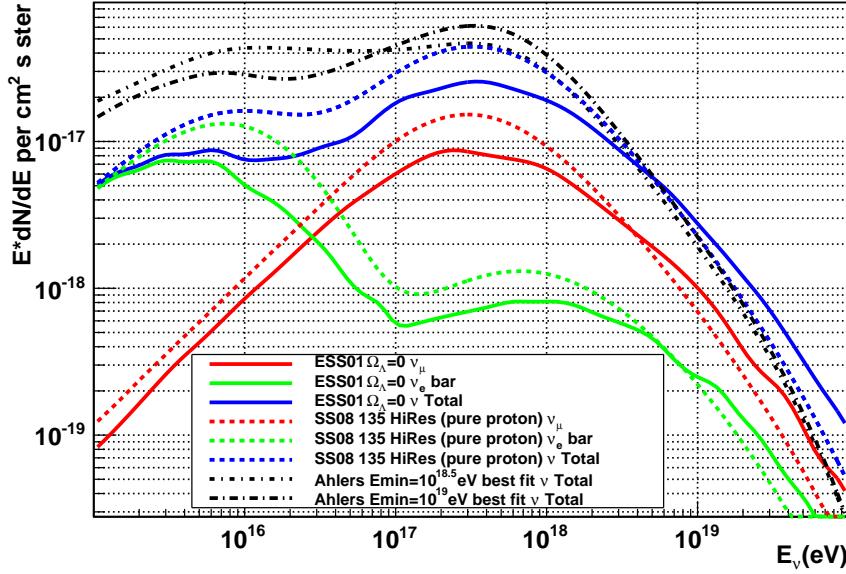


Figure 5.1: The neutrino flux prediction from different GZK theoretical models. The ESS01 [30] and SS08 [32] models both give curves for produced  $\nu_\mu$  and  $\bar{\nu}_e$  which are used for calculating GZK neutrino event rate at IC40 after flavour oscillations over cosmological distances. The Ahlers models (reference [33]) give a prediction for the all-flavour neutrino flux. The predicted neutrino event rates from these models for the full IC40 data sample are in the order of 1.

neutrino flavour oscillation over cosmological distances (see section 2.2.1) the main GZK peak will oscillate to a flavour ratio of (1 : 1 : 1) on earth while the neutron decay peak evolves to (5/9 : 2/9 : 2/9). All noted event rates at IceCube take into account this flavour mixing. In the case that a model prediction is given for the total neutrino flux (such as for the Ahlers models), a mixing to flavour ratio (1 : 1 : 1) is used. In addition event rates for a generic diffuse flux of  $E^{-2}$  energy dependency are reported. While the analysis is optimised for the higher energy GZK neutrino flux, it is also sensitive to the  $E^{-2}$  diffuse flux.

Figure 5.2 shows the resulting  $\nu_e$ ,  $\nu_\mu$  and  $\nu_\tau$  fluxes passing the IC40 detector online filter used as a starting point for this analysis (EHE Filter). Each curve represents  $\nu + \bar{\nu}$  fluxes. The prominent Glashow resonance is seen at the  $\nu_e$  flux. The  $\nu_\mu$  and  $\nu_\tau$  fluxes are quite similar and are substantially higher than the  $\nu_e$  flux thanks to the large muon range.

### 5.1.2 Background events

High energy atmospheric muons (and muon bundles) originating from cosmic-ray showers represent the main background for this neutrino search (see section 2.3.1). Double and triple coincident CR showers represent a much less significant background. This analysis includes atmospheric neutrinos as background and aims to minimise their rate after the final selection

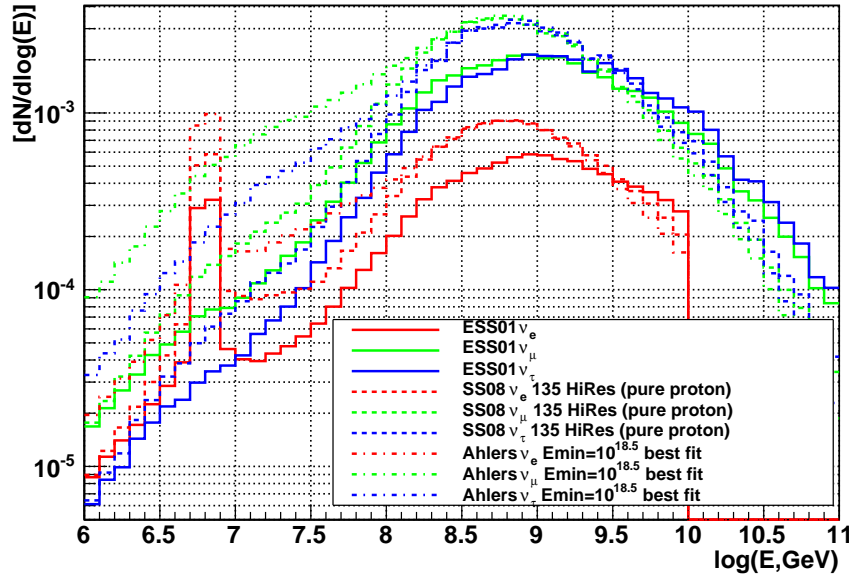


Figure 5.2: GZK neutrino fluxes at IC40 passing the detector online filter (EHEFilter) used for this analysis. Fluxes of the three neutrino flavours ( $\nu + \bar{\nu}$ ) are presented for three theoretical models. Rates are scaled to the IC40 data burn sample live time of 33.8 days.

in order to better separate surviving UHE neutrinos from atmospheric ones. The default atmospheric neutrino models used are Honda 2006 [38] for the conventional component and Enberg-Sarcevic [36] for the prompt flux (see sections 2.3.2 and 2.3.3).

### 5.1.3 Analysis structure

Previous GZK neutrino searches in IceCube perform a final event selection based on the Number of Photo-Electrons (NPE) registered in the event and the first-guess track zenith angle [86]. The approach of this work is to use event topology observables that are based on higher level reconstruction and that have a signal-background separation power to increase background rejection. The sensitivity of the neutrino search to detect a neutrino signal is represented by the neutrino effective area. This parameter represents the equivalent area for which all neutrinos reaching the detector would be recorded and pass the analysis event selection. The effective area is dependent on the neutrino energy, incoming zenith angle and flavour, and it enfold the detector physical size and detection efficiencies. If the approach taken by this analysis is successful, then the NPE threshold cut at the analysis final level would be set to lower values, then the neutrino effective area would increase for this analysis compared to previous ones. The structure of the analysis is as follows:

- Analysis level 0 : the IC40 online EHE Filter event selection.

- Analysis level 1 : an energy cut (size of the observed event) to reduce background events efficiently. Lower event rates make it feasible to calculate higher level observables.
- Analysis level 2 : rejection of atmospheric muons by using the IceTop surface array in the appropriate angular range.
- Analysis level 3 (final cut selection) : simultaneous optimisation of cuts on event-topology observables and registered event NPE as a function of the zenith angle of reconstructed tracks.

### 5.1.4 Data sample and simulated events

Information about the IceCube MC signal and background event simulation for the in-ice detector used for this analysis are summarised in Table 5.1. Specifically for the IceTop veto study described in section 6.1, different simulation files including detector simulation of the IceTop and the in-ice IceCube detectors were used for which the information is summarised in Table 5.2.

The data used for this analysis are events collected by the IceCube detector in its 40-strings configuration taken between April 2008 and May 2009. Only data runs where the in-ice part of the detector as well as the IceTop part of the detector were functioning well are considered. All runs tagged as "good" runs and with a run number ending with xx0 constitute the burn sample for this analysis - a set of data used for comparisons with MC simulation and for construction of the analysis which is later discarded. The live time of the data burn sample is 33.86 days. The live time of the set of runs used for the GZK neutrino search is then 315.34 days (the burn sample runs are excluded).

Data and MC simulated events have gone through the same filtering and reconstruction chain. The analysis development has been done while continuously checking good data description by MC simulated events.

## 5.1. Analysis overview

Generator	Type	Spectrum shape	$N_{\text{files}}$	$N_{\text{primaries}}/\text{file}$	Used for
CORSIKA	single proton (H)	$E^{-2}$	600	$2 \times 10^6$	analysis
CORSIKA	single iron (Fe)	$E^{-2}$	600	$2 \times 10^6$	analysis
CORSIKA	single poly-gonato	$\Delta = -1$	1000	$4 \times 10^5$	MC-data comparison
CORSIKA	double coincident poly-gonato	unweighted	1000	$10^7$	analysis
CORSIKA	double coincident poly-gonato	$\Delta = -0.5$	7000	$2 \times 10^6$	analysis
CORSIKA	triple coincident poly-gonato	unweighted	1000	$10^7$	analysis
NuGen	$\nu_{\mu}$	$E^{-1}$	1000	$5 \times 10^3$	analysis
NuGen	UHE $\nu_{\mu}$	$E^{-1}$	100	$1 \times 10^3$	analysis
NuGen	$\nu_e$	$E^{-1}$	1000	$5 \times 10^3$	analysis
NuGen	$\nu_{\tau}$	$E^{-1}$	1000	$5 \times 10^3$	analysis
NuGen	UHE $\nu_{\tau}$	$E^{-1}$	100	$1 \times 10^3$	analysis

Table 5.1: MC Simulated events used for this analysis (in-ice detector simulation). All simulation files use the AHA ice model unless mentioned otherwise. The 2-component model simulation files have a total of 2M single proton showers and 2M single iron showers. The CORSIKA simulation  $\Delta$  parameter gives the index of reduction of the spectral slope of simulated files with comparison to the poly-gonato model. The normal NuGen datasets neutrino energy range is  $10^1 - 10^{10}$  GeV while the energy range in the UHE sets is  $10^9 - 10^{11}$  GeV. The UHE dedicated sets are needed in order to include events from the high energy tail of the GZK peak.

Generator	Primary type	Spectrum shape	$N_{\text{showers}}$	Energy range
SIBYLL	H	$E^{-1}$	$3.6 \times 10^6$	$10^4 - 10^8$ GeV
SIBYLL	He	$E^{-1}$	$3.3 \times 10^6$	$10^4 - 5 \times 10^7$ GeV
SIBYLL	O	$E^{-1}$	$3.3 \times 10^6$	$10^4 - 5 \times 10^7$ GeV
SIBYLL	Si	$E^{-1}$	$3.3 \times 10^6$	$10^4 - 5 \times 10^7$ GeV
SIBYLL	Fe	$E^{-1}$	$3.6 \times 10^6$	$10^4 - 10^8$ GeV

Table 5.2: IC40 IceTop and in-ice detector coincident simulation files used for the IceTop veto study. All simulation files use the AHA ice model.

## 5.2 Analysis level 0 (EHE Filter)

The data sample starting point for this analysis is the IC40 online filter called *EHE Filter* which is designed to retain very bright events in the in-ice detector corresponding to high energy particles. The analysis level 0 (EHE Filter) uses a single selection condition:

$$\log_{10}(\text{NPE}_{\text{portia}}) > 2.8 \quad . \quad (5.1)$$

The observable NPE refers to the total Number of Photo-Electrons collected in an event by the IceCube DOMs (see section 4.2.1). The NPE value used in the EHE Filter condition is obtained by the *portia* waveform processing algorithm. In general *portia* is very similar to the *Feature Extractor* algorithm described in 4.2.1, but fewer waveform corrections due to detector hardware effects are performed in *portia*. However during the IC40 data taking *portia* used ATWD and FADC pulses for the calculation of NPE while *Feature Extractor* used solely ATWD pluses. *Feature extracted* FADC pulses had to be discarded and were not used for track reconstructions due to a software bug in the online processing. The NPE values used in higher levels of the analysis are obtained by *Feature Extractor* and shall be marked simply as NPE. Distribution of the NPE values at EHE filter level are shown in Figure 5.3. The list of MC simulation and data streams represented by the distribution curves is given in Table 5.4.

Simulation and data events go through an offline processing which consists of track first guess (the linefit algorithm, see section 4.2.3) and several likelihood reconstruction algorithms including SPE 1-iteration, SPE 32-iterations and MPE (see section 4.2.4). The following Table 5.3 gives the analysis level 0 passing rates for the different MC simulation and data burn sample streams. The difference of 30% between data and all-CORSIKA simulation event rates is due to differences at low NPE values of the passing events and it is significantly reduced at higher analysis levels. Full IC40 data rates for different theoretic GZK models (Figure 5.2) are listed in Table 5.4.

## 5.3 Analysis level 1

The aim of the analysis level 1 cut is to efficiently reject background events while retaining signal events and to reduce the data volume significantly. The searched GZK neutrino signal creates very bright events in the detector while the atmospheric muon background rate strongly decreases with energy, therefore the level 1 cut variables are energy related. In addition, the likelihood minimisation MPE track fit is required to converge without problems as the fitted track parameters are used in the higher filter levels.

The event variables used are:

- $\text{NPE}_{FE}$  - The number of collected photo-electrons, obtained by the *Feature Extractor* waveform processing algorithm.

	EHE Filter rate (Hz)
Proton + Fe (2component)	0.785
Double coincident CORSIKA (dcor)	0.123
Triple coincident CORSIKA (tcor)	$7.22 \times 10^{-3}$
CORSIKA total (mc_all)	0.916
Atmospheric $\nu$ (atm_honda_sarcevic)	$2.26 \times 10^{-5}$
GZK $\nu_\mu$ (sig_numu)	$1.79 \times 10^{-8}$
GZK $\nu_e$ (sig_nue)	$4.58 \times 10^{-9}$
GZK $\nu_\tau$ (sig_nutau)	$1.66 \times 10^{-8}$
GZK total (gzk_all)	$3.9 \times 10^{-8}$
$E^{-2}$ total (E2_all)	$5.46 \times 10^{-6}$
Data burn sample (data)	1.32

Table 5.3: Analysis level 0 (EHE filter) event rates for MC simulation and burn sample data. The names of corresponding curves in all following distributions are given in brackets. The default atmospheric neutrino models are Honda 2006 (conventional) and Sarcevic-Enberg (prompt). The default GZK neutrino signal is SS135h. Rates are for  $\nu + \bar{\nu}$ .

GZK neutrino model	EHE Filter rate (315.34 days)
SS08 135h (pure proton)	1.06
ESS01 $\Omega_\Lambda = 0$	0.79
Ahlers $E_{min} = 10^{18}$ eV best fit	0.89
Ahlers $E_{min} = 10^{18.5}$ eV best fit	1.21

Table 5.4: EHE filter GZK model all-flavour event rates for the live time of the IC40 data. Rates are for  $\nu + \bar{\nu}$ .

- NCh - The number of in-ice DOMs with registered signal.
- MPE fit status integer - The return value of the MPE track reconstruction algorithm. Status integer zero means fit status 'OK', the fit has converged without problems.

The analysis level 1 conditions which must be simultaneously satisfied are:

$$\begin{aligned}
 \log_{10}(\text{NPE}_{FE}) &> 3.5 \\
 \text{NCh} &> 100 \\
 \text{MPEFit.StatusI} &= 0
 \end{aligned} \tag{5.2}$$

The level 1 cut rejects more than 99% of the background while retaining 66% of the signal at analysis level 0. The full information of the level 1 simulation and data passing rates is provided in Table 5.5.

Two dimension distributions of  $\cos(\theta)$  vs.  $\log(\text{NPE})$  for the Analysis level 1 data and MC are shown in Figure 5.5. The data burn sample plot (left) can be compared to the middle plot

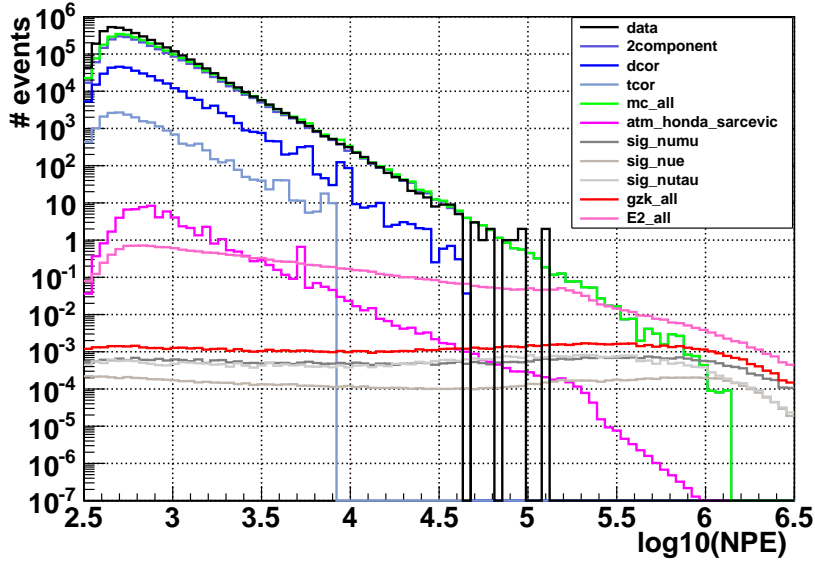


Figure 5.3: Analysis level 0 NPE distribution of MC simulated and burn sample data events. The plotted curves correspond to the MC simulation and data streams given in Table 5.3.

of MC background events which includes the following simulation streams: proton + iron showers, double and triple coincident CORSIKA showers, and neutrino atmospheric flux. The signal plot on the right represent the GZK neutrino flux (three neutrino flavours). It is clear that the background is predominantly downgoing and decreases strongly for larger zenith angles. Mis-reconstructed events and atmospheric neutrinos contribute a flux around and below the horizon. The strongest GZK signal on the other hand is around the horizon and at large NPE values. These distributions and their observed differences between signal and background are the basis for the final cut selection together with additional dedicated parameters presented in the next chapter.

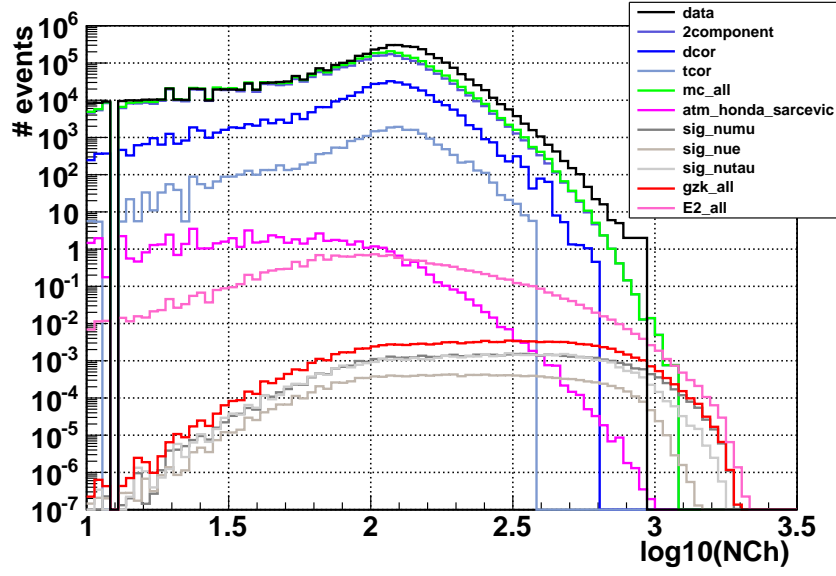


Figure 5.4: Analysis level 0 NCh distribution of MC simulated and burn sample data events. The plotted curves correspond to the MC simulation and data streams given in Table 5.3.

	EHE Filter rate (Hz)	Level 1 rate (Hz)	Level 1 passing fraction (%)
Proton + Fe (2component)	0.785	$5.52 \times 10^{-3}$	0.7
Double coincident CORSIKA (dcor)	0.123	$8.71 \times 10^{-4}$	0.7
Triple coincident CORSIKA (tcor)	$7.22 \times 10^{-3}$	$5.68 \times 10^{-5}$	0.78
CORSIKA total (mc_all)	0.916	$6.45 \times 10^{-3}$	0.7
Atmospheric $\nu$ (atm_honda_sarcevic)	$2.26 \times 10^{-5}$	$1.66 \times 10^{-7}$	0.76
GZK $\nu_\mu$ (sig_numu)	$1.79 \times 10^{-8}$	$1.18 \times 10^{-8}$	65.9
GZK $\nu_e$ (sig_nue)	$4.58 \times 10^{-9}$	$2.72 \times 10^{-9}$	59.4
GZK $\nu_\tau$ (sig_nutau)	$1.66 \times 10^{-8}$	$1.13 \times 10^{-8}$	68.0
GZK total (gzk_all)	$3.9 \times 10^{-8}$	$2.58 \times 10^{-8}$	66.05
E <sup>-2</sup> total (E2_all)	$5.46 \times 10^{-6}$	$1.4 \times 10^{-6}$	25.6
Data burn sample (data)	1.32	$6.32 \times 10^{-3}$	0.47

Table 5.5: Analysis level 1 event rates for MC simulation and burn sample data. The default atmospheric neutrino models are Honda 2006 (conventional) and Sarcevic-Enberg (prompt). The default GZK neutrino signal is SS135h. Rates are for  $\nu + \bar{\nu}$ .

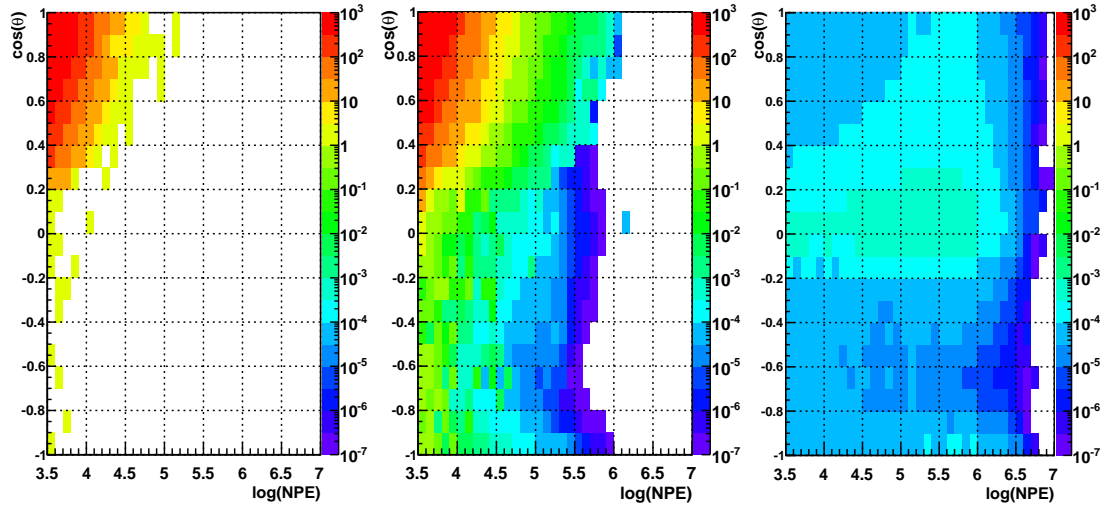


Figure 5.5: Analysis level 1  $\cos(\theta)$  vs.  $\log(\text{NPE})$  distribution for data burn sample events (left), MC simulated background (middle) and MC simulated signal (right). Simulation distributions are normalised to the data burn sample live time of 33.8 days. The colour scale represents the event rate in each  $(\cos(\theta), \log(\text{NPE}))$  bin.

## 6 Atmospheric muon bundles rejection methods

As described in section 2.3.1 the main background of this EHE neutrino search consists of muon bundles from Extensive Air Showers (EAS). Several methods were developed for the separation of energetic muon bundles events from neutrino events and are used in this analysis. The development study was performed using  $\nu_\mu$  signal exclusively, and the resulting methods show signal-background separation power for the three neutrino flavours.

A muon bundle created in EAS may have thousands of muons that reach the IceCube detector at a depth of 1500 m below the surface. Most of the muons are concentrated in a dense core, but some may have relatively high transverse momenta  $p_t$  and are therefore separated from the core of the bundle at the depth of IceCube by a distance  $\propto p_t/E_\mu$ . Multiple scattering and deflection due to the earth's magnetic field can increase the separation for near-horizontal events [87]. Observing the separation of single muons within the bundle core is not possible in IceCube as the photon scattering length in ice is too short and the detector's string spacing is too large for this purpose. However, differences in the light distribution around the bundle core compared to that around a single muon can be used to distinguish the two event classes.

Section 6.1 presents a study of the performance of the IceTop surface array for vetoing high energy muon bundles. Section 6.2 describes how early photon hit times due to muons separated from the bundle core are used for rejecting these events. Finally in section 6.3 the perpendicular light distribution around a fitted track gives additional separation power between muon bundles and neutrino-induced muon events.

### 6.1 Atmospheric shower veto using IceTop

The IceTop surface array uses the same Digital Optical Modules (DOMs) as IceCube's in-ice detector (see section 3.2). When an EAS develops and reaches the surface, charged particles traversing the IceTop tanks generate DOM hits (predominantly muons and electrons). Due to the spreading out of EAS and the high multiplicity within the shower, IceTop has an efficiency

reaching to 100% for detecting close to vertical showers with shower axis in vicinity of the surface array.

Using IceTop hits to veto muon bundle events is very beneficial to the EHE neutrino search as the signal events are in the same phase space as the background: downgoing to horizontal incoming particles. For the IC40 observatory, a CR shower axis with incoming zenith angle up to  $36^\circ$  can be contained in the instrumented volume of both the IceTop array and the in-ice detector. While this constitutes  $1/5$  of the sky's solid angle above the horizon which can be background-cleaned, neutrino-induced leptons in this zenith region arrive at the in-ice detector after propagating only a short distance in the ice. These leptons therefore retain most of the initial energy of the GZK neutrino and their energy flux directly reflects the GZK neutrino spectrum.

In order to use the full capabilities of IC40, the analysis therefore needs to use IceTop hit information in order to tag and reject energetic muon bundles. For this purpose the IceTop detection efficiency was studied for muon bundle events that fulfilled the IC40 in-ice EHE filter condition. The detection efficiency was studied with respect to the incoming CR particle type, energy and topology: zenith angle and its impact parameter to IceTop's centre.

This rejection method is pure in the sense that GZK signal events do not have accompanying IceTop hits except for noise hits, so no signal should be lost when applying the veto. The following section discusses how accompanying IceTop hits due to noise are minimised and why signal loss due to them can be neglected.

Each IceTop tank is calibrated separately in order to determine the charge threshold to be set for its DOM to trigger. The recorded charge by a muon traversing an IceTop tank strongly depends on the length of track in the ice. For a vertical muon this corresponds to the height of the tank ( $\sim 1\text{m}$  ice depth). The charge threshold is then given in units of Vertical Equivalent Muons (VEM) which corresponds to  $\sim 250$  created photoelectrons for an high gain DOM. In IC40 the high gain DOM trigger threshold was in the range  $0.1\text{-}0.2$  VEM (corresponds to  $25\text{-}50$  photoelectrons) which constitutes a high enough threshold to reduces noise hits substantially. Secondly, during the IC40 data taking the IceTop array was working in Hard Local Coincidence (HLC) mode, requiring both tanks of an IceTop station to record hits within a time window of  $1\mu\text{s}$  in order for the waveforms to be kept. IceTop HLC hits (two or more) are saved when within an in-ice event time window. The HLC therefore rejects isolated noise hits. It is noted that small air showers which are detected by a single IceTop tank do not pass the HLC condition and waveforms are not kept. This limits the veto efficiency on low energy showers. The 59-stations IceTop detector started working on a Soft Local Coincident (SLC) data taking mode in June 2009. The SLC mode is similar to HLC with the addition that waveform information from isolated tank hits is saved (time and charge stamps). Therefore, in future analyses using newer IceCube data, the IceTop veto is expected to yield an improved veto capability on low energy showers.

Lastly, the chance that IceTop records at least 2 HLC hits from a real atmospheric muon event

in coincidence with a GZK neutrino event (during the event time window of  $\sim 10\mu\text{s}$ ) was statistically calculated and shown to be very small and is therefore neglected in this analysis.

### 6.1.1 Data and simulated events

The MC simulation used for this study is a dedicated simulation sample of CR showers including detector simulation of both the IceTop surface array and the in-ice detector DOMs. Simulation includes showers from five nuclei types: H, He, O, Si and Fe, for incoming particles with a zenith angle in the range of  $[0, 65]^\circ$  and energy in the range  $10^4 - 5 \cdot 10^7$  GeV (Table 5.2). The SIBYLL hadronic interaction model [75] is used and simulation is done according to an  $E^{-1}$  spectrum. For this study the events are then weighted to represent the CR flux with equal contribution from each nucleus type, which is an approximative representation of it. The data used for this study is the data burn sample as described in 5.1.4. There is no IceTop and in-ice detector coincident simulation for double and triple CORSIKA showers and the veto efficiency is not studied for these type of events.

### 6.1.2 Veto efficiency dependencies

We define the IceTop veto efficiency for a sample of background simulated events as the number of events that have two or more IceTop HLC triggers (one station or more) within the in-ice event time window over all background simulated events. The veto efficiency is studied for subsamples of the MC simulated events with respect to CR particle type, initial energy, zenith angle & event topology.

Several new parameters are defined here in order to describe the topology of the event in the detector. The Impact Parameter (IP) to IceTop is defined as the distance between the incoming CR track position on the ice surface to the centre of the IceTop array, calculated in 2D, as presented in Figure 6.1. The IP (dashed purple line) is then used to calculate a containment parameter (ITcontain) defined as the IP value divided by the length of the instrumented IceTop detector pointing in the same direction as the IP and measured from its centre (solid black line), i.e the maximum instrumented radius in the region where the incoming particle track intersects the ground. This yields  $\text{ITcontain} < 1$  for tracks passing through the instrumented array (contained tracks) and  $\text{ITcontain} > 1$  for tracks passing outside of it (non-contained tracks). Similarly the IP to the centre of the in-ice detector is calculated in 3D from the point of closest approach along the CR track. The track's ICcontain parameter with regards to the in-ice detector is defined similarly as the ITcontain variable but is calculated in 3D. Studying the veto efficiency w.r.t. the containment parameters rather than the IPs reduces the effect of the IC40 detector asymmetry between the detector long and short axes on the efficiency distribution. Figure 6.1 shows a scheme of the IceCube observatory, an incoming track, the definitions of both impact parameters and the length of the instrumented detector used for containment parameter calculation.

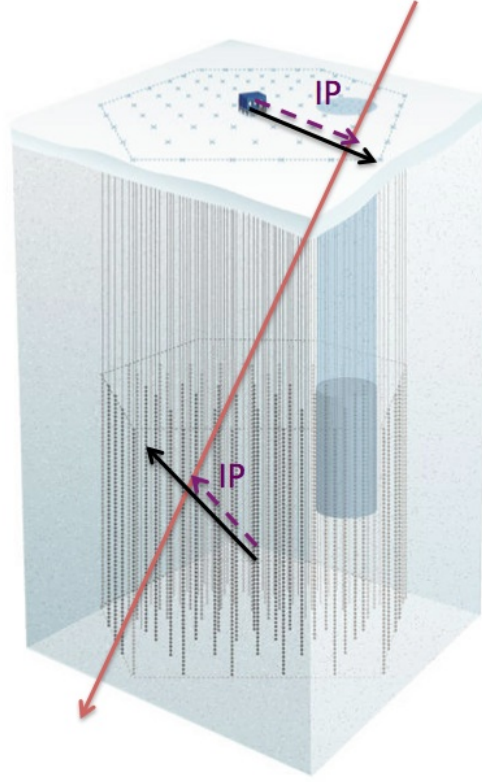


Figure 6.1: The complete IceCube observatory, definitions of the IceTop and in-ice detector Impact Parameters (IPs, dashed purple lines) and illustration of the length of the detector in the same direction as the IP used for the calculation of the containment parameter (solid black lines).

Studied events must fulfil the EHE Filter requirement, selecting events that deposit a large amount of light in the in-ice detector. The veto efficiency for EHE filtered events is then studied using MC true values. Comparing the veto efficiency for different CR primary types showed very small differences. Figure 6.2 shows a comparison of proton and iron nuclei, the two extreme cases. The distributions show that the IceTop veto efficiency is strongly dependent on the initial CR energy and zenith angle (see Figure 6.3). The veto efficiency dependency on the IP w.r.t. the in-ice detector is also demonstrated in these previous plots. A veto condition is then constructed from three parameters characterising the topology of the event: the CR zenith angle and the two IPs, or alternatively ITcontain and ICcontain. The dependency on the azimuth angle is neglected as it is not very important in the IceCube 40-strings detector configuration (section 3.2). Due to the EHE Filter requirement the dependency of the veto on the in-ice IP is the weakest, giving almost constant high efficiency for in-ice contained events and low efficiency for non-contained events. This is clearly demonstrated in Figure 6.4 looking at the veto efficiency on both containment values (MC true values).

The veto efficiency has been studied so far as function of quantities that were provided by the

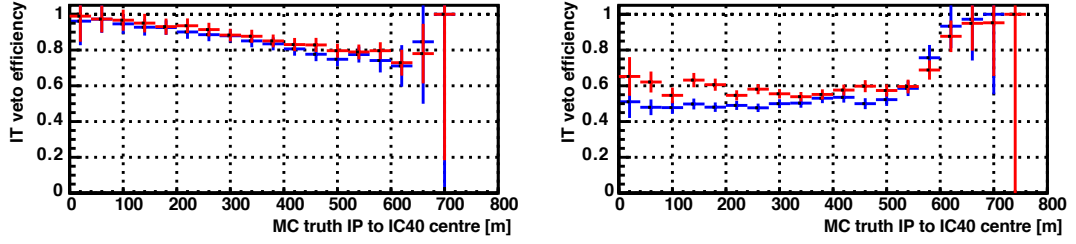


Figure 6.2: The IceTop veto efficiency vs. the IP [m] to the in-ice detector for proton (blue) and iron (red) nuclei. Left plot: events with CR MC true zenith in the range  $[0, 18^\circ]$ , right plot: events with CR MC true zenith in the range  $[18^\circ, 25^\circ]$ . The error bars represent statistical errors.

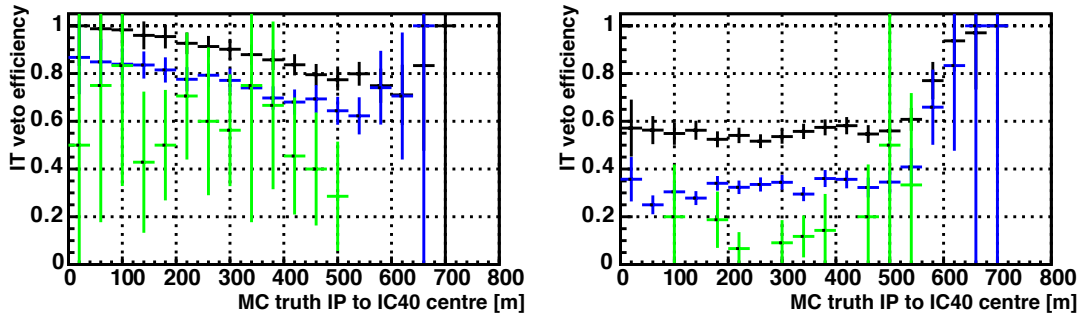


Figure 6.3: The IceTop veto efficiency vs. the IP [m] to the in-ice detector for different energy range curves:  $[0.1, 1]$  PeV (green),  $[1, 10]$  PeV (blue),  $[10, 50]$  PeV (black). Left plot: events with CR MC true zenith in the range  $[0, 18^\circ]$ , right plot: events with CR MC true zenith in the range  $[18^\circ, 25^\circ]$ . The error bars represent statistical errors.

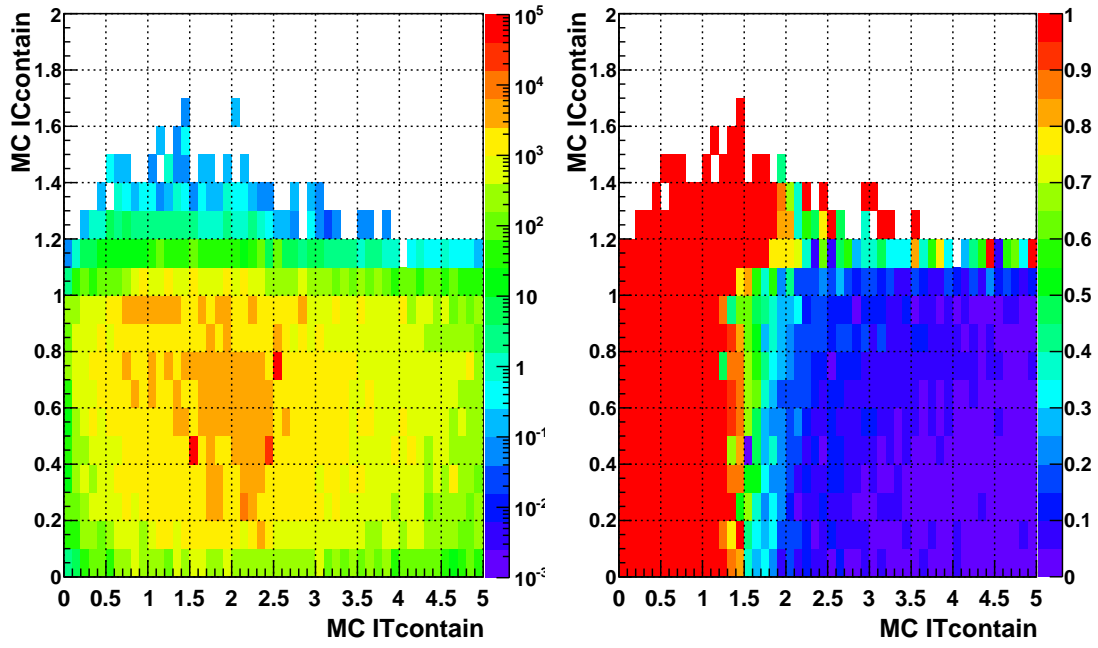


Figure 6.4: IceTop veto efficiency dependency (MC) on true IceTop and in-ice detector containment values. Left plot: distribution of in-ice vs. IceTop containment values for the CR MC dataset (EHE filtered), right plot: IceTop veto efficiency calculated for the same MC events, plotted as a function of ICcontain and ITcontain.

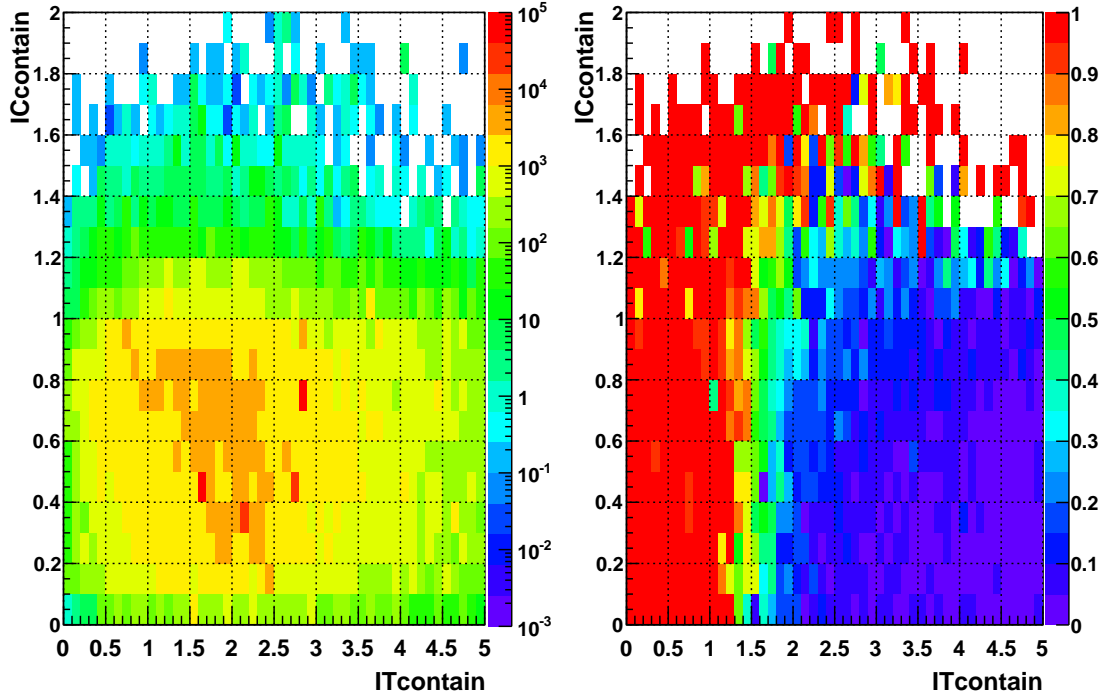


Figure 6.5: IceTop veto efficiency dependency (MC) on MPE reconstructed IceTop and in-ice detector containment values. Left plot: distribution of in-ice vs. IceTop MPE reconstruction containment values for the CR MC dataset (EHE filtered), right plot: IceTop veto efficiency calculated for the same MC events, plotted as a function of MPE ICcontain and ITcontain.

MC truth. In practice, the CR energy is measured by the event NPE value (see section 5.3) and the CR zenith and containment values are calculated w.r.t. the MPE reconstructed track. As seen in Figure 6.5, the efficiency containment map built from the reconstructed track and energy is slightly smeared in comparison to the previous plot.

The veto efficiency has been characterised to be used in this neutrino search by dividing the MC data to three  $\log_{10}(\text{NPE})$  ranges and plotting the veto w.r.t. the MPE track zenith cosine and ITcontain value (the dependency on ICcontain is neglected). This is shown in Figure 6.6. As the veto is applied after analysis level 1 and its  $\log_{10}(\text{NPE}) > 3.5$  condition, only the lower distribution is used in the EHE neutrino search.

### 6.1.3 Data and MC simulation results

A similar veto efficiency map was constructed using burn sample data. The burn sample has reduced statistics at the higher NPE values compared with the MC dataset and higher statistics at the lower NPE values. The obtained veto efficiency distribution from the full burn sample data is shown in Figure 6.7. At the highest NPE range (bottom plot) the high veto

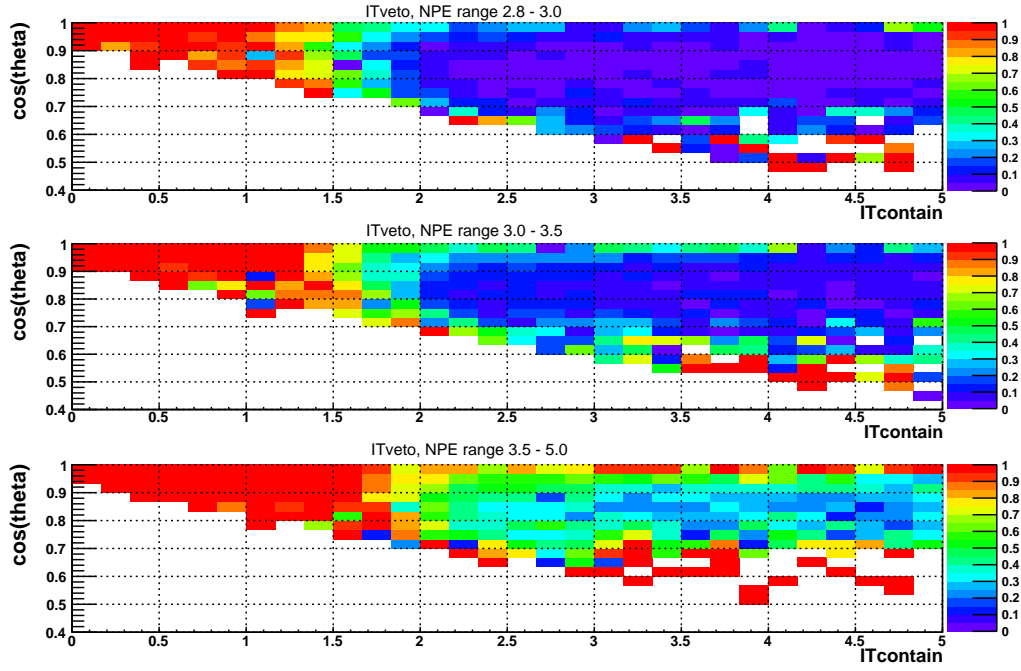


Figure 6.6: IceTop veto efficiency characterisation in reconstructed  $\cos(\theta)$  vs.  $\text{ITcontain}$ . The MC dataset is divided to three  $\log_{10}(\text{NPE})$  ranges:  $[2.8, 3]$  (top),  $[3, 3.5]$  (middle) and  $[>3.5]$  (bottom). The veto efficiency improves with higher NPE events and a high efficiency region ( $>90\%$ ) is found for  $\text{ITcontain} < 1.5$ .

efficiency region appears similarly as in simulation but the burn sample has less entries and the distribution fluctuates more. There are differences between the data and MC simulated events that create slightly different veto capabilities and efficiency for the two samples. The data sample includes single CR showers as well as double and triple coincident showers which constitute about 14% of the event rate at the analysis level 1. There are no double or triple coincident CR shower MC sets available for IceTop veto studies. Data also includes atmospheric neutrino events which are negligible at the event rate but may influence the veto efficiency at certain angles. The MC simulation is only of single MC showers and is limited in angle and energy. In summary, results from data and MC simulation show a similar trend of high veto efficiency for IceTop contained events but the MC describes only a sub sample of the data and results are not expected to be identical. In order to account for these differences in a conservative fashion, the IceTop veto is applied in the analysis in the following way: data events with IceTop signal ( $\geq 2$  HLC hits) are vetoed while on the background MC simulation stream the (MC-obtained) veto efficiency is applied as a reduction weight factor on the single CR shower muon background events (no rejection of double and triple coincident showers). The veto weight factor is applied in the zenith range  $\cos(\theta)=[0.6,1.0]$  and only if the veto efficiency was calculated with  $N \geq 2$  entries in order to disregard bins where the efficiency has an high error due to low statistics. In that way the total background veto passing rate is slightly higher for the MC simulation stream than for the data stream, and the veto representation in MC is conservative.

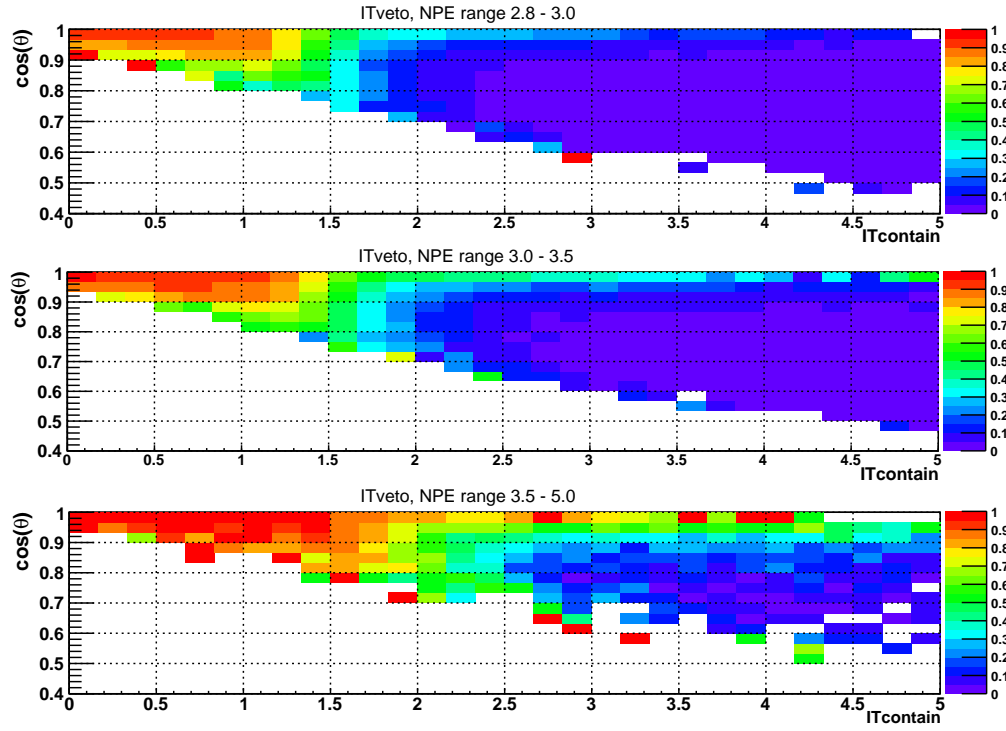


Figure 6.7: The IceTop veto efficiency in the data burn sample in reconstructed  $\cos(\theta)$  vs.  $\text{ITcontain}$  divided to three  $\log_{10}(\text{NPE})$  ranges: [2.8,3] (top), [3.0,3.5] (middle) and [ $>3.5$ ] (bottom).

## 6.2 Early photon hit times

A single muon track hypothesis is used in this analysis for event track reconstruction (the MPE reconstruction algorithm, see section 4.2.4). In the case of large muon bundles originating from energetic CR showers there could be outlying muons which are well separated in space from the main bundle at the IceCube depth. These can generate DOM photon hits which are recorded with negative time residual ( $t_{\text{res}}$  defined in 4.2.2), meaning photons with unphysical arrival time with respect to the fitted single track. The existence of such negative  $t_{\text{res}}$  hits can be used to distinguish these muon bundle events from signal events, neutrino-induced single leptons. This is done by defining a negative  $t_{\text{res}}$  likelihood parameter. The development of a cut parameter out of the  $t_{\text{res}}$  distribution has been done using  $\nu_\mu$  alone as the reference signal.

Figure 6.8 illustrates that muon bundle events tend to have more negative  $t_{\text{res}}$  than the signal events by showing the average number of hits per  $t_{\text{res}}$  range calculated from a large number of events.

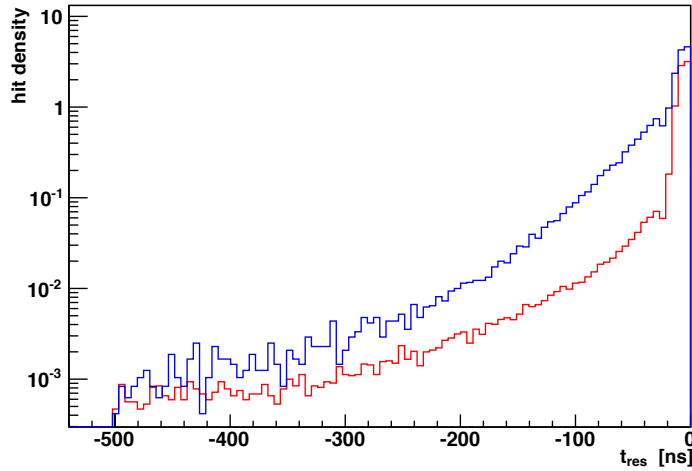


Figure 6.8: The density of negative  $t_{\text{res}}$  hits for muon bundles (blue) from proton and iron CR showers and signal (red) simulated events. The residual times are calculated w.r.t. the MPE fitted track. The events used for calculating the average density are in a range  $\cos(\theta)=[1,0.9]$  and  $\log(\text{NPE})=[4.0,4.5]$ .

### 6.2.1 Early $t_{\text{res}}$ hit density PDFs

The likelihood parameter construction requires a description of typical signal and background events to which an event is compared. This comparison yields a likelihood value for a signal and background hypothesis which is later used as a cut parameter for background rejection. For this purpose a 2D signal  $t_{\text{res}}$  hit density versus  $t_{\text{res}}$  time value distribution is constructed by stacking many MC signal events (and separately for background, muon bundles MC events). This is done in the following way:

- The number of photon hits in the event in the  $t_{\text{res}}$  range  $[-400, 1000]$  ns is calculated by summing over photon hits in that range:  $p_{\text{all}} = \sum_{i=0}^N p_{\text{tres},i}$  with  $p_{\text{tres},i}$  representing the number of photon hits in the  $i$ th bin. A time residual bin width of 10ns is used.
- A logarithm of photon hit density  $\rho_{\text{tres}}$  per  $t_{\text{res}}$  bin is calculated by  $\log(\rho_{\text{tres},i}) = \log(p_{\text{tres},i}/p_{\text{all}})$ . Photon densities are used rather than the number of registered photons as the density is roughly decorrelated from the event NCh (number of active DOMs), an observable that shows some disagreements between data and MC simulation.
- If  $p_{\text{tres},i} > 0$  then the  $\log(\rho_{\text{tres},i})$  value is in the range  $[-3, 0]$ . If  $p_{\text{tres},i} = 0$  then the value of the logarithm is set artificially to  $\log(\rho_{\text{tres},i}) = -4$  to represent minimum density. This is done as  $t_{\text{res}}$  bins with zero entries are important information in the event description and the chosen value is small enough that it is not otherwise obtained in any event in any  $t_{\text{res}}$  bin.
- A 2D histogram of  $\log(\rho_{\text{tres}})$  vs  $t_{\text{res}}$  is filled with information from signal (background) events. The 2D histogram is scaled by  $1/N_{\text{events}}$  giving that for each  $t_{\text{res}}$  bin the distribution of  $\log(\rho_{\text{tres}})$  is normalised to 1. In other words, for each  $t_{\text{res}}$  bin there is a Probability Distribution Function (PDF) of the logarithm of photon hit density for signal (and background) events, a PDF of  $(\log(\rho_{\text{tres}})|t_{\text{res},i})$ .

The EHE-filtered MC simulated events are divided into five  $\log(\text{NPE})$  ranges and five signal and five background 2D PDFs are constructed (four ranges relevant after the analysis level 1 cut). This is done in order to limit the NPE dependency of the constructed parameter, giving PDF of  $(\log(\rho_{\text{tres}})|t_{\text{res},i}, \text{NPE})$ . Examples of the obtained 2D PDFs for the range  $\log(\text{NPE})=[4.0, 4.5]$  for signal and background MC events as well as the corresponding distribution from data burn sample events are presented in Figure 6.9. It is seen that the density of negative  $t_{\text{res}}$  hits is higher in data and background MC compared to signal MC. Data and background MC show very similar behaviour. A difference between signal and background MC in the density distribution at positive  $t_{\text{res}}$  values is observed. This difference is due to the fact that, for a given NPE range, background event tracks pass closer to the IceCube detector centre than signal event tracks, which predominantly pass outside of it (or at its edge). Photons originating from a muon passing well outside of the detector need to propagate (on average) larger distances than for contained events to reach the DOMs. With increasing propagation distance there is less chance for direct photons ( $t_{\text{res}} = 0$ ) and higher probability for larger  $t_{\text{res}}$  values. In addition the accuracy of reconstructing non-contained tracks is lower than that of events passing well within the instrumented detector volume. A poorer estimation of the track parameters (zenith, azimuth, vertex) results in less accurate estimations of  $t_{\text{res}}$  values. From these reasons the signal positive  $t_{\text{res}}$  distribution is less peaked around  $t_{\text{res}} = 0$  and flatter at large values compared to the background distribution.

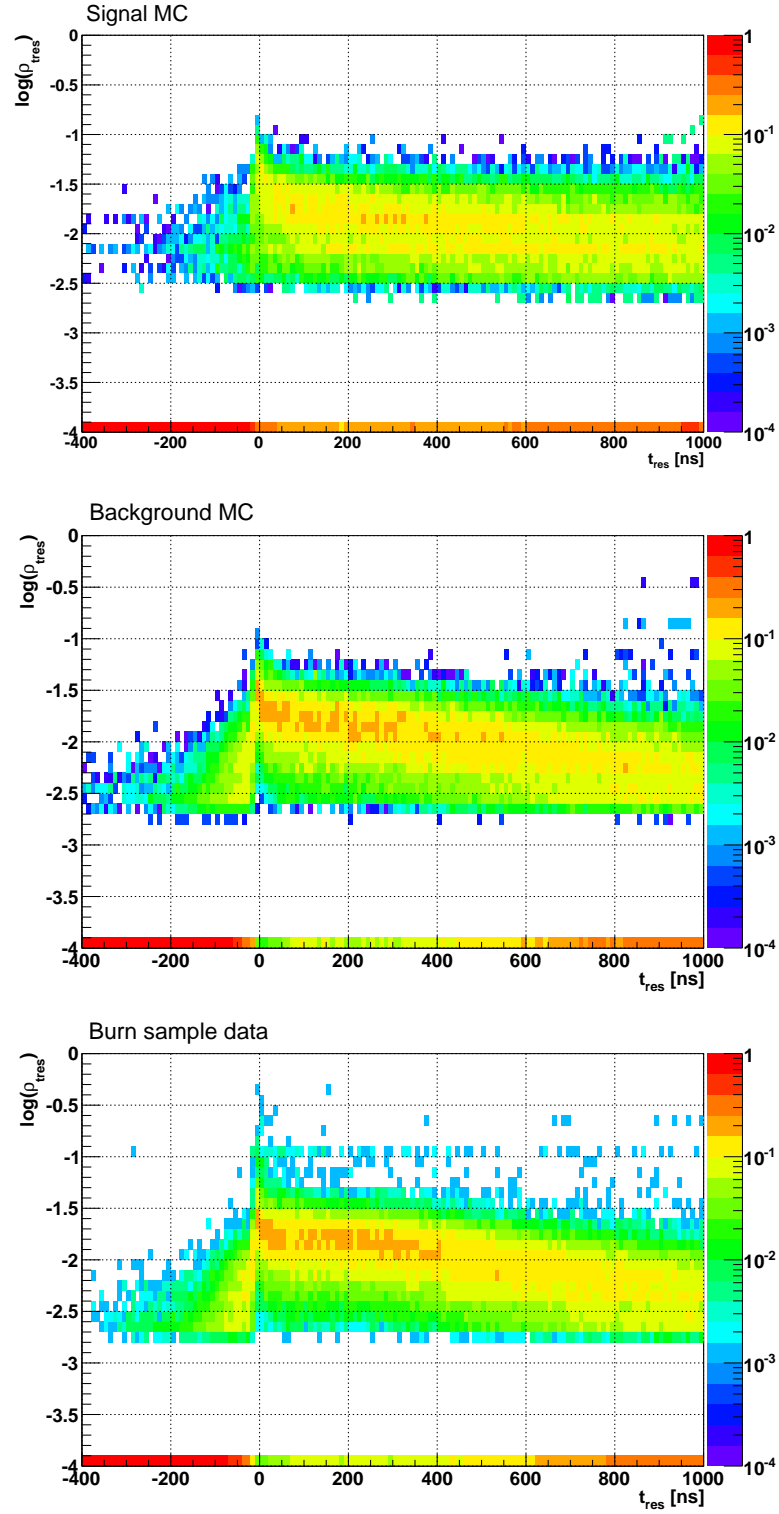


Figure 6.9: The 2D PDFs of negative  $t_{\text{res}}$  photon hit density for signal and background simulation, and the photon hit density distribution for data events. Upper plot:  $\nu_\mu$  signal MC, middle: atmospheric muon background MC, bottom: data burn sample events.

### 6.2.2 Construction of early $t_{\text{res}}$ likelihood parameter

The  $t_{\text{res}}$  hit distribution of a single event is then used to construct a signal-like (background-like) photon hit density likelihood parameter by comparing it to the signal (or background) 2D PDF of  $(\log(\rho_{\text{tres}}) | t_{\text{res},i}, \text{NPE})$ . This is done as following (quantities are defined per event):

- Photon hits with residual time in the range  $[-400, 50]$  ns only are considered.
- The set of photon hit logarithm of densities is calculated:  $\log(\rho_{\text{tres},i} | t_{\text{res},i}, \text{NPE})$ .
- The probabilities corresponding to the set of photon densities are read from the signal (or background) relevant 2D PDF, giving a set  $p_{s,i}(\log(\rho_{\text{tres},i}) | t_{\text{res},i}, \text{NPE})$ . Here s stands for signal, b for background.
- The signal likelihood is the product of signal photon hit density probabilities:  $L_s = \prod p_{s,i}$ , and similarly for background likelihood.
- The ratio of signal-hypothesis likelihood to background-hypothesis likelihood is the eventual parameter that is used to separate signal from background:  
 $\Delta \ln(L_{\text{tres}}) = \ln(L_s) - \ln(L_b) = \ln(L_s/L_b)$ , giving negative values to background-like events and positive values to signal-like events (s stands for signal, b for background).

In the cases where there are no photon hits in the residual time range of  $[-400, 50]$  ns (as may happen for signal events, low percentage of background events, or for badly mis-reconstructed events) then the  $\Delta \ln(L_{\text{tres}})$  parameter is left undefined and it is not used as a cut parameter. In practice even in such case the  $\Delta \ln(L_{\text{tres}})$  can be calculated and the obtained value was shown to be a relatively large positive one, very much "signal" like, as expected. The decision whether to include or exclude such "zero photon hits" in this method is a matter of choice, but the end result is most probably the same. These events are very much signal-like and are kept.

### 6.2.3 Early photon hits $\Delta \ln(L_{\text{tres}})$ parameter distributions

The resulting  $\Delta \ln(L_{\text{tres}})$  parameter distributions for different MC simulation streams and burn sample data at the analysis level 1 are shown in Figure 6.10. The total MC background simulation and burn sample data distributions agree well. The background peaks at negative  $\Delta \ln(L_{\text{tres}})$  values while the GZK signal peaks at positive ones as expected.

In order to better present the separation power between signal and background events, the distributions are divided into  $\log(\text{NPE})$  ranges (four distributions above analysis level 1 cut) and are shown in Figure 6.11 (distributions are normalised to 1). The division of the events into  $\log(\text{NPE})$  bins is relevant as at the analysis final level the  $\Delta \ln(L)$  parameter cut value is determined together with a  $\log(\text{NPE})$  cut. The separation improves slightly with higher NPE.

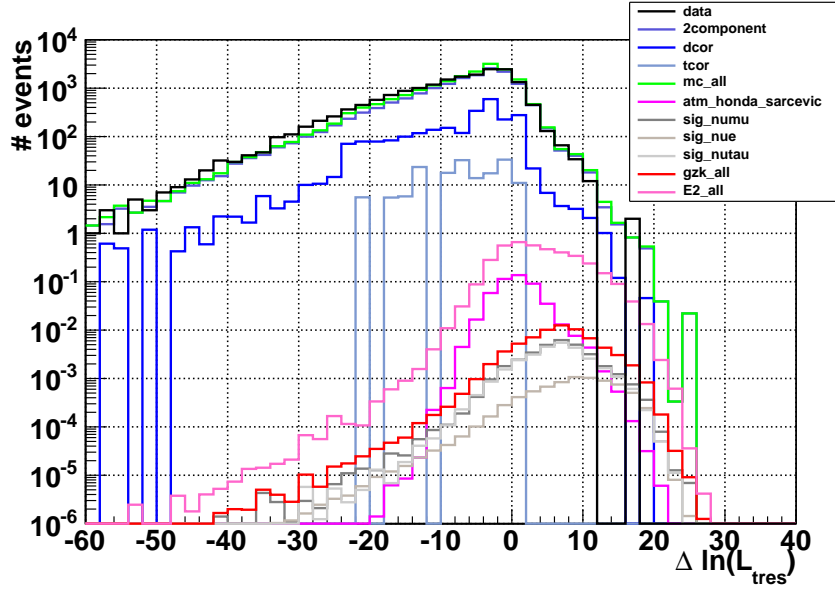


Figure 6.10:  $\Delta \ln(L_{\text{tres}})$  parameter distribution at analysis level 1. Total MC background simulation (green) and burn sample data (black) distributions agree well.

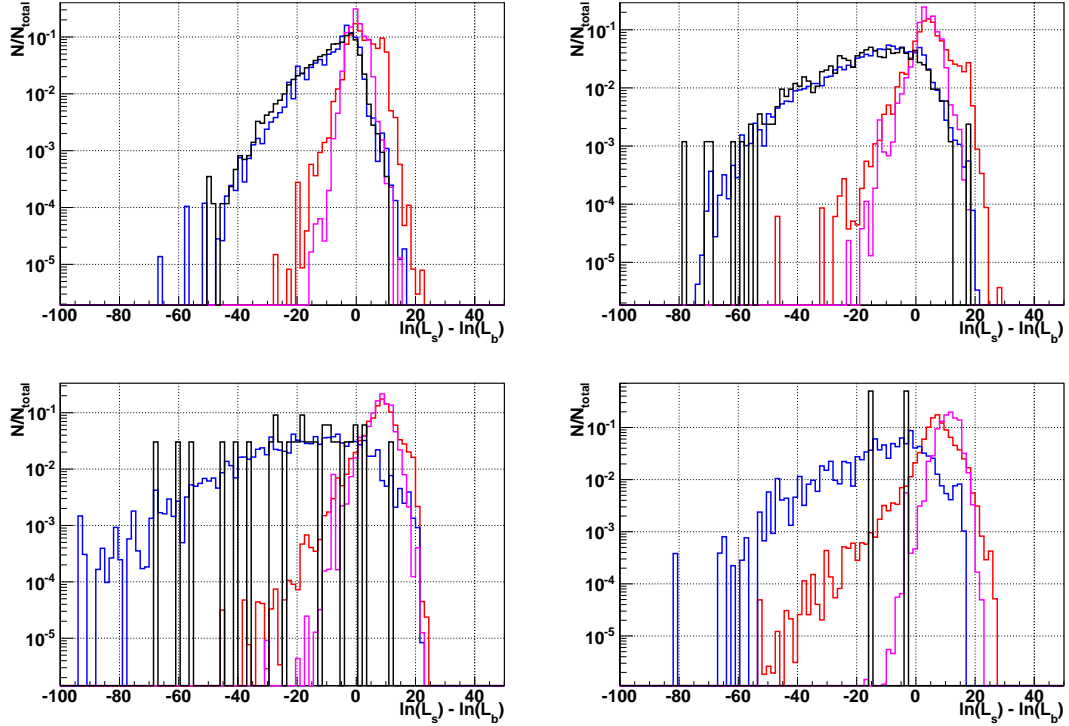


Figure 6.11:  $\Delta \ln(L_{\text{tres}})$  parameter distributions for different  $\log(\text{NPE})$  ranges: top left  $[3.5, 4.0]$ , top right  $[4.0, 4.5]$ , bottom left  $[4.5, 5.0]$ , bottom right  $> 5.0$ . The curves represent GZK neutrino all-flavour (red), atmospheric neutrinos (magenta), CORSIKA atmospheric muon background (blue) and burn sample data (black). The distributions are normalised to 1.

### 6.3 Perpendicular light distribution

As mentioned earlier, the photon scattering length in the ice is too short and the spacing of the IceCube DOMs is too large to facilitate the observation of separate muons within a muon bundle core. However, the emitted light distribution perpendicular and along a muon bundle core may differ from that of a single muon event of the same energy. The radial spread of the muons inside the bundle can be up to  $\sim 50$  m, so the perpendicular light distribution at small distances is flatter around a bundle compared to a single muon track. The amount of detected light at larger distances is higher for a single muon track compared to a bundle. This is because muons in the bundle range out and do not reach the clearest ice at the bottom of the detector and of large stochastic energy losses in the single muon case. In this work we focus on constructing a likelihood parameter describing the difference in falling light densities perpendicular to a muon bundle and a single muon light source.

This development work included as well an attempt to use the change in light yield along the track, but this has not produced a useful parameter. The ice quality (scattering and absorbent coefficients) changes with depth, with the clearest ice found at the bottom of the IceCube detector. This results in a higher photon detection efficiency at the bottom of the detector, an effect which works in contrast to the fading light yield from muon bundles as they traverse the ice and loose energy, making the light fading less visible. One has to precisely account for the ice clarity between points of photon emission and detection, taking into account the zenith angle and location of the reconstructed track, in order to recover the fading of light along the track. It is not clear if it is possible to do this with our current knowledge of ice quality in the detector so that the difference between a muon bundle and a single muon would be visible.

#### 6.3.1 Perpendicular light density parametrisation

The amount of detected light at perpendicular distances from a single muon track is a function of the muon energy, ice properties and the detector noise level due to DOM electronics. Its parameterisation is described in [88] and is given by the so-called  $\mu$ -function:

$$\mu(d, \theta, E) = a(\theta, E) \omega^{-d/d_0} + b_{\text{noise}} \quad (6.1)$$

The relevant variables are  $d$ : DOM-track distance,  $\theta$ : opening angle between the string axis and track,  $E$ : energy of the track and  $d_0 = 1$  m. The parameter  $a$  (in units of NPE) represents the light normalisation and is dependent on the energy of the track in IceCube, the dimensionless parameter  $\omega$  describes the shape of the falling light curve and  $b_{\text{noise}}$  (in units of NPE) gives the expected noise level of the DOMs. The parameters  $a$  and  $\omega$  are both dependent on ice properties which vary with depth [68]. However, it is difficult to resolve the dependency as for each event light is emitted and detected at different ice depths and the dependency is averaged in the fitted parameter values. An example for the detected light distribution around a single muon neutrino event and the fitted  $\mu(d, \theta, E)$  function is given in Figure 6.12.

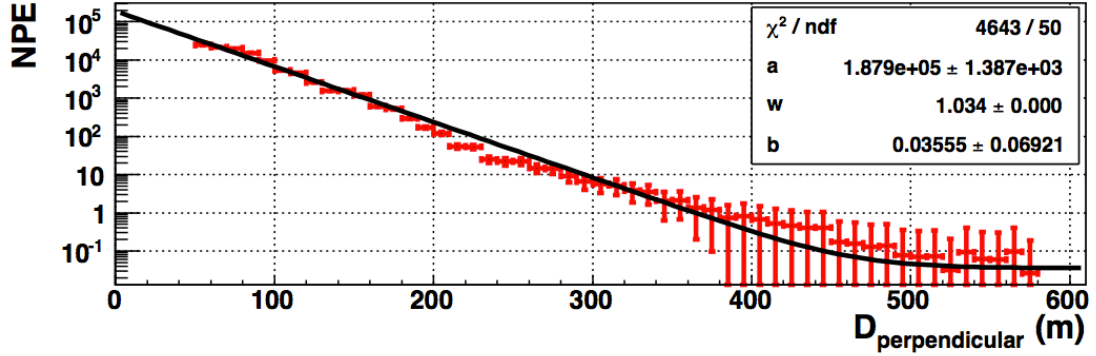


Figure 6.12: Distribution of detected light perpendicular to a simulated neutrino-induced single muon track (red markers) and the fitted  $\mu$ -function (black) for an event with  $\log(\text{NPE})=5$ .

### 6.3.2 Construction of $\mu$ -function likelihood parameter

The difference in perpendicular light distribution between signal and background events in this analysis appears in the  $\mu$ -function fitted values of  $\omega$  and  $a$ . The  $\mu$ -function fit is applied on the set of event-collected pulses (DOM location and *feature extracted* amplitude) and distances calculated with respect to the MPE reconstructed track. In 2-dimensional distributions of fitted  $\log(a)$  vs  $\omega$  values, signal and background events occupy different areas of the phase space. This is shown in Figure 6.13 where signal events typically have a smaller  $\omega$  value and a larger  $\log(a)$  value than background events. The 2D distributions in Figure 6.13 are normalised to 1 so essentially each one constitute a 2D PDF of  $(\omega, \log(a))$  values for its data subset. Such 2D PDFs are constructed from signal and background MC event samples for the four relevant  $\log(\text{NPE})$  ranges above the analysis level 1 cut (same as in section 6.2.1).

These are used to calculate a  $\mu$ -function likelihood parameter in the following manner:

- A given event has a fitted MPE track and fitted  $\mu$ -function to its collected light distribution, resulting in a pair of  $(\omega, \log(a))$  values.
- The probability for a signal (background) event to obtain that set of  $(\omega, \log(a))$  values is read from the relevant signal (background) 2D PDF, represented as  $p_s((\omega, \log(a))|\log(\text{NPE}))$ . If the read probability is smaller than  $10^{-5}$  or the 2D PDF has an empty bin (no information from MC events), a minimum probability of  $p = 10^{-5}$  is set.
- The likelihood for a signal (background) hypothesis is then simply the obtained probability,  $\ln(L_s) = \ln(p_s)$ .
- Similarly as in section 6.2.2 the parameter of the ratio of signal-hypothesis likelihood to background-hypothesis likelihood is defined by  $\Delta \ln(L) = \ln(L_s) - \ln(L_b) = \ln(L_s/L_b)$ , giving negative values to background-like events and positive values to signal-like events.

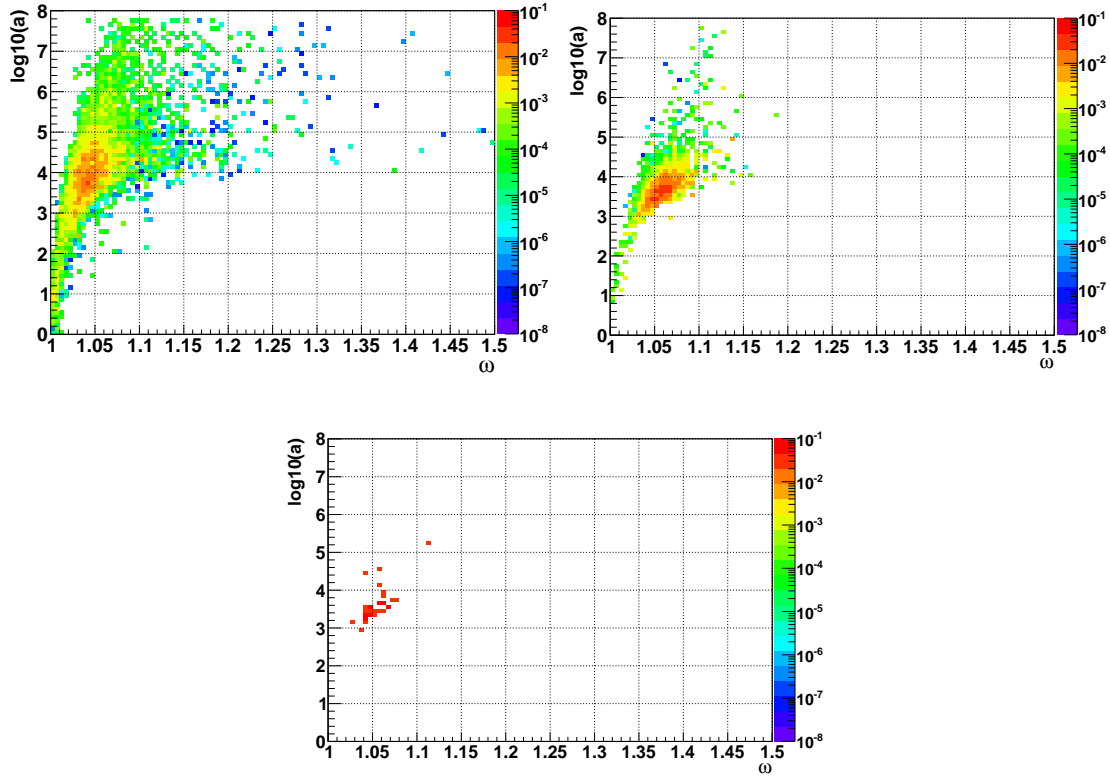


Figure 6.13:  $\mu$ -function fit parameters  $\log(a)$  vs  $\omega$  2D distributions for  $\nu_\mu$  signal MC (top left), atmospheric muon background MC (top right) and data burn sample events (bottom) for events in range  $\log(\text{NPE})=[4.5,5]$ . The distributions are normalised to 1.

In the case that the  $\mu$ -function fit does not converge correctly or the probabilities of an  $(\omega, \log(a))$  pair are minimal ( $p = 10^{-5}$ ) for the signal and background hypotheses, then the parameter  $\Delta \ln(L_{\text{perp}})$  is not defined for this event and cannot be used as a cut parameter. This method is limited by the MC statistics from which the 2D PDFs are constructed.

The distributions of  $\Delta \ln(L_{\text{perp}})$  for all MC streams and data burn sample at analysis level 1 are shown in Figure 6.14. The separation power of this parameter is not as strong as the early photon hit parameter.

#### 6.4 Combined $\Delta \ln(L)$ parameter separation power results.

To maximise the potential of the two parameters they are combined to a single likelihood  $\Delta \ln(L_{\text{com}}) = \Delta \ln(L_{\text{tres}}) + \Delta \ln(L_{\text{perp}})$ . This is a valid approach as adding the two  $\Delta \ln(L)$  terms is the same as multiplying the initial probabilities calculated for the two observables and constructing a single likelihood test

#### 6.4. Combined $\Delta \ln(L)$ parameter separation power results.

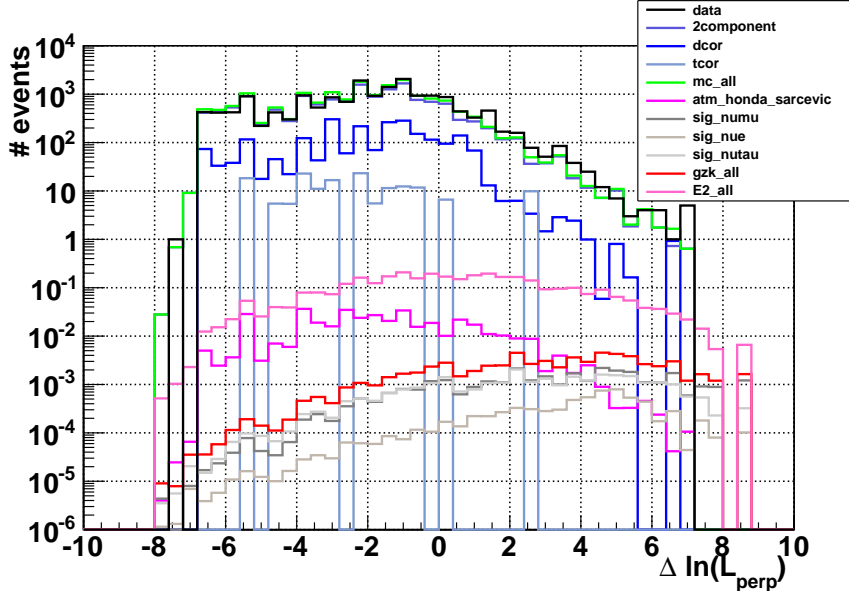


Figure 6.14:  $\mu$ -function fit  $\Delta \ln(L_{\text{perp}})$  distribution at analysis level 1.

$$\begin{aligned}
 \Delta \ln(L_{\text{com}}) &= \ln(L_{s,\text{tres}}) - \ln(L_{b,\text{tres}}) + \ln(L_{s,\text{perp}}) - \ln(L_{b,\text{perp}}) \\
 &= \ln(L_{s,\text{tres}} \cdot L_{s,\text{perp}}) - \ln(L_{b,\text{tres}} \cdot L_{b,\text{perp}}) \\
 &= \ln\left(\prod p_{s,\text{tres},i} \cdot p_{s,\text{perp}}\right) - \ln\left(\prod p_{b,\text{tres},i} \cdot p_{b,\text{perp}}\right).
 \end{aligned} \tag{6.2}$$

The combined likelihood is a stronger cut parameter than using the two separated cuts consecutively. The signal and background separation is increased when multiplying the probabilities, less signal events have a negative  $\Delta \ln(L_{\text{com}})$  value (background-like events) and are lost in comparison to the two separated cuts. The distributions of the combined likelihood parameter per log(NPE) range at the analysis level 1 are given in Figure 6.15.

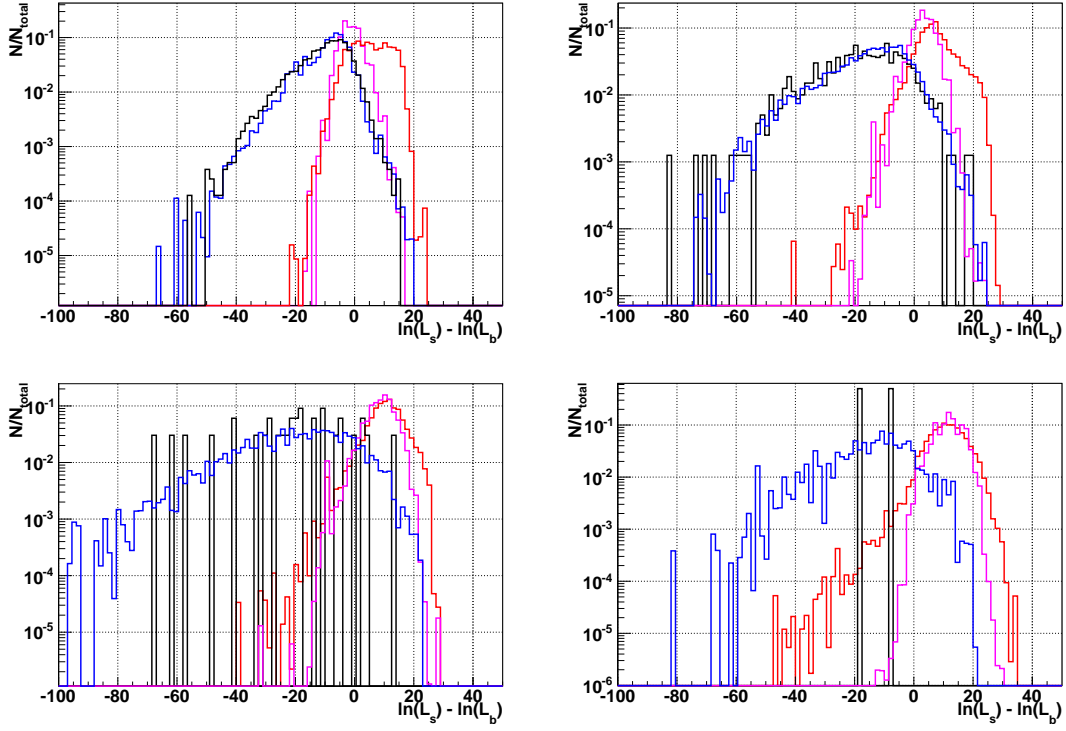


Figure 6.15: Distributions of the combined  $\Delta \ln(L_{\text{com}})$  parameter for different  $\log(\text{NPE})$  ranges: top left  $[3.5, 4.0]$ , top right  $[4.0, 4.5]$ , bottom left  $[4.5, 5.0]$ , bottom right  $> 5.0$ . The curves represent GZK neutrino all-flavour (red), atmospheric neutrinos (magenta), CORSIKA atmospheric muon background (blue) and burn sample data (black). The distributions are normalised to 1.

## 7 Analysis final event selection

The high level cuts of this analysis use the studies described in chapter 6 and the observables developed therein. The final cut selection is performed on the entire event distribution with zenith dependent cut values and has been optimised for signal discovery potential.

### 7.1 Analysis level 2

The IceTop veto on muon bundles described in section 6.1 is applied on the IC40 data passing the Analysis level 1 cuts (section 5.3). This is performed as follows:

- Data burn sample: events with IceTop signal ( $\geq 2$  HLC hits) are rejected (see section 6.1).
- MC simulation single CORSIKA showers (p+Fe): events are re-weighted by  $w = 1 - \epsilon_{\text{veto}}$  where  $\epsilon_{\text{veto}}$  represents the veto efficiency for the relevant ( $\cos(\theta)$ , ITcontain) bin as obtained by the IceTop and in-ice simulation study (Figure 6.6 bottom plot,  $\log(\text{NPE}) > 3.5$ ). The zenith angle and containment parameter are of the reconstructed MPE track. The re-weighting is done in the zenith range  $\cos(\theta) = [0.6, 1.0]$ , corresponding to a reconstructed zenith below  $53^\circ$ . It is only applied if the veto efficiency was calculated with  $N \geq 2$  entries, otherwise,  $w = 1$  (see section 6.1.3).
- MC simulation double and triple coincident CORSIKA showers: all events are kept (the veto efficiency was not studied for these type of events, see section 6.1.1).

Event rates of the data and MC simulation streams at Analysis level 2 (after IceTop veto) are shown in Table 7.1. The background simulation stream event rate (single + double + triple coincident CORSIKA showers) that passes the veto condition is slightly higher than that of the data stream. This means the application of the IceTop veto on the MC is on the conservative (safe) side. The effect of the IceTop veto is seen in the Analysis level 2  $\cos(\theta)$  vs.  $\log(\text{NPE})$  distribution in Figure 7.1 if compared to the same distribution at Analysis level 1 (Figure 5.5).

	Level 1 rate (Hz)	Level 2 rate (Hz)	Level 2 passing fraction (%)
Proton + Fe	$5.52 \times 10^{-3}$	$3.31 \times 10^{-3}$	59.9
Double coincident CORSIKA	$8.71 \times 10^{-4}$	$8.71 \times 10^{-4}$	100
Triple coincident CORSIKA	$5.68 \times 10^{-5}$	$5.68 \times 10^{-5}$	100
CORSIKA total	$6.45 \times 10^{-3}$	$4.24 \times 10^{-3}$	65.7
Atmospheric $\nu$	$1.66 \times 10^{-7}$	$1.66 \times 10^{-7}$	100
GZK $\nu_\mu$	$1.18 \times 10^{-8}$	$1.18 \times 10^{-8}$	100
GZK $\nu_e$	$2.72 \times 10^{-9}$	$2.72 \times 10^{-9}$	100
GZK $\nu_\tau$	$1.13 \times 10^{-8}$	$1.13 \times 10^{-8}$	100
GZK total	$2.58 \times 10^{-8}$	$2.58 \times 10^{-8}$	100
$E^{-2}$ total	$1.4 \times 10^{-6}$	$1.4 \times 10^{-6}$	100
Data burn sample	$6.32 \times 10^{-3}$	$3.92 \times 10^{-3}$	62.1

Table 7.1: Event rates for MC simulation and burn sample data. Default atmospheric neutrino models are Honda 2006 (conventional) and Sarcevic-Enberg (prompt). The default GZK neutrino signal is SS135h. Rates are for  $\nu + \bar{\nu}$ .

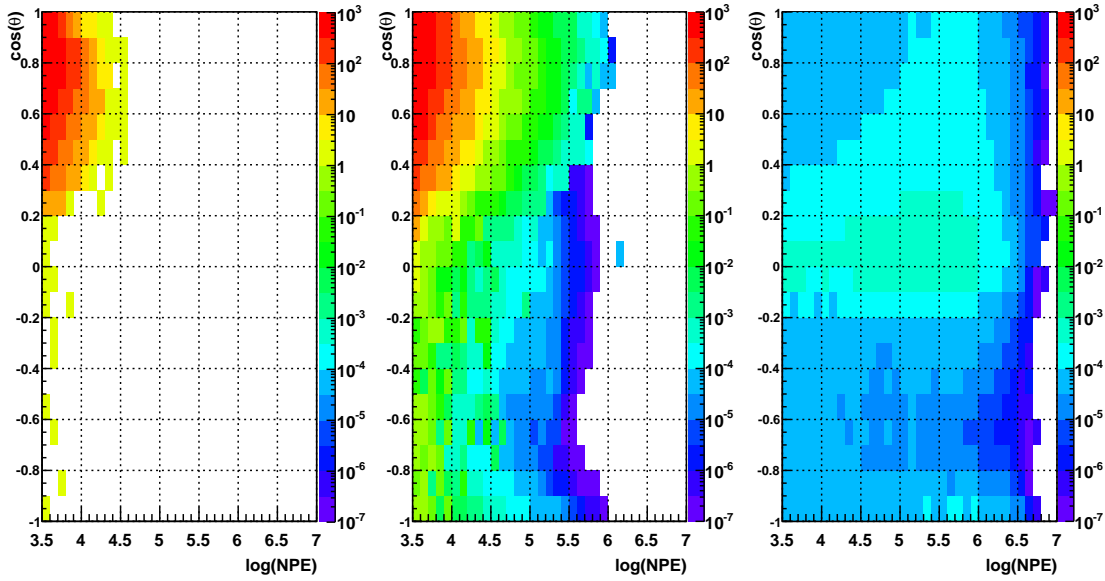


Figure 7.1: Analysis level 2  $\cos(\theta)$  vs.  $\log(\text{NPE})$  distribution for data burn sample events (left), MC simulated background (middle) MC simulated signal (right). Simulation distributions are normalised to the data burn sample live time of 33.8 days. The colour scale represents the event rate in the  $(\cos(\theta), \log(\text{NPE}))$  bin.

## 7.2 Analysis level 3 cut optimisation

At the beginning of this analysis work it was shown that the expected GZK neutrino signal rate for the default theoretical model (*SS08 135h* [32]) is 1.06 events for the IC40 live time (blinded

data) and in the range 0.8-1.2 for other models (see Table 5.4). Given the potential to detect signal events, the approach for determining the final event selection was chosen to optimise the analysis for a discovery by minimising the Model Discovery Potential (MDP) parameter. The MDP parameter is defined similarly to the commonly used Model Rejection Factor (MRF) [89]. Minimising the MRF parameter optimises the power of the analysis to reject theoretical flux models. The MDP parameter on the other hand optimises the analysis to make a discovery if a signal is observed.

### 7.2.1 Model Discovery Potential parameter

In this analysis we perform a counting experiment, meaning eventually counting the events that survive the last cut. In this case a discovery is defined as a high enough observation for which the probability to occur in the background-only hypothesis is very small. If this happens, we claim that (with a defined confidence level) an extra flux above the background has been discovered. We define here the parameters for which these conditions are fulfilled (large enough observation, small enough probability), how the discovery significance is calculated and accordingly the Model Discovery Potential parameter (MDP [90] [91]) for which the last cut selection is optimised.

The probability to count in an experiment  $n_{\text{obs}}$  given a background-only expectation value of  $\mu_b$  is calculated from the Poisson distribution and is referred to as the  $p$ -value:

$$P(\geq n_{\text{obs}}|\mu_b) \quad (7.1)$$

If the  $p$ -value is very small, smaller than  $\alpha = 5.73 \times 10^{-7}$ , then a discovery can be claimed as this particular  $\alpha$  value corresponds to a  $5\sigma$  observation. We define  $n_{\text{crit}}$  as the critical number of observed events needed in order to obtain such  $p$ -value:

$$P(\geq n_{\text{crit}}|\mu_b) < \alpha \quad (7.2)$$

$n_{\text{crit}}$  can be calculated as a function of  $\mu_b$  and for our choice of  $\alpha$ . If a real signal is present with expectation value  $\mu_s$  then the  $n_{\text{crit}}$  value is calculated according to the demanded statistical power of the observation given by  $1 - \beta$ . This relation is written as

$$P(\geq n_{\text{crit}}|\mu_b + \mu_s) = 1 - \beta \quad (7.3)$$

If we choose to demand  $1 - \beta = 0.9$ , meaning given the background and signal expectation values  $n_{\text{obs}} \geq n_{\text{crit}}$  would be obtained at 90% of the cases, then this defines the least detectable signal  $\mu_{\text{lds}}$  as the minimum signal expectation value that fulfils (7.3) for our choice of  $1 - \beta$

$$P(\geq n_{\text{crit}}|\mu_b + \mu_{\text{lds}}) = 0.9 \quad (7.4)$$

This means that a signal of strength  $\mu_{\text{lds}}$  together with background expectation of  $\mu_b$  generate an observed  $n_{\text{obs}}$  giving a  $p$ -value smaller than  $\alpha = 5.73 \times 10^{-7}$  at 90% of the cases. In practice,

given  $\mu_b$  value, relation (7.2) is used to determine  $n_{\text{crit}}$  and afterwards (7.4) is used to determine  $\mu_{lds}$ . The MDP parameter is then defined as  $\text{MDP} = \mu_{lds}/\mu_s$ , so that minimising the MDP means finding the cut location with which the experiment has the best potential to make a discovery.

### 7.2.2 Cut optimisation technique

The parameters used at the Analysis level 3 are the event  $\log(\text{NPE})$ , the calculated combined likelihood parameter  $\Delta \ln(L_{\text{com}})$  (presented in section 6.4) and reconstructed zenith angle,  $\cos(\theta)$ . The distributions of the first two are given in Figure 7.2. Because of the strong zenith dependence of the background and signal distributions (see Figure 7.1) final cuts on  $(\log(\text{NPE}), \Delta \ln(L_{\text{com}}))$  are determined for  $\cos(\theta)$  bins, as presented in the next section.

The selection at the final analysis cut level is performed as follows:

- The entire event distribution shown in Figure 7.1 is divided into 14 bins of  $\cos(\theta)$ , with fine binning of 0.1 bin width at the signal region around the horizon and above it, and wider bins in the upgoing region.
- For each  $\cos(\theta)$  bin a 2D distribution of  $\Delta \ln(L_{\text{com}})$  vs  $\log(\text{NPE})$  is plotted. This is done separately for CORSIKA background events (proton + iron, double and triple coincident showers), atmospheric neutrino background and GZK neutrino signal. An example for these 2D distributions is given in Figure 7.3 for the zenith bin number 10 ( $\cos(\theta)=[0.1,0.0]$ ). Events for which the  $\Delta \ln(L_{\text{com}})$  is undefined (see sections 6.2.2 and 6.3.2) are placed in the y-axis overflow bins and are kept for the next steps. All zenith bin plots are found in the appendix, Figures A.1 to A.3.
- The 2D distributions are used to calculate complement cumulative distributions w.r.t. the two parameters. Examples of the resulting plots are shown in Figure 7.4 for zenith bin 10. The complement cumulative distributions then provide signal and background expectation rates for each  $(\log(\text{NPE}), \Delta \ln(L_{\text{com}}))$  cut value. All zenith bin plots are found in Figures A.4 to A.7.
- Signal and background (CORSIKA + atmospheric neutrinos) expectation values for each  $(\log(\text{NPE}), \Delta \ln(L_{\text{com}}))$  cut values are read from the complement cumulative distributions and the MDP parameter is calculated for that cut selection. This is done repeatedly by scanning over the  $\log(\text{NPE})$  and  $\Delta \ln(L_{\text{com}})$  ranges, thus creating a 2D MDP map for that  $\cos(\theta)$  bin. The MDP parameter is not calculated if  $\mu_s = 0$  or  $\mu_b > 5$ , a range which is not interesting for this work. An example of the obtained MDP map for zenith bin 10 is given in Figure 7.5 and all zenith bin plots are found in Figure A.7.

The 2D MDP map for a  $\cos(\theta)$  bin illustrates the MDP distribution and minimum position for that bin, but finding the local MDP minimum for each bin and setting the  $(\log(\text{NPE}),$

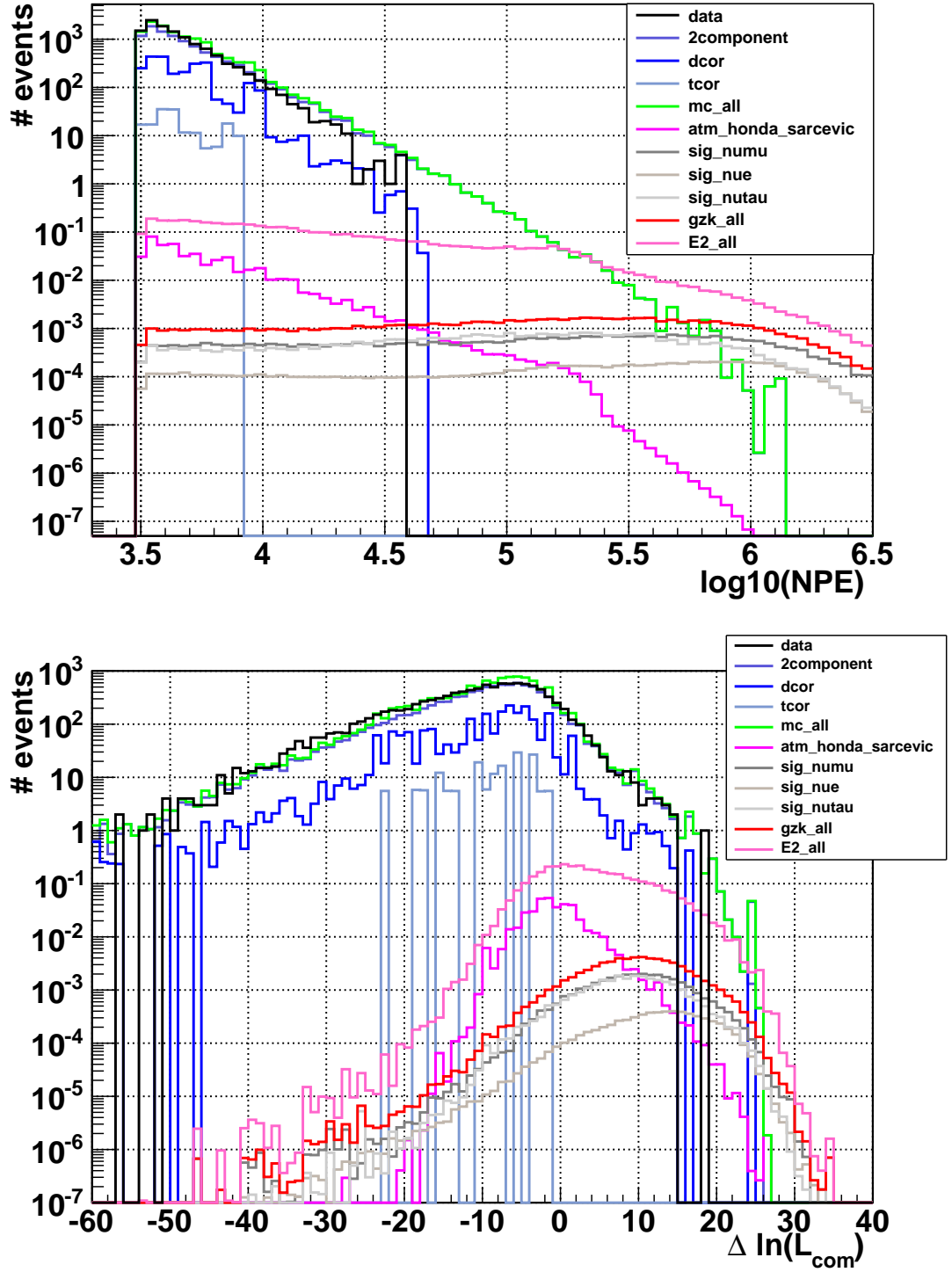


Figure 7.2: Distributions of  $\log(\text{NPE})$  (top) and combined likelihood parameter (bottom) at Analysis level 2.

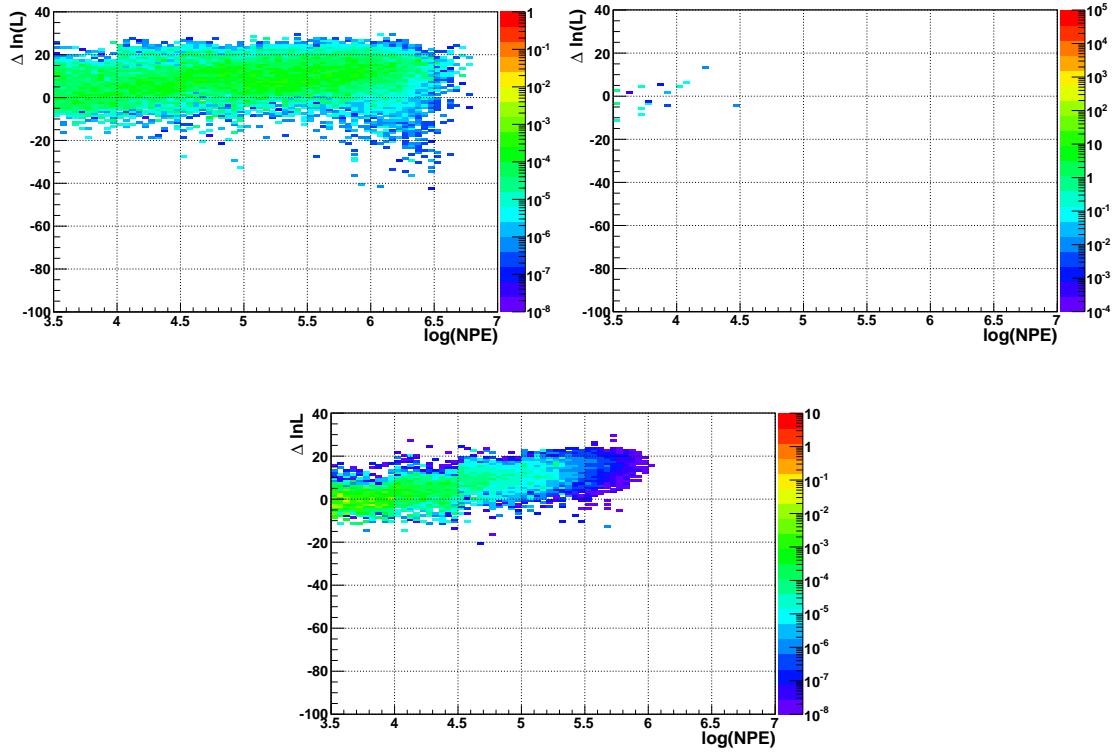


Figure 7.3: Event rate distributions of  $\Delta \ln(L_{\text{com}})$  vs  $\log(\text{NPE})$  for zenith bin 10 ( $\cos(\theta)=[0.1,0.0]$ ). Top left: GZK neutrino signal events, top right: CORSIKA background events, bottom: atmospheric neutrino events. Events for which the  $\Delta \ln(L_{\text{com}})$  is undefined are placed in the y-axis overflow bins and are kept for the next steps. The colour scale represents the event rate per  $(\Delta \ln(L_{\text{com}}), \log(\text{NPE}))$  bin. The displayed range for the event rate is different in each plot.

$\Delta \ln(L_{\text{com}})$  cuts accordingly does not give the best outcome for the analysis over the full sky. In turn a global MDP parameter is evaluated and minimised. The calculation of  $\mu_{lds}$  takes into account signal and background rates from all 14 zenith bins. Global MDP optimisation simultaneously determines the 14 sets of  $(\log(\text{NPE}), \Delta \ln(L_{\text{com}}))$  cuts.

$$\text{MDP}_{\text{global}} = \mu_{lds} / \mu_s \quad \text{with} \quad \mu_s = \sum_{i=1}^{14} \mu_{s,i}, \quad \mu_b = \sum_{i=1}^{14} (\mu_{\text{CORSIKA},i} + \mu_{\text{atmospheric},i}) \quad (7.5)$$

The global MDP optimisation means finding the minimum of a function of 28 free parameters. Scanning the full parameters phase space in order to find the minimum is a computationally intensive process which is impractical for this work. Instead it was decided to perform the global optimisation in an iterative fashion. The starting point for the cut values was chosen for each bin in the area where zero background events pass the cuts. Within that area of cut values, the set of cuts maximising the signal rate were chosen as the start values. The total 14 zenith bins signal and background rates passing these initial cuts are used to calculate an MDP starting value. The next steps of this cut optimisation is a process to achieve the

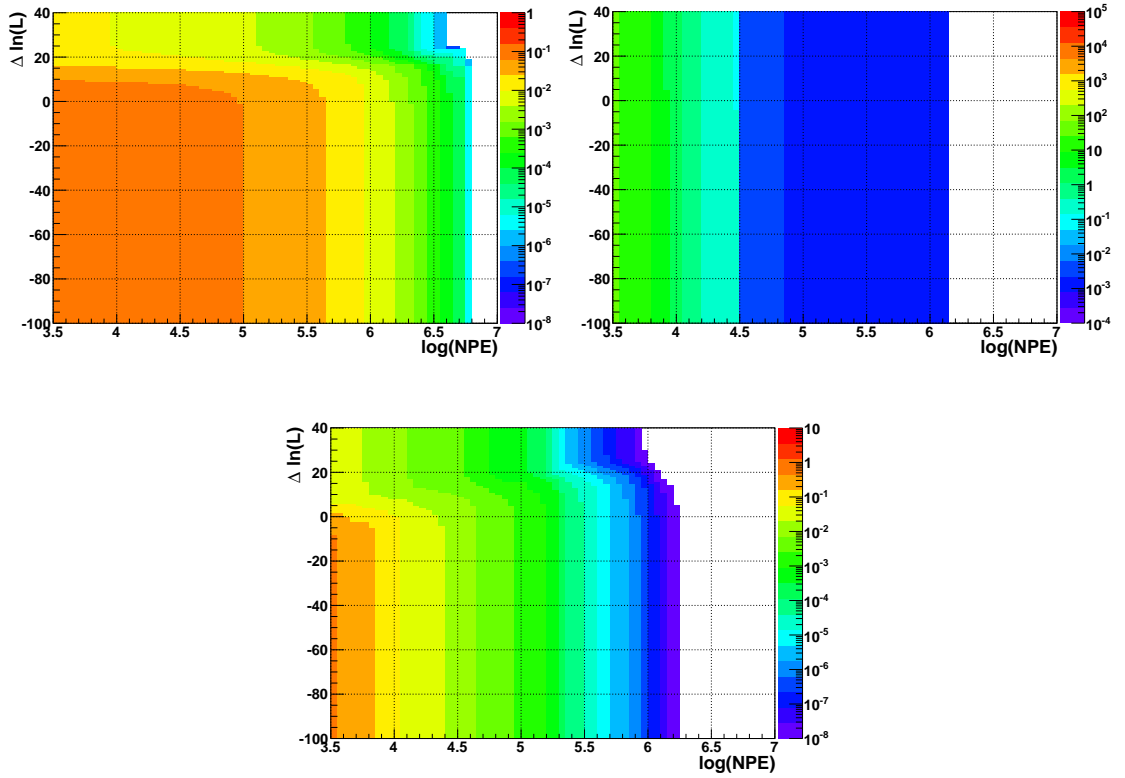


Figure 7.4: Complement cumulative distributions of  $\Delta \ln(L_{\text{com}})$  vs  $\log(\text{NPE})$  for zenith bin 10 ( $\cos(\theta)=[0.1,0.0]$ ). Top left: GZK neutrino signal events, top right: CORSIKA background events, bottom: atmospheric neutrino events.

lowest MDP value possible. Several zenith bins cut positions were scanned simultaneously at each step while the other ones remained fixed, and new sets of  $(\log(\text{NPE}), \Delta \ln(L_{\text{com}}))$  cuts were fixed according to the position of the minimum MDP value found in this step. The process was repeated many times while changing the combination of scanned zenith bins and scanned region around the step's cut position starting point and updating the global MDP value if it has improved. The process was finalised when the MDP value converged and did not show any improvement in the successive steps. The minimum MDP found is taken to be the global minimum and the 14 sets of  $(\log(\text{NPE}), \Delta \ln(L_{\text{com}}))$  final cut values are determined by its position. The results of the global MDP minimisation are reported in the next section.

### 7.3 Final event selection

The MDP minimum obtained in the iterative global minimisation is:

$$\text{MDP} = 16.4, \quad \mu_{lds} = 5.3, \quad \mu_s = 0.323.$$

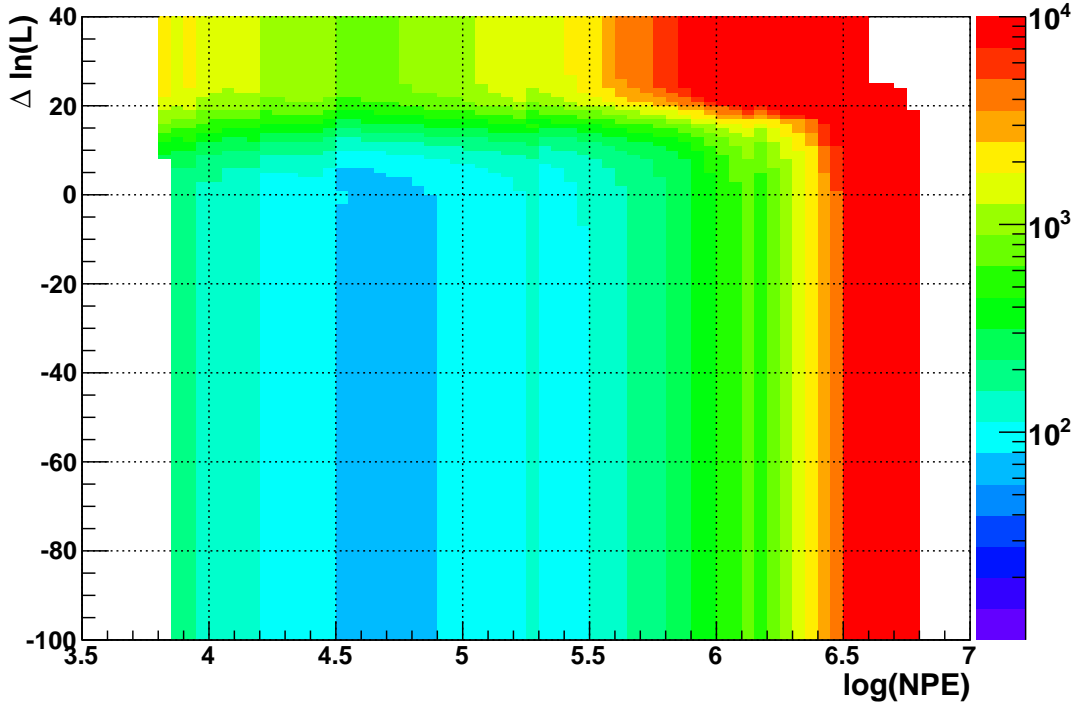


Figure 7.5: MDP parameter 2D map for zenith bin 10.

The interpretation of these values is that with the obtained final cut selection a minimum flux observation of 5.3 events, which is higher by a factor 16.4 than the signal expectation value of 0.323 events, would produce a  $5\sigma$  discovery. The background rate expectation for this final cut selection is 0.015, a factor 20 lower than the GZK signal expectation. Table 7.2 holds a summary of the expected event rates for the IC40 full year blinded data and Table 7.3 lists the full information of  $(\log(\text{NPE}), \Delta \ln(L_{\text{com}}))$  final cut values and passing rates for each zenith bin. The final GZK neutrino rate is 30.5% of the EHE filter level rate while the Analysis level 1 rate stands at 66% of the initial rate. Zero data burn sample events pass the final cuts. All CORSIKA events passing the final cuts are of single CR shower type. For all bins below  $\cos(\theta)=0.2$  no cut is placed on the  $\Delta \ln(L_{\text{com}})$  parameter. CORSIKA background events in these zenith bins are mis-reconstructed events with poorly determined zenith angle. This results in an unusable  $\Delta \ln(L_{\text{com}})$  parameter which can occur due to several different reasons, all of which are more likely for mis-reconstructed events: non converged  $\mu$ -function fit or alternatively the set of  $(a, \omega)$  values are away from the main distributions and there is no valid likelihood estimation for the values ( $\Delta \ln(L_{\text{perp}})$  undefined), or there are zero photon hit entries in the residual time range of  $[-400, 50]$  ns from which to construct  $\Delta \ln(L_{\text{tres}})$ . So in practice the  $\Delta \ln(L_{\text{com}})$  parameter is relevant for background rejection above  $\cos(\theta)=0.2$ .

Data stream	MDP final cut rates for IC40 blinded data
GZK total	0.32
(% from EHE filter rate)	(30.5%)
$E^{-2} \nu$ flux total	3.65
CORSIKA background	0.002
Atmospheric $\nu$ background	0.012
Total background	0.015

Table 7.2: Summary of the event rates passing the analysis level 3 cuts for the different simulation and data streams. Zero data burn sample events pass the final cut. Rates are for  $\nu + \bar{\nu}$ , all flavours summed.

### 7.3.1 Neutrino effective area

The sensitivity of the analysis to detect a neutrino signal is presented by the neutrino effective area. This parameter represents the equivalent area for which all neutrinos reaching the detector would be recorded and pass the event selection, taking into account the detector response function. The neutrino effective area at different cut levels of this analysis is shown in Figure 7.6 for the sum of the three neutrino flavours. The effect of the level 1 cut and the level 3 cut on the analysis detection power as a function of the neutrino energy is apparent by comparing the higher level effective area curves to the initial EHE filter one. Sensitivity is degraded at energies below  $\sim 10^{6.5}$  GeV and the final effective area at  $\sim 10^{10}$  GeV is about a factor  $\sim 2$  lower than the initial one. The analysis final level effective areas for the different neutrino flavours are provided in Figure 7.7.

The  $\nu_\mu$  and  $\nu_\tau$  effective areas are of similar size and are larger than the  $\nu_e$  effective area due to the large muon propagation range and the nature of tau composite events. The effect of the Glashow resonance is visible in the  $\nu_e$  effective area just below  $\sim 10^7$  GeV.

The effective areas obtained by another IC40 EHE neutrino search [86] are given for comparison (referred to as IC40 EHE curves). The two analyses differ in some of the tools they use such as the MC simulation models, waveform pulse extraction algorithm, track reconstruction algorithm, GZK model used for analysis optimisation and observables used for high level cut selection. In the final level of the IC40 EHE analysis the data are separated into deep and shallow events depending on the depth of the DOM with the largest recorded signal. The final MDP optimised cut selection is based on *portia* NPE (see section 5.2) and linefit reconstructed zenith angle for the shallow events, and *portia* NPE and event time span for the deep events. The analysis work described in this thesis has a lower neutrino effective area than the IC40 EHE analysis below  $\sim 10^7$  GeV and slightly higher above this energy. The new techniques in this analysis work compared to the IC40 EHE search are the use of the IceTop veto, the use of the topological cut parameters and the approach of making a final cut optimisation in 2D for each zenith bin. These entail some benefits as well as some disadvantages:

## Chapter 7. Analysis final event selection

bin number	$\cos(\theta)$ range	$\log(\text{NPE})$ cut value	$\Delta \ln(L_{\text{com}})$ cut value	CORSIKA total rate	atmospheric $\nu$ rate	GZK signal $\nu$ rate
1	[1.0, 0.9]	5.4	9	$3.87 \times 10^{-5}$	$1.93 \times 10^{-5}$	$7.28 \times 10^{-3}$
2	[0.9, 0.8]	5.6	-1	0	$1.54 \times 10^{-6}$	$6.49 \times 10^{-3}$
3	[0.8, 0.7]	5.2	9	$8.43 \times 10^{-4}$	$5.63 \times 10^{-5}$	$8.63 \times 10^{-3}$
4	[0.7, 0.6]	5.4	4	0	$6.3 \times 10^{-6}$	$9.98 \times 10^{-3}$
5	[0.6, 0.5]	5.5	-10	0	$3.21 \times 10^{-6}$	$1.13 \times 10^{-2}$
6	[0.5, 0.4]	5.5	1	0	$2.83 \times 10^{-6}$	$1.12 \times 10^{-2}$
7	[0.4, 0.3]	5.45	-8	0	$6.72 \times 10^{-6}$	$1.69 \times 10^{-2}$
8	[0.3, 0.2]	5.15	-1	0	$2.22 \times 10^{-4}$	$3.04 \times 10^{-2}$
9	[0.2, 0.1]	5.1	-	0	$6.01 \times 10^{-4}$	$4.33 \times 10^{-2}$
10	[0.1, 0.0]	4.85	-	$1.77 \times 10^{-3}$	$3.12 \times 10^{-3}$	$6.98 \times 10^{-2}$
11	[0.0, -0.1]	4.7	-	0	$5.86 \times 10^{-3}$	$5.89 \times 10^{-2}$
12	[-0.1, -0.2]	5.25	-	0	$2.39 \times 10^{-4}$	$1.20 \times 10^{-2}$
13	[-0.2, -0.4]	5.15	-	0	$4.61 \times 10^{-4}$	$1.12 \times 10^{-2}$
14	[-0.4, -1.0]	5.1	-	0	$1.87 \times 10^{-3}$	$2.45 \times 10^{-2}$
total rate				$2.65 \times 10^{-3}$	$1.25 \times 10^{-2}$	0.323

Table 7.3: Summary of the event rates passing the analysis level 3 cuts per zenith bin. Zero burn sample events pass the final cuts. Rates are for  $\nu + \bar{\nu}$ , all flavours summed.

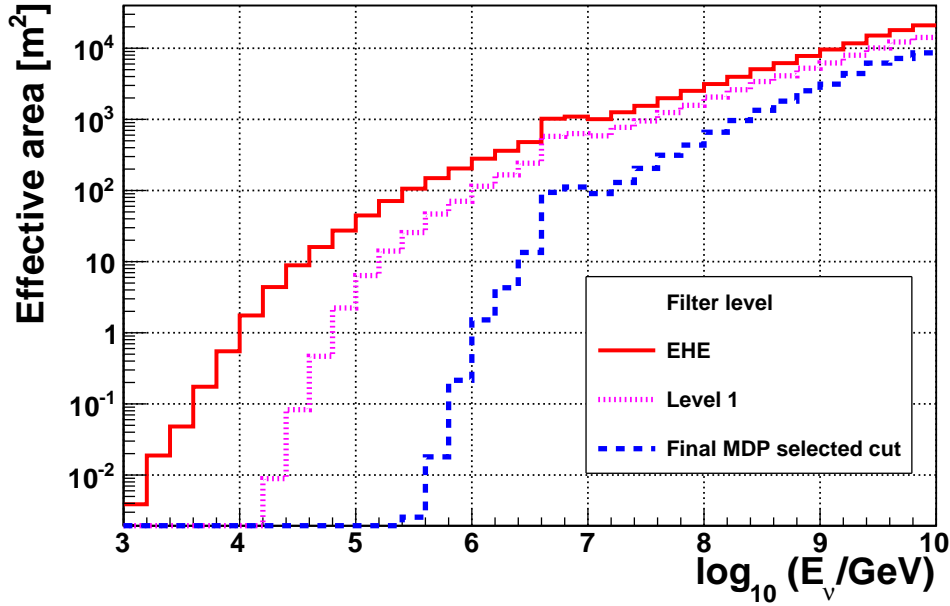


Figure 7.6: Analysis effective area for Analysis EHE filter (starting level in red), level 1 (dotted magenta) and final MDP selected cut (dashed blue).

- Muon background rejection by the IceTop veto leads to smaller background event rates at high NPE values in the close-to-downgoing zenith range. This permits the NPE final

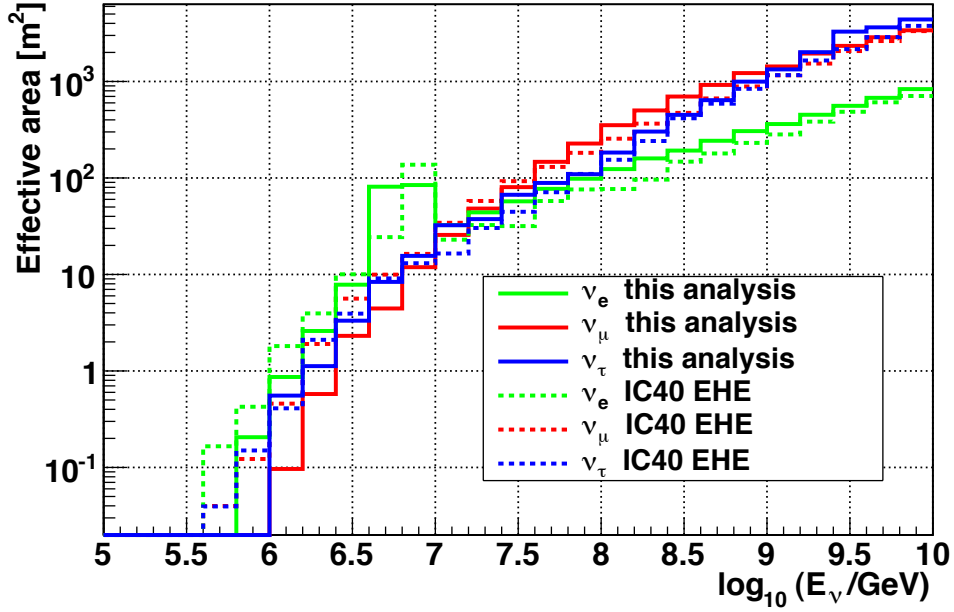


Figure 7.7: Analysis effective area for different neutrino flavours and in comparison to another IC40 EHE neutrino search [86].

cut to be set at lower values which increases the final neutrino signal rates though most of the GZK signal is around the horizon. On the other hand this analysis uses only data runs in which the IceTop surface array was functioning well. This requirement creates a live time loss of 18 days, or 5% reduction, from the IC40 EHE search live time of 333.5 days. The live time reduction degrades the overall sensitivity of the analysis and the final upper limit set by it. A possible improvement to this situation is discussed in section 8.1.

- The MPE track reconstruction method used in this work is a likelihood maximisation algorithm. The MPE reconstructed track parameters have on average much smaller errors in comparison with the linefit (analytical solution) first-guess track parameters. On the other hand, for a small portion of events the MPE reconstruction gives a poorly reconstructed track, and rarely, the minimisation procedure may not have converged at all.
- The 2D simultaneous optimisation of the final analysis level cut (per zenith bin) using the topological parameters should be an improvement compared to the IC40 EHE search where the final cut is set by a single parameter (different one for deep and shallow events). More information on the event characteristics is needed, particularly information which may be used to maximise the selection power of the observables.

### 7.4 Systematic uncertainties

The systematic uncertainty for this GZK neutrino search is due to the shortcomings in our description of all the processes taking place: physical interactions, particle's energy loss processes and detector attributes and response. The list below gives information about different uncertainty sources for this analysis and their estimated uncertainty ranges. Uncertainties obtained by the IC40 EHE analysis [86] are interesting due to similarities between that work and this GZK neutrino search.

- The uncertainty on the event rates due to the distribution of the NPE value for a charged particle energy. The IC40 EHE analysis obtains a background rate uncertainty of about 40% and signal rate uncertainty of up to 8% from this source [86].
- The uncertainty in the neutrino-nucleon inelastic cross section is estimated as  $\pm 9\%$  [78], which was shown to affect the signal event rate almost linearly [92].
- The uncertainty in the primary cosmic-ray composition at UHE energies. The IC40 EHE search tests two extreme composition scenarios, pure proton and pure iron, and reports a change of 84% in the atmospheric muon background event rate.
- The uncertainty in the hadronic interaction model used for air showers simulation. The IC40 EHE reports a difference of 36% in the background rate rising from two commonly used hadronic interaction models. However CORSIKA, the default model in this analysis, was not used by the IC40 EHE search.
- The uncertainty in the conventional component of the atmospheric neutrino flux (Honda model) is estimated as  $\pm 25\%$  on the flux absolute normalisation [38].
- The uncertainty in the prompt component of the atmospheric neutrino flux (Enberg model) is cited as an asymmetric error range in the overall flux normalisation of -44% to +25% [36].
- The uncertainty on the IceCube photomultiplier tube efficiency was measured to be  $\pm 8\%$  [65]. A shadowing effect from the string main cable and the PMT's magnetic shield reduces the DOM sensitivity by an estimated 7%. The uncertainty due to noise hits is expected to be small.
- The uncertainty on the measured properties of the glacial ice at the South Pole. A better determination of the scattering and absorption coefficients is an ongoing effort by the IceCube collaboration. Newer ice models [73] seem to describe data better than the AHA ice model used in this analysis. The difference between the AHA ice model and the new SPICE-Mie model is larger than the reported AHA model uncertainty.

Other uncertainty sources are the statistical error on the MC simulated events and the error on the IT veto efficiency which was obtained from data burn sample events (statistics dependent).

As mentioned above, this analysis work and the IC40 EHE search have some similarities (namely use of zenith-dependent NPE threshold cuts) and some differences, and their resulting neutrino effective areas are very similar. The IC40 EHE reports a combined uncertainty of about  $+14\% - 12\%$  for the signal event rate and  $+60\% - 96\%$  for the background rate. These numbers can only be used as a crude estimate for the systematic uncertainties in this analysis work.



## 8 Results & discussion

After finalising the three stages of cut selection, the analysis was approved by the IceCube collaboration. Permission was granted to “unblind”, i.e. study the IC40 entire year of previously blinded data. The data were processed through the analysis stream and no events from the unblinded data survived the final cuts, which is consistent with the background event rate expectation of 0.015. This result is used to calculate the neutrino flux upper limit after the observation of zero events during the analysis live time of 315.34 days, which is calculated as follows. The expected number of neutrino events in a certain energy range  $\Delta$  from a  $d\phi_\nu/dE$  neutrino flux is given by

$$\delta N = \int_{\Delta} A_\nu(E_\nu) \cdot \frac{d\phi_\nu}{dE} dE \cdot 4\pi \cdot T \quad (8.1)$$

where  $A_\nu$  is the neutrino effective area which depends on the neutrino energy,  $T$  is the experiment's live time. Taking into account the three neutrino flavours and assuming cosmogenic neutrinos of  $\nu_e : \nu_\mu : \nu_\tau$  produced with flavour ratio 1:2:0 and after oscillations detected at earth with 1:1:1 ratio we have

$$\delta N = \frac{1}{3} \int_{\Delta} \sum_{l=1}^3 A_{\nu_l}(E_\nu) \cdot \frac{d\phi_{\nu_e+\nu_\mu+\nu_\tau}}{dE} dE \cdot 4\pi \cdot T \quad (8.2)$$

$l$  represents the three neutrino flavours. The 90% Confidence Limit (CL) is obtained by demanding that  $dN$  is smaller than  $N_{90}$  which for background level  $\sim 0$  is equal to 2.44 as calculated by Feldman-Cousins [93]. Assuming a power-law flux of the form  $d\phi_\nu/dE = a \cdot E^{-\alpha}$  and using the relation

$$\frac{dN}{dE} = \frac{dN}{d \log E} \cdot \frac{1}{E \ln(10)} \quad (8.3)$$

the 90% CL condition becomes

$$N_{90} \leq \frac{1}{3} \int_{\Delta} \sum_{l=1}^3 A_{\nu_l}(E_\nu) \cdot a E^{-(\alpha-1)} \cdot d \log E \cdot \ln(10) \cdot 4\pi \cdot T \quad (8.4)$$

From here finding the upper limit means finding the power-law flux normalisation  $a$  which corresponds to the required limit

$$a \geq \frac{1}{\sum \frac{A_v}{E^{\alpha-1}}} \cdot \left( \frac{3 \cdot N_{90}}{\text{dlog } E \cdot \ln(10) \cdot 4\pi \cdot T} \right) \quad (8.5)$$

the sum here is over the bins within the energy range  $\Delta$  and the effective area in the sum of the three neutrino flavours areas.

The red curve in Figure 8.1 top plot (*Differential upper limit*) represents the quasi-differential model-independent 90% CL limit normalised by energy decade (meaning  $\text{dlog } E=1$ , and essentially assuming  $E^{-1}$  flux within the energy decade). The upper limit for an  $E^{-2}$  power-law flux is obtained in the energy range  $[10^{5.5}, 10^9]$  GeV at a value of  $E^2 \phi \leq 4.75 \times 10^{-8}$  GeV cm $^{-2}$  s $^{-1}$  sr $^{-1}$  and is shown by a dashed red curve Figure 8.1 bottom plot ( $E^{-2}$  *upper limit*). This result is slightly lower than the WB limit presented by a black dashed line (*WB limit*).

An alternative method for demonstrating the power of this analysis, and which is independent of the normalisation or energy binning, works by obtaining the spectral limit curves similarly as described in reference [94]. In this method the power-law 90% CL limit is calculated for a range of slopes, meaning for each  $\alpha$  in the appropriate range the  $a$  normalisation is calculated. The spectral limits are drawn and the intersection points of consecutive  $\alpha$  value limit curves define an envelope which represents the analysis upper limit to power-law flux spectra. For this work power-law limits were calculated for slopes in the range  $\alpha = [-1, 5]$  with  $d\alpha = 0.1$  and the resulting limits are shown in Figure 8.1 bottom plot. The envelope of these curves was extracted and is shown in Figure 8.1 upper plot by a magenta curve (*Power law limit*) and can be compared with the previously obtained upper limits which are based on a specific slope selection. The *Power law limit* curve is tangent to the  $E^{-2}$  upper limit and does not fall below it meaning the analysis is optimised for a power-law index of  $\gamma \sim 2$ .

The quasi-differential limit obtained for the previous IC40 EHE neutrino search [86] is calculated in the same manner and plotted for comparison by a green line (*Upper limit IC40 EHE*). It is noted that the green curve is not expected to recreate the IC40 EHE upper limit reported in [86] as it is calculated differently (different energy range is taken, the 90% CL upper limit differs due to different background expectation rate, systematic uncertainties are included and the Glashow resonance is ignored). Also included in the figure are the default GZK neutrino model (*SS08 135 HiRes*, dashed blue) and the highest flux model considered (*Ahlers  $E_{min} = 10^{19}$  eV best*, dashed-dotted black).

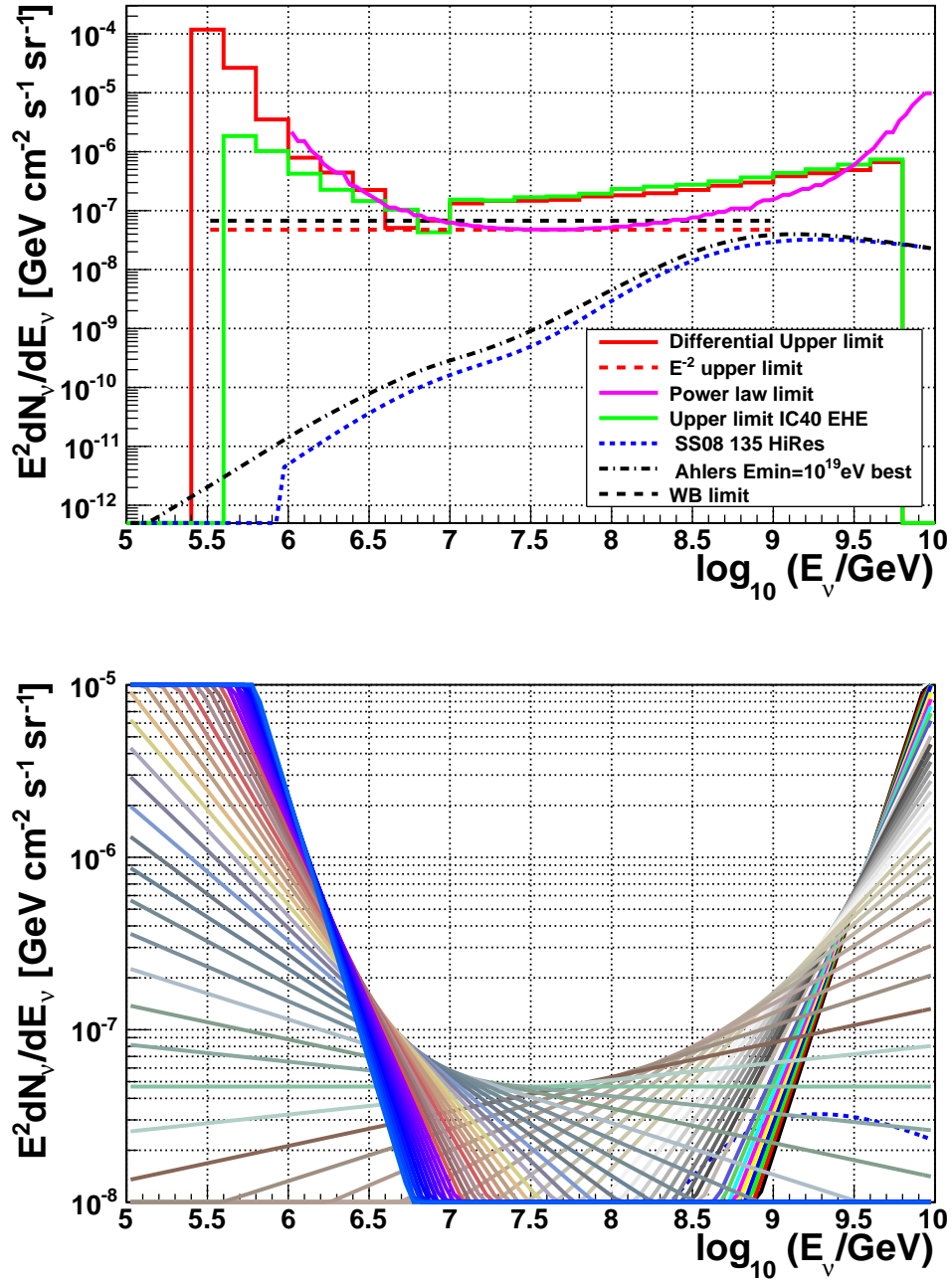


Figure 8.1: Upper plot: neutrino flux upper limit obtained by this analysis. Bottom plot: power-law spectra obtained limits. Flux slopes range from  $\alpha = -1$  (black rising line on the right) to  $\alpha = 5$  (blue curve on the left) in  $\Delta\alpha = 0.1$  steps.

### 8.1 Discussion

The IceTop veto on atmospheric muon background was developed for this analysis work and at that time was a novel approach in IceCube. Using the veto is even more interesting in the IC 59-strings detector and newer data samples as the detector is now running in soft local coincidence mode (section 6.1) and the veto efficiency is increased. The method can be useful also for lower energy neutrino searches by helping to reject atmospheric muon events that are mis-reconstructed and are in the signal region. It is a clean parameter as signal rejection by the veto condition is negligible. In hindsight, this analysis could have included the complete blinded data set, meaning including also the runs in which IceTop was malfunctioning ("bad" IT runs). In that case the IT veto would have been applied only on a subsample of the data ("good" IT runs). A correction factor for the veto efficiency would have been calculated depending on the time fractions of good and bad IT runs. The "effective" veto efficiency would have been applied then on the MC simulated streams and the loss of 18 days from the analysis live time would have been prevented. However, an implementation of this approach is needed in order to assess whether the resulting signal expectation rate and final upper limit would be better or worse than the current ones.

This GZK search was the first one in IceCube to use event topology parameters based on high level reconstruction and photon hit-pattern description. Specifically, the early photon hits likelihood parameter shows good capability of separation of signal from background events, also for events with energies below EHE. In the current approach it is the highest NPE events per zenith bin that survive the last level cut. The separation power of the topological parameters may be better exploited in an analysis with a combined likelihood approach. In that approach a single likelihood parameter can be calculated by incorporating all the relevant information (NPE, zenith, IceTop DOM hits, topological parameters and any other useful observables) and the final analysis cut is set by selecting a "signal-like" likelihood threshold.

Nowadays the IceCube detector is complete with its 86 strings and the instrumented volume has doubled compared to the 40 string detector. With increasing detection live time in the coming years, future GZK neutrino searches are expected to detect the first GZK neutrinos or to be able to exclude theoretical models.

# A Appendix A

The full event distributions used at Analysis level 3 (section 7.2) for determining the final cut values are given here. The sky is divided to  $\cos(\theta)$  bins with the following ranges:

bin number	1	2	3	4	5	6	7
$\cos(\theta)$	[1.0, 0.9]	[0.9, 0.8]	[0.8, 0.7]	[0.7, 0.6]	[0.6, 0.5]	[0.5, 0.4]	[0.4, 0.3]
bin number	8	9	10	11	12	13	14
$\cos(\theta)$	[0.3, 0.2]	[0.2, 0.1]	[0.1, 0.0]	[0.0, -0.1]	[-0.1, -0.2]	[-0.2, -0.4]	[-0.4, -1.0]

Table A.1:  $\cos(\theta)$  bins used at Analysis level 3.

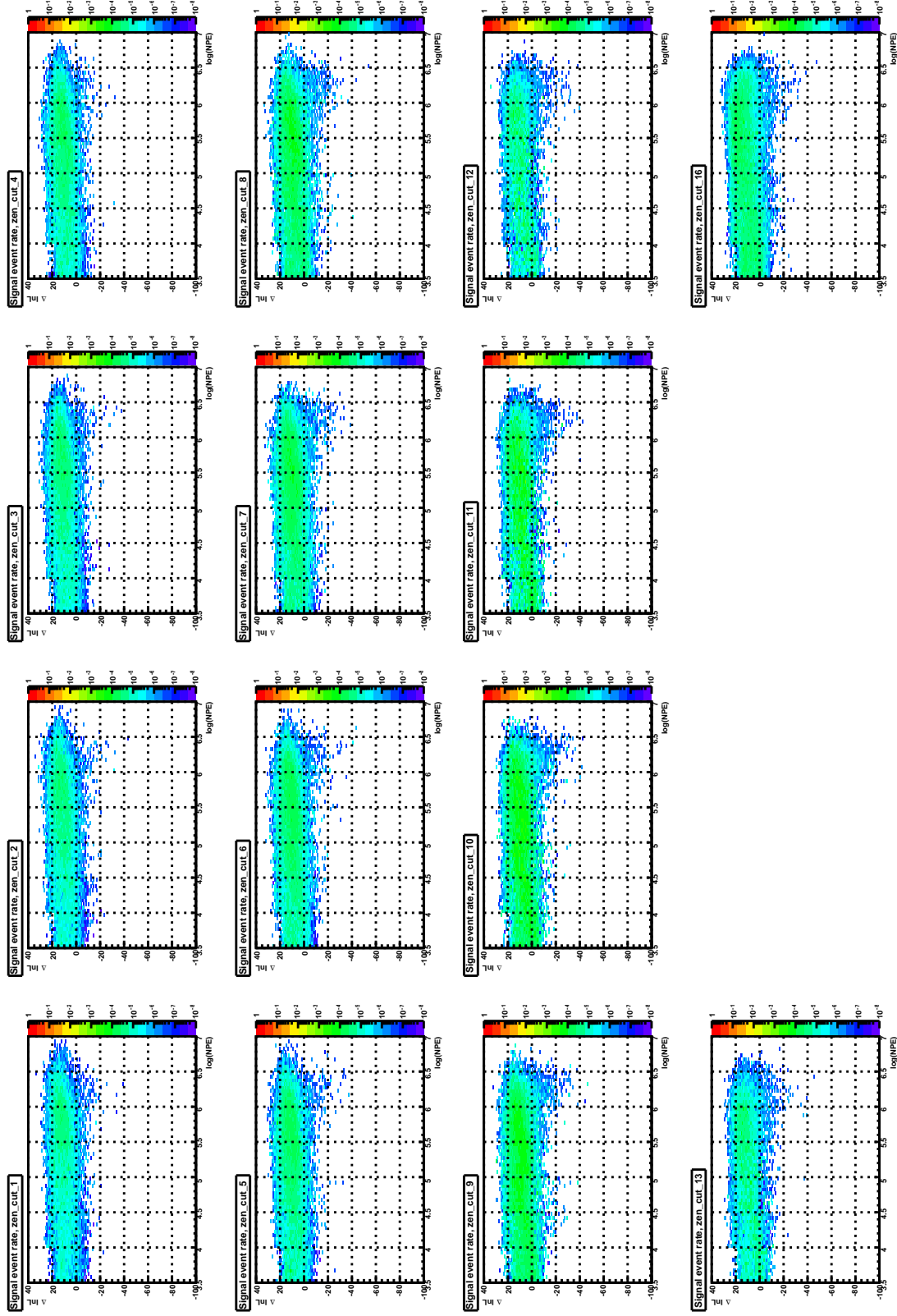


Figure A.1: GZK neutrino signal distribution of  $\Delta \ln(L_{\text{com}})$  vs  $\log(\text{NPE})$ .

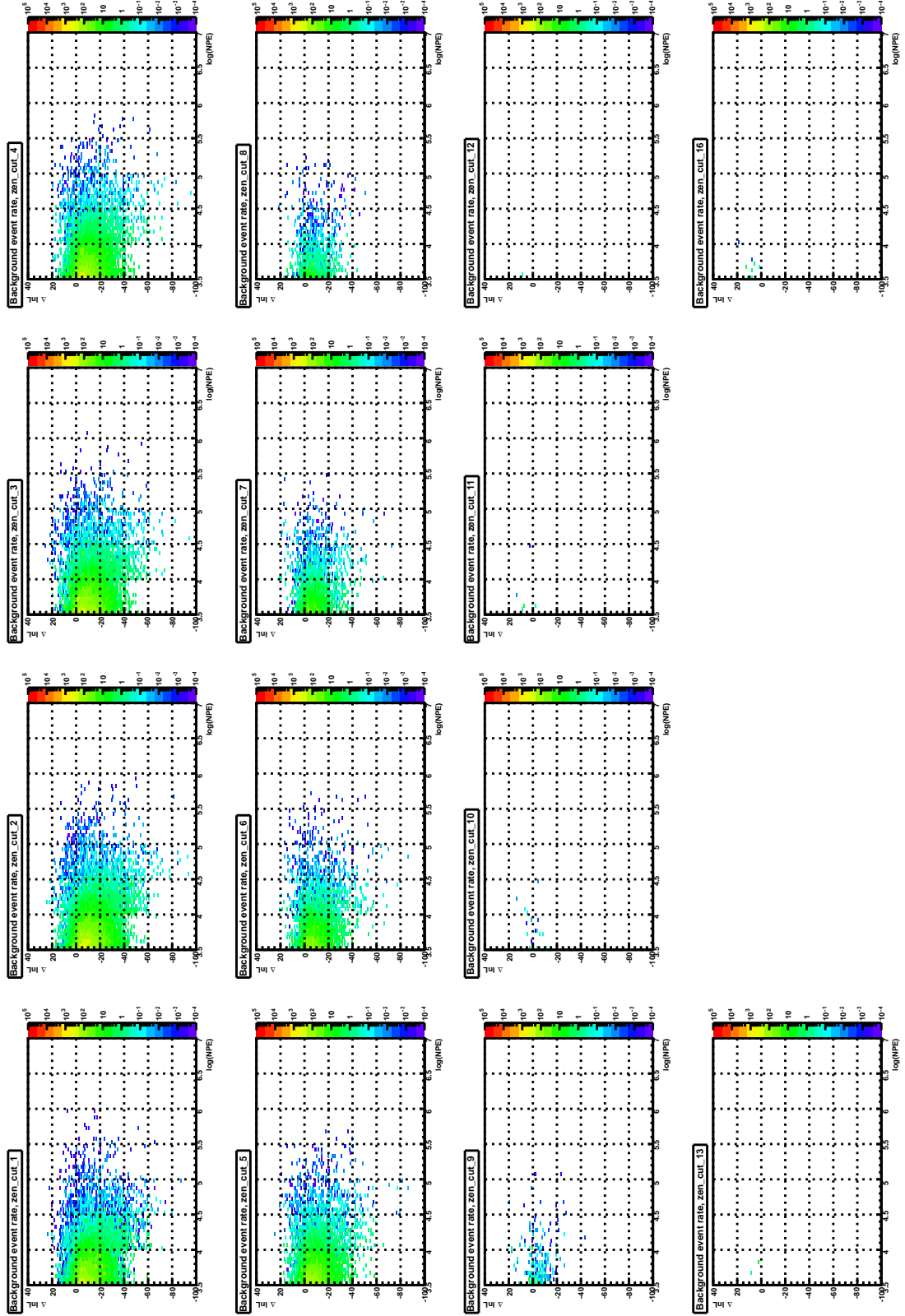


Figure A.2: Corsika background events distribution of  $\Delta \ln(L_{\text{com}})$  vs  $\log(\text{NPE})$ .

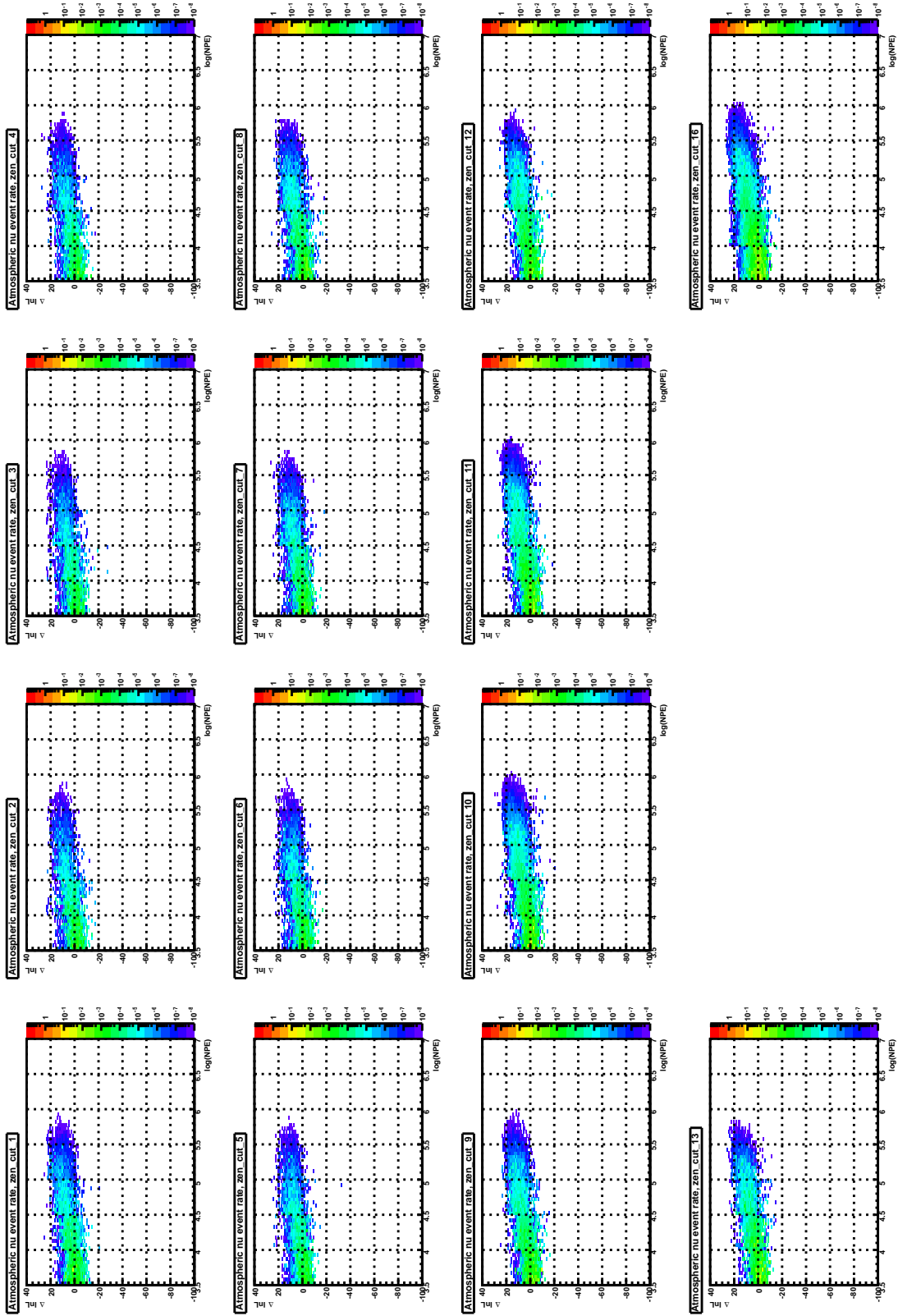


Figure A.3: Atmospheric neutrino background distribution of  $\Delta \ln(L_{\text{com}})$  vs  $\log(\text{NPE})$ .

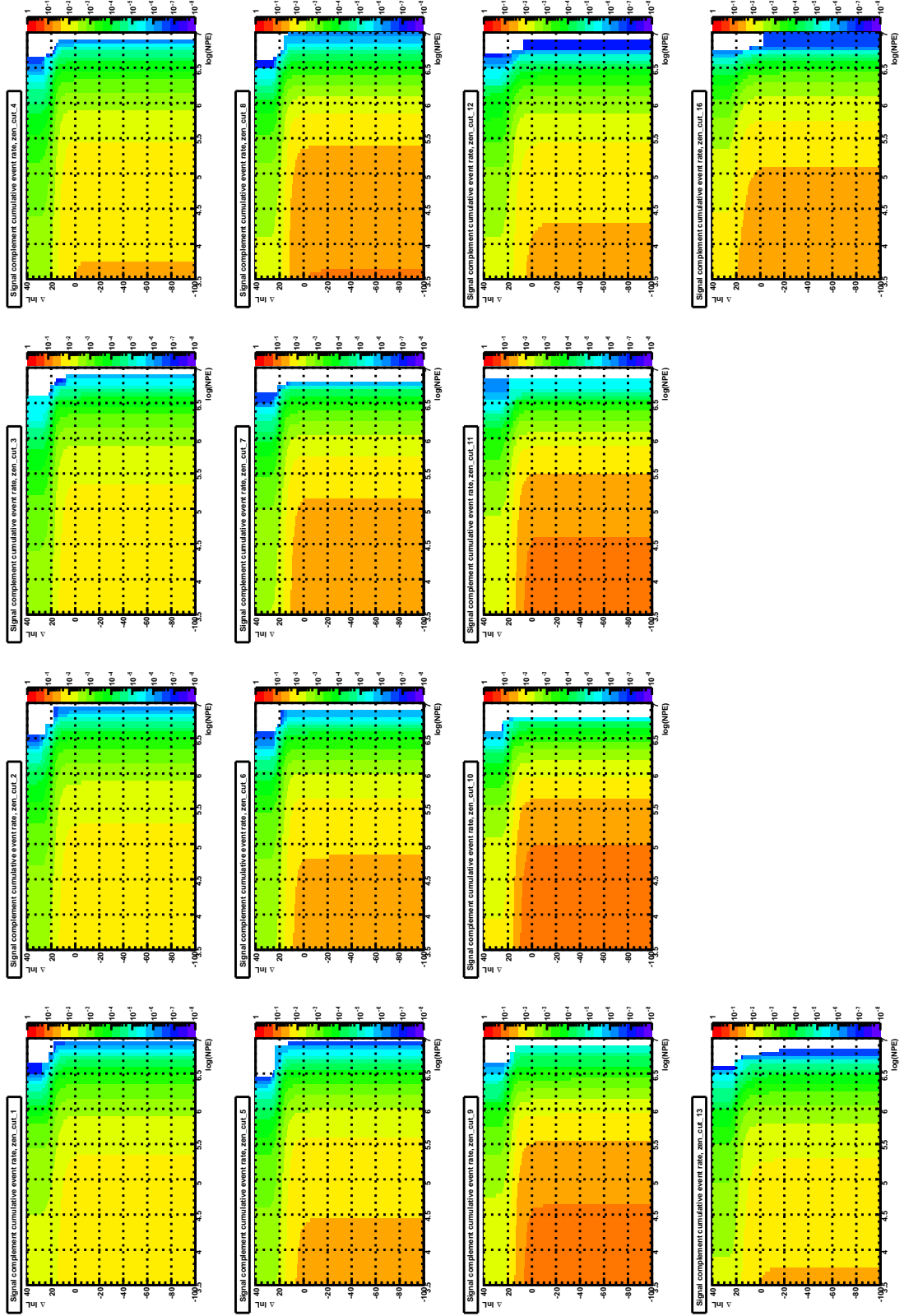


Figure A.4: GZK neutrino signal complement cumulative distributions of  $\Delta \ln(L_{\text{com}})$  vs  $\log(\text{NPE})$ .

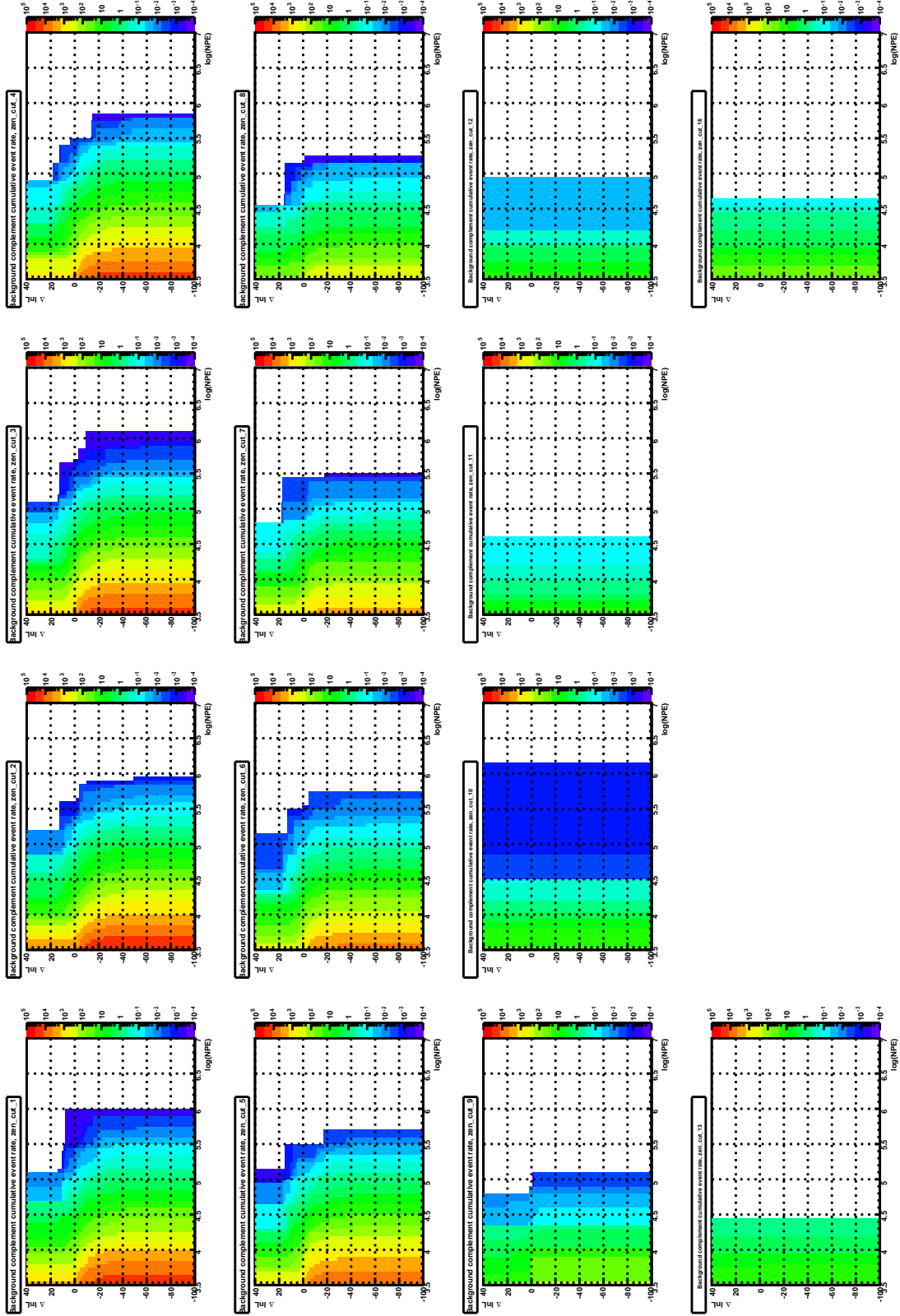


Figure A.5: Corsika background complement cumulative distributions of  $\Delta \ln(L_{\text{com}})$  vs  $\log(\text{NPE})$ .

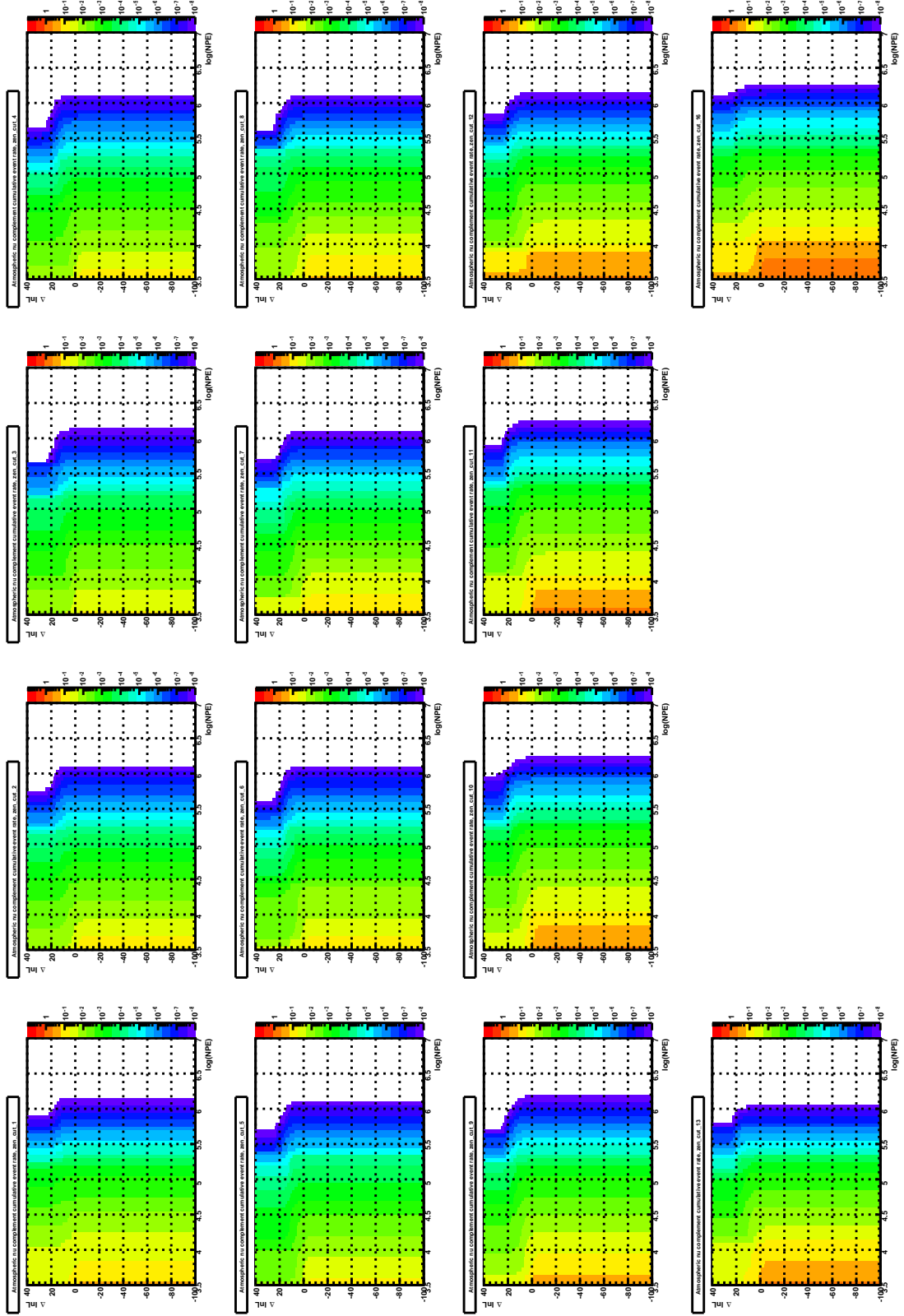


Figure A.6: Atmospheric neutrino background complement cumulative distributions of  $\Delta \ln(L_{\text{com}})$  vs  $\log(\text{NPE})$ .

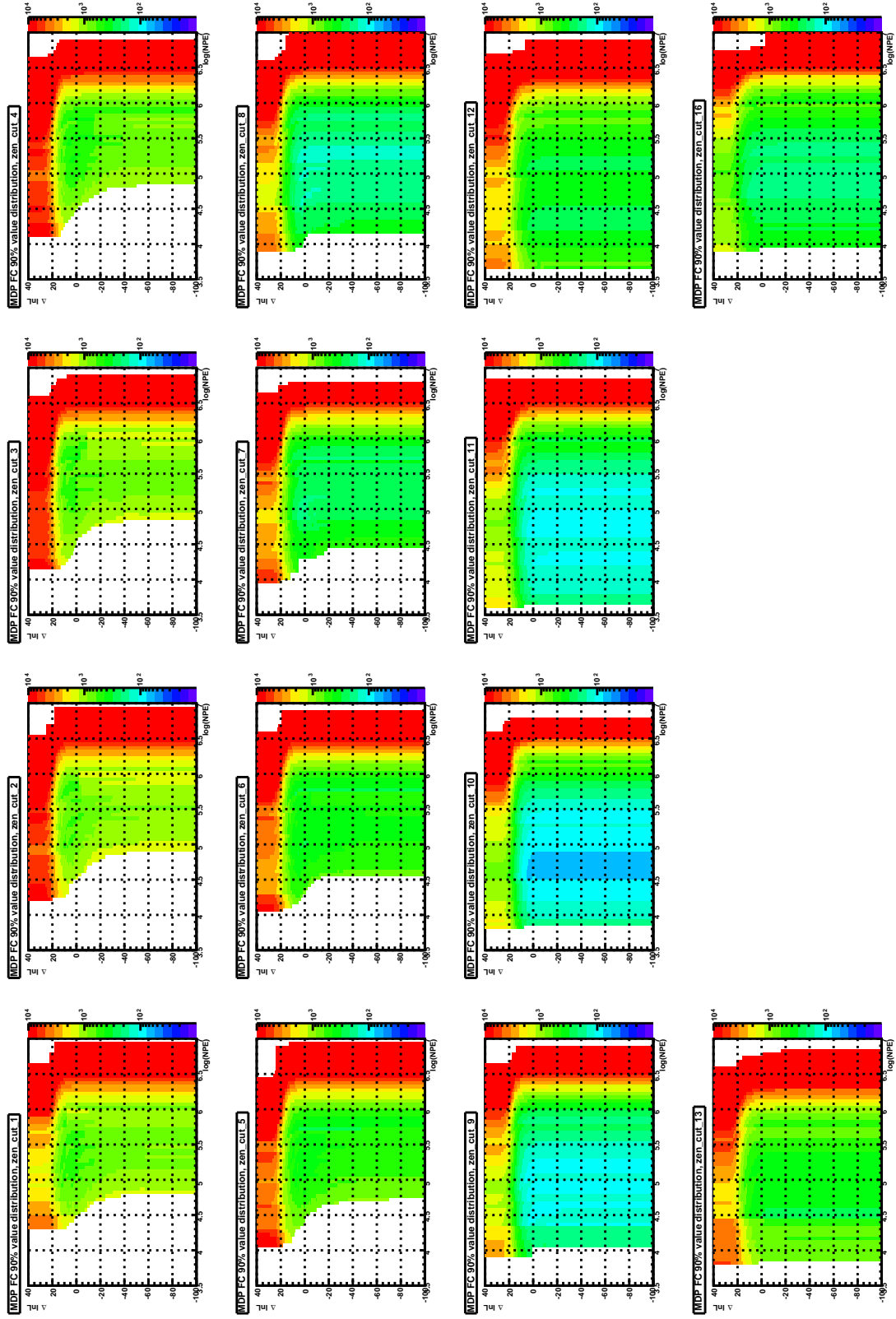


Figure A.7: MDP parameter value distributions w.r.t  $\Delta \ln(L_{\text{com}})$  and  $\log(\text{NPE})$ .

## **B** List of abbreviations

AGN - Active galactic nucleus  
AMANDA - Antarctic muon and neutrino detector array  
ANIS - All neutrino interaction simulation  
ATWD - Analog transient waveform digitiser  
CC - Charged-current  
CL - Confidence level  
CIB - Cosmic infrared background  
CMB - Cosmic microwave background  
CR - Cosmic ray  
CORSIKA - Cosmic ray simulation for Kascade  
DIS - Deep inelastic scattering  
DOM - Digital optical module  
EHE - Extreme high energy  
EM - Electromagnetic  
ESS - Engel-Seckel-Stanev  
fADC - fast analog to digital converter  
GRB - Gamma ray burst  
GZK - Greisen-Zatsepin-Kuzmin  
HLC - Hard local coincidence  
IC - IceCube  
ICL - IceCube laboratory  
IT - IceTop  
LC - Local coincidence  
MB - Main board  
MC - Monte Carlo  
MDP - Model discovery potential  
MMC - Muon Monte Carlo  
MNS - Maki-Nakagawa-Sakata  
MPE - Multi photoelectron

## **Appendix B. List of abbreviations**

---

MRF - Model rejection factor  
MSPS - Mega samples per second  
NC - Neutral-current  
NPE - Number of photoelectrons  
OM - Optical module  
PDF - Probability density function  
PE - Photoelectron  
PMT - Photomultiplier tube  
PnF - Processing and filtering  
PREM - Preliminary Earth model  
SLC - Soft local coincidence  
SMGCR - Standard model for galactic cosmic rays SMT - Simple majority trigger  
SNR - Supernova remnant  
SPB - Synchrotron proton blazar  
SPE - Single photoelectron  
SS - Seckel-Stanev  
UHECR - Ultra high energy cosmic ray  
WB - Waxman-Bahcall

# Bibliography

- [1] K. Hirata et al., "Observation of a neutrino burst from the supernova SN1987A", Phys. Rev. Lett. **58**: 1490 (1987).
- [2] T.K. Gaisser, "Cosmic Rays and Particle Physics", Cambridge university press (1990).
- [3] M. Takeda et. al., (The AGASA Collaboration), "Energy determination in the Akeno Giant Air Shower Array experiment", Astropart. Phys. **19**: 447 (2003).
- [4] R. Abbasi et al., (the HiRes collaboration), "A Study of the Composition of Ultra-High-Energy Cosmic Rays Using the High-Resolution Fly's Eye", Astrophys. J. **622**: 910 (2005).
- [5] J. Abraham et. al., (The Pierre Auger Collaboration), "Observation of the Suppression of the Flux of Cosmic Rays above  $4 \times 10^{19}$  eV", Phys. Rev. Lett. **101**: 061101 (2008).
- [6] J. Alcaraz et. al., (The AMS Collaboration), "Cosmic protons", Phys. Lett. **B 490**: 27 (2000).
- [7] J. Chang et. al., (The ATIC Collaboration), "An excess of cosmic ray electrons at energies of 300-800 GeV", Nature **456**: 362 (2008).
- [8] T. Antoni et. al., (The KASCADE Collaboration), "KASCADE measurements of energy spectra for elemental groups of cosmic rays: Results and open problems", Astropart. Phys. **24**: 1 (2005).
- [9] M. Amenomori et. al., "Tibet air shower array: results and future plan", J. Phys. Conf. Ser. **120**: 062024 (2008).
- [10] K. Nakamura et al., (The Particle Data Group), "The Review of Particle Physics", J. Phys. G **37**: 075021 (2010).
- [11] R. Aloisio, V. Berezhinsky and A. Gazizov., "Transition from galactic to extragalactic cosmic rays", Astropart. Phys. **39-40**: 129 (2012).
- [12] A. W. Strong, I. V. Moskalenko, and V. S. Ptuskin, Ann. Rev. of Nucl. and Part. Science **57**: 285 (2007).
- [13] K. Greisen, "End to the Cosmic-Ray Spectrum?", Phys. Rev. Lett. **16**: 748 (1966).  
G. T. Zatsepin and V. A. Kuzmin, "Upper limit of the spectrum of cosmic rays", JETP Lett. **4**: 78 (1966).

## Bibliography

---

- [14] D. Allard et al., "UHE nuclei propagation and the interpretation of the ankle in the cosmic-ray spectrum", *Astron. and Astrophys.* **443**: L29 (2005).  
D. Allard et al., "Implications of the cosmic ray spectrum for the mass composition at the highest energies", *JCAP* **0810**: 033 (2008).
- [15] J. Abraham et al., (The Pierre Auger Collaboration), "Measurement of the energy spectrum of cosmic rays above  $10^{18}$  eV using the Pierre Auger Observatory", *Phys. Lett.*, **B 685**: 239 (2010).
- [16] J. Abraham et al., (The Pierre Auger Collaboration), "Measurement of the depth of maximum of extensive air showers above  $10^{18}$  eV", *Phys. Rev. Lett.*, **104**: 091101 (2010).
- [17] R. Blandford and D. Eichler, "Particle acceleration at astrophysical shocks: A theory of cosmic ray origin", *Phys. Rept.* **154**: 1 (1987).
- [18] A. M. Hillas, "The Origin of Ultra-High-Energy Cosmic Rays", *Ann. Rev. Astro. Astrophys.*, **22**: 245 (1984).
- [19] W. Baade and F. Zwicky, "Remarks on Super-Novae and Cosmic Rays", *Phys. Rev.* **46**: 76 (1934).
- [20] F. Halzen, "Pionic Photons and Neutrinos from Cosmic Ray Accelerators", Presented at the Crakow School of Theoretical Physics, 11-19 June 2011, arXiv:1111.1131v1.
- [21] S.R. Kelner, F.A. Aharonian and V.V. Bugayov, "Energy spectra of gamma-rays, electrons and neutrinos produced at proton-proton interactions in the very high energy regime", *Phys. Rev.* **D 74**: 034018 (2006).
- [22] M. Ribordy, in "Neutrino Physics and Astrophysics", edited by G. Bellini and L. Ludhova, Proceedings of ISAPP Course CLXXXII, Varenna, Italy, 2011 (IOS Press, Amsterdam, 2012).
- [23] Z. Maki, M. Nakagawa, and S. Sakata, Prog. "Remarks on the Unified Model of Elementary Particles", *Theor. Phys.* **28**: 870 (1962).
- [24] H. Athar, M. Jezabek and O. Yasuda, "Effects of neutrino mixing on high-energy cosmic neutrino flux", *Phys. Rev.* **D 62**: 103007 (2000).
- [25] E. Waxman and J. Bahcall, "High Energy Neutrinos from Astrophysical Sources: An Upper Bound", *Phys. Rev.* **D 59**: 023002 (1999).
- [26] E. Waxman and J. Bahcall, "High Energy Astrophysical Neutrinos: the Upper Bound is Robust", *Phys. Rev.* **D 64** : 023002 (2001).
- [27] A. Muecke et al., "BL Lac Objects in the Synchrotron Proton Blazar Model" *Astropart. Phys.*, **18**: 593 (2003).
- [28] S. Razzaque, P. Meszaros and E. Waxman, "Neutrino tomography of gamma ray bursts and massive stellar collapses", *Phys. Rev.* **D 68**: 083001 (2003).

- 
- [29] A. Achterberg et al., "Intergalactic Propagation of UHE Cosmic Rays", arXiv:astro-ph/9907060 (1999).
- [30] R. Engel, D. Seckel and T. Stanev, "Neutrinos from propagation of ultra-high energy protons", Phys. Rev. **D 64**: 093010 (2001).
- [31] G. Sigl, in "Neutrino Physics and Astrophysics", edited by G. Bellini and L. Ludhova, Proceedings of ISAPP Course CLXXXII, Varenna, Italy, 2011 (IOS Press, Amsterdam, 2012).
- [32] D. Seckel and T. Stanev. Talk presented at the IAPS 2008 conference in Golden, Colorado.
- [33] M. Ahlers et al., "GZK Neutrinos after the Fermi-LAT Diffuse Photon Flux Measurement", Astropart. Phys. **34**: 106 (2010).
- [34] M. Ave et al., "Cosmogenic Neutrinos from Ultra-High Energy Nuclei", Astropart. Phys. **23**: 19 (2005).
- [35] B. Louis et al., "The evidence for oscillations", Los Alamos Science number 25 (1997).
- [36] R. Enberg, M. H. Reno, I. Sarcevic, "Prompt neutrino fluxes from atmospheric charm", Phys. Rev. **D 78**: 043005 (2008).
- [37] M. Thunman, G. Ingelman, and P. Gondolo, "Charm production and high energy atmospheric muon and neutrino fluxes" Astropart. Phys. **5**: 309 (1996).
- [38] M. Honda et al., "Calculation of atmospheric neutrino flux using the interaction model calibrated with atmospheric muon data", Phys. Rev. **D 75**: 043006 (2007).
- [39] S. L. Glashow, "Resonant scattering of antineutrinos", Phys. Rev. **118**: 316 (1960).
- [40] A. Bhattacharya et al., "The Glashow resonance at IceCube: signatures, event rates and  $pp$  vs.  $p\gamma$  interactions", JCAP **1110**: 017 (2011).
- [41] A. Connolly, R. S. Thorne and D Waters, "Calculation of High Energy Neutrino-Nucleon Cross Sections and Uncertainties Using the MSTW Parton Distribution Functions and Implications for Future Experiments", Phys. Rev. **D 83**: 113009 (2011).
- [42] A.Z. Gazizov and S.I. Yanush, "Hard pomeron enhancement of ultrahigh-energy neutrino-nucleon cross-sections", Phys. Rev. **D 65**: 93003 (2002).
- [43] H. Lai et al., "Global QCD analysis of parton structure of the nucleon: CTEQ5 parton distributions", Eur. Phys. J. **C 12**: 375 (2000).
- [44] A.Z. Gazizov, M. Kowalski, "ANIS: High energy neutrino generator for neutrino telescopes", Comput. Phys. Commun., **172**: 203 (2005).
- [45] A. Cooper-Sarkar, S. Sarkar, "Predictions for high energy neutrino cross-sections from the ZEUS global PDF fits", JHEP **0801**: 075 (2008).

## Bibliography

---

- [46] C. H. V. Wiebusch, "The detection of faint light in deep underwater neutrino telescopes", PhD thesis, RWTH Aachen (1995).
- [47] G.A. Askaryan, "Excess negative charge of an electron-photon shower and its coherent radio emission", JTEP, **14**: 441 (1962).
- [48] I. Kravchenko, et al., "RICE limits on the diffuse ultra-high energy neutrino flux", Phys. Rev. **D 73**: 082002 (2006).
- [49] P. W. Gorham et al., "Observational constraints on the ultra-high energy cosmic neutrino flux from the second flight of the ANITA experiment", Phys. Rev. **D 82**: 022004 (2010).
- [50] J. Vandenbroucke, G. Gratta and N. Lehtinen, "Experimental Study of Acoustic Ultra-High-Energy Neutrino Detection", Astrophys. J. **621**: 301 (2005).
- [51] The ANTARES collaboration, "AMADEUS - The Acoustic Neutrino Detection Test System of the ANTARES Deep-Sea Neutrino Telescope", Nucl. Instr. Meth. Physics Research Section A, **626**: 128 (2011).
- [52] The IceCube collaboration, "Status and recent results of the South Pole Acoustic Test Setup", 4th International workshop on Acoustic and Radio EeV Neutrino detection Activities, ARENA 2010, arXiv:1010.2025.
- [53] L. Braun et al., "Acoustic resonant sensor for ultra high energy neutrino detection", Astropart. Phys. **34**: 595 (2011).
- [54] D. Chirkin, W. Rohde, "Propagating leptons through matter with Muon Monte Carlo (MMC)", arXiv:hep-ph/0407075v2 (2004).
- [55] T. DeYoung, S. Razzaque, D.F. Cowen, "A novel tau signature in neutrino telescopes", J. Phys. Conf. Ser., **60**: 231 (2007).
- [56] K. Nakamura et al. (Particle Data Group) "Tau branching fractions", J. Phys. **G 37**: 075021 (2010).
- [57] S. Iyer Dutta, M. H. Reno, I. Sarcevic, D. Seckel, "Propagation of muons and taus at high energy", Phys. Rev. **D 63**: 094020 (2001).
- [58] E. Anders et al., (The AMANDA collaboration), "Results from the AMANDA high energy neutrino detector ", Nucl. Phys. Proc. Suppl. **91**: 423 (2000).
- [59] A. Achterberg et al., (The IceCube collaboration), "First year performance of the IceCube neutrino telescope", Astropart. Phys. **26**: 155 (2006).
- [60] R. Abbasi et al., (The IceCube Collaboration), "The Design and Performance of IceCube DeepCore", Astropart. Phys. **35**: 615 (2012).

- 
- [61] L. Kopke for the IceCube Collaboration, "Supernova Neutrino Detection with IceCube", Contribution to the "5th Symposium on Large TPCs for Low Energy Rare Events and Workshop on Neutrinos from Supernovae", Paris, Dec. 2010. ( arXiv:1106.6225).
- [62] L. Demiroers, M. Ribordy and M. Salathe, "Novel technique for supernova detection with IceCube", *Astropart. Phys.* **35**: 485 (2012).
- [63] R. Bruijn for the IceCube collaboration, "Supernova Detection in IceCube: Status and Future", *Nucl. Phys.* **B 237**: 94 (2013).
- [64] K. Hanson, O. Tarasova, "Design and production of the IceCube digital optical module", *Nucl. Instr. Meth.* **A 567**: 214 (2006).
- [65] R. Abbasi et al., (The IceCube collaboration), "Calibration and characterization of the IceCube photomultiplier tube", *Nucl. Instr. Meth.* **A 618**: 139 (2010).
- [66] A. Karle, "Monte Carlo simulation of photon transport and detection in deep ice: Muons and cascades", *Proceedings of the Workshop on Simulation and Analysis Methods for Large Neutrino Telescopes*, DESY (1998).
- [67] R. Abbasi et al., (The IceCube collaboration), "The IceCube data acquisition system: signal capture, digitization and timestamping ", *Nucl. Instr. Meth.* **A 601**: 294 (2009).
- [68] M. Ackerman et al., (The AMANDA collaboration), "Optical properties of deep glacial ice at the South Pole", *J. Geophys. Res.* **D13**: 203 (2005).
- [69] P.B. Price, K. Woschnagg, D. Chirkin, "Age vs depth of glacial ice at South Pole", *Geophys. Res. Lett.* **27**(13): 2129 (2000).
- [70] P. Askebjerg et al., "UV and optical light transmission properties in deep ice at the South Pole", *Geophys. Res. Lett.* **24**: 1355 (1997).
- [71] S.L. Miller, "Clathrate hydrates of air in Antarctic ice", *Science* **165**: 489 (1969).
- [72] K. Woschnagg and P. B. Price, "Temperature Dependence of Absorption in Ice at 532 nm", *Applied Optics* **40**: 2496 (2001).
- [73] M.G. Aartsen et al., (The IceCube collaboration), "Measurement of South Pole ice transparency with the IceCube LED calibration system", *Nucl. Instr. Meth.* **A 73**: 89 (2013).
- [74] D. Heck et al., "Corsika: A monte carlo code to simulate extensive air showers", tech. rep. FZKA (1998).
- [75] R. S. Fletcher, T. K. Gaisser, P. Lipari and T. Stanev, "Sibyll: An event generator for simulation of high energy cosmic ray cascades", *Phys. Rev.* **D 50**: 5710 (1994).
- [76] J. R. Hoerandel, "On the knee in the energy spectrum of cosmic rays", *Astropart. Phys.* **19**: 193 (2003).

## Bibliography

---

- [77] R. Glasstetter et al (the KASCADE collaboration), "Analysis of Electron and Muon Size Spectra of EAS", Proc. of the 26th Intern. Cosmic Ray Conf., 222, Salt Lake City, USA (1999).
- [78] A. Cooper-Sarkar and S. Sarkar, "Predictions for high energy neutrino cross-sections from the ZEUS global PDF fits", JHEP **1**: 075 (2008).
- [79] A.M. Dziewonski and D.L. Anderson., "Preliminary reference earth model", Phys. Earth Planet Int. **25**: 297 (1981).
- [80] J. Lundberg et al., "Light tracking through ice and water - scattering and absorption in heterogeneous media with Photonics", Nucl. Instr. Meth. **A 581**: 619 (2007).
- [81] C. Roucelle, "Documentation for the DOMcalibrator module", IceCube internal report (2007).
- [82] D. Chirkin, "Feature extraction of IceCube waveforms", IceCube internal report (2007).
- [83] J. Ahrens et al. (the AMANDA collaboration), "Muon Track Reconstruction and Data Selection Techniques in AMANDA", Nucl. Instr. Meth. **A 524**: 169 (2004).
- [84] D. Pandel, "Bestimmung von Wasser- und Detektorparametern und Rekonstruktion von Myonen bis 100 TeV mit dem Baikal-Neutrino teleskop NT-72", Diploma thesis, Humboldt-Universität zu Berlin, Berlin, Germany (1996).
- [85] G. Japaridze and M. Ribordy, "Realistic arrival time distribution from an isotropic light source", arXiv:astro-ph/0506136 (2005).
- [86] R. Abbasi et al., (the IceCube collaboration), "Constraints on the extremely-high energy cosmic neutrino flux with the IceCube 2008-2009 data", Phys. Rev. **D 83**: 092003 (2011).
- [87] L. Gerhardt et al., Proceedings of the 31st ICRC, Lodz, Poland, July 2009. arXiv:0909.0055v.1.
- [88] M. Ribordy, "Reconstruction of Composite Events in Neutrino Telescopes", Nucl. Instr. Meth. **A 574**: 137 (2007).
- [89] G. Hill and K. Rawlins, "Unbiased cut selection for optimal upper limits in neutrino detectors: the model rejection potential technique", Astropart. Phys. **19**: 393 (2003).
- [90] G. Punzi, "Sensitivity of searches for new signals and its optimization", Talk from PHYS-TAT03, Stanford, California, USA, arXiv:physics/0308063 (2003).
- [91] G. Hill et al., "Examining the balance between optimising an analysis for best limit setting and best discovery potential", Proceedings of PHYSTAT O5, Oxford, England (2005).
- [92] R. Abbasi et al. (the IceCube collaboration), "The first search for extremely-high energy cosmogenic neutrinos with the IceCube Neutrino Observatory", Phys. Rev. **D 82**: 072003 (2010).

- [93] G.J. Feldman and R.D. Cousins, "A Unified Approach to the Classical Statistical Analysis of Small Signals", Phys. Rev. **D 57**: 3873 (1998).
- [94] M. Ribordy and A. Neronov, "IceCube Sensitivity for Neutrino Flux from Fermi Blazars in Quiescent States", Phys. Rev. **D 80**: 083008 (2009).



# Shirit Cohen

---

Avenue du Jura 5  
01210 Ferney-Voltaire, France  
+41 76 405 10 92  
shirit.cohen@epfl.ch



## Education

- 2007 – 2013 **PhD in Astroparticle Physics** EPFL, Lausanne (graduation expected 05/2013)  
Invited student for 3 months at the University of Wisconsin, Madison, WI, US
- 2004 – 2007 **MSc in Particle Physics** University of Amsterdam, The Netherlands
- 2000 – 2004 **BA in Physics** Technion, Haifa, Israel

## Professional experience

- 2007 – 2012 **Teaching assistant** at the High Energy Physics Laboratory, EPFL. Coordinating and tutoring physics courses and laboratory work in French & English
- 1998 – 2000 **Electronic circuit designer** (full position) E.C.I. Telecom, Petah-Tikva, Israel.  
Design verification while interacting with engineers, designers and assembly line
- 1996 – 1998 **Electronic technician** in an R&D team, Israeli Defense Forces
- 1993 – 1996 **Summer camp instructor** supervising children groups & organizing activities

## Projects

- 2007 – 2012 **PhD thesis** with the IceCube neutrino observatory at the South Pole.  
Performing data mining, statistical analysis and developing new detection methods of high energy neutrinos. Presenting results in international meetings
- 2006 – 2007 **MSc thesis** with the LHCb experiment at CERN, Geneva. Determining the experiment's sensitivity for physics measurements by Monte Carlo simulation studies
- 2003 **CERN summer student research project** with the ATLAS collaboration, developing new methods for detector quality checks

## IT skills

C/C++, Python, Matlab, MS-Office, Root, RooFit

## Languages

**Hebrew:** Mother tongue   **English:** Excellent   **French:** Good level (C1)

## Other interests

Brazilian and African dance and music. Active in "Sambaloelek" association, Preveessin, France

## Personal details

**Date of birth:** 20 July 1978   **Nationality:** Austrian, Israeli